BRAGANÇA
POLYTECHNIC UNIVERSITY
INSTITUTO POLITÉCNICO
DE BRAGANÇA

UNIVERSIDADE TECNOLÓGICA FEDERAL DO PARANÁ

ANALYSIS OF FAILURE IN SHEET METAL STAMPING

THIAGO FERNANDO KAWAKAMI

Thesis presented to the School of Technology and Management in the scope of the Master in Mechanical Engineering Degree.

Bragança

2024-2025

BRAGANÇA POLYTECHNIC UNIVERSITY
INSTITUTO POLITÉCNICO DE BRAGANÇA

UTFPR
UNIVERSIDADE TECNOLÓGICA FEDERAL DO PARANÁ

ANALYSIS OF FAILURE IN SHEET METAL STAMPING

THIAGO FERNANDO KAWAKAMI a61435

Thesis presented to the School of Technology and Management in the scope of the Master in Mechanical Engineering Degree.

Supervisors:
Ph.D. Prof. Luis Manuel Ribeiro de Mesquita
M.Sc. Eng. Osmano Morais
Ph.D. Prof. Janaína Fracaro de Souza

This document does not include the suggestions made by the board.

Bragança
2024-2025

Dedication

I would like to dedicate this master's thesis, first and foremost, to God.

I also dedicate it to my parents, my mother Luciane and my father Marcelo, as well as to my relatives Shigueki, Luiza, Toshike, and Iza, who have supported me in every aspect of life from the very beginning. They always encouraged me to study and strive for more. None of this would have been possible without them.

To my siblings, Lucas and Caroline—thank you for your constant motivation, laughter, and jokes.

I am especially grateful to my uncle Rodovaldo, who has been like a father to me. I also thank my uncles and aunt, André, Flavia, and Issao, for their generous financial support.

To all the friends I made along this journey—especially my childhood friends Felipe, Arthur, and Lucas Fabrício—thank you for inspiring me.

To my university friends, especially Thiago Yuji, Thiago Watanabe, Victor Segré, and Vinícius Muraoka, thank you for trusting me and helping me through the classes along this path.

I am deeply thankful to my undergraduate research advisor, Dr. Alireza Mohebi Ashtiani, who taught me so much and guided me throughout my academic journey.

Finally, I would like to express my appreciation to my former boss, Guerreiro, and to everyone at his company, for their support and influence on my professional development.

Acknowledgment

I would like to express my sincere gratitude to the **Federal Technological University of Paraná (UTFPR)** and the **Polytechnic Institute of Bragança (IPB)** for providing me with the opportunity to pursue my studies as a double degree student.

I am also deeply grateful to **Catraport**, M.Sc. Osmano Morais, João, and M.Sc. Julia Murta for the opportunity to carry out my thesis in collaboration with industry, and for their valuable guidance throughout this process.

I extend my heartfelt thanks to all my professors who helped me reach this stage, especially Ph.D. Luís Mesquita and Ph.D. Janaína Fracaro de Souza. I am particularly grateful for your availability and patience. My gratitude extends beyond the course content to the lasting lessons you have imparted—lessons I will carry with me throughout life.

I would also like to thank Luiza for her constant support and assistance in the Laboratory of Mechanical Resistance of Materials (LERM), and to Amilton Patrick for his help as well.

My sincere thanks go to Avenida Brasil, especially Mara and Leandro, for giving me the opportunity to work in Portugal and for enabling me to support myself during this period.

To my housemates from “Bairro Nobre”, thank you for the long conversations and companionship. To Raphael Britto, thank you for the countless hours we spent together in the library working on our theses.

I am also grateful to Bryan, Jovanne, and Elisane for their warmth, support, and for welcoming me into their home. I’m also grateful to Eduardo and Larissa my fathers.

To my friends from CIMO (Mountain Research Center) and FAB-LAB, thank you for the laughs, patience, and advice.

I would not have completed this thesis without the support of each and every one of you.

Abstract

In the past, forming dies were developed through a trial-and-error process, where failures were identified and the die shape was subsequently adjusted. With the advent of the Finite Element Method (FEM), this process became more efficient, as FEM could be used to simulate and analyze forming results. Meanwhile, the tightening of automotive emission standards has increased the demand for more suitable materials, leading to stricter safety margins to achieve the desired weight reduction.

In this work, the FEM will be employed to assess whether the failures observed in the industrial cold stamping process could have been predicted. To achieve this, several tensile tests will be conducted to characterize the material properties of two Ferritic Stainless Steel (FSS), EN 1.4509 and EN 1.4512. Using Digital Image Correlation (DIC), the anisotropy coefficients will be obtained and used to model the Barlat (1989) and Hill (1948) yield criteria. The Forming Limit Diagram (FLD) will be predicted through Abspoel and Keeler and Brazier methods. Finally, FEM simulations will be carried out using Ansys Forming software on two different stamped parts. The first part involves seven forming operations, while the second is limited to only the initial operation. In the first part, an increased tendency for wrinkling is observed near the notches, resulting in a local increase in thickness. In the second part, two of three failures observed in industrial production are successfully reproduced with the default parameters. Subsequently, the Lankford Ratio is varied by ±10%, which leads to the occurrence of the final failure. This highlights a strong dependency on the Lankford Ratio.

Keywords: Finite Element Method, cold stamping, tensile tests, Ferritic Stainless Steels, Digital Image Correlation, anisotropy, yield criterion, Forming Limit Diagram;

Resumo

No passado, as matrizes de estampagem eram desenvolvidos por meio de um processo de tentativa e erro, as falhas eram identificadas e a geometria da matriz era ajustada posteriormente. Com o advento do Método dos Elementos Finitos (FEM), esse processo tornou-se mais eficiente, uma vez que o FEM passou a ser utilizado para simular e analisar os resultados. Paralelamente, a rigorosidade das normas de emissões automotivas aumentou a demanda por materiais adequados levando à adoção de margens de segurança mais rigorosas para atingir o peso desejado.

Neste trabalho, o FEM será utilizado para avaliar se as falhas observadas no processo industrial de estampagem a frio poderiam ter sido previstas. Para isso, serão realizados diversos ensaios de tração com o objetivo de caracterizar as propriedades dos materiais de dois aços inoxidáveis ferríticos (FSS), EN 1.4509 e EN 1.4512. Utilizando a Correlação de Imagem Digital (DIC), os coeficientes de anisotropia serão determinados e utilizados na modelação dos critérios de escoamento de Barlat (1989) e Hill (1948). O Diagrama de Limite de Conformação (FLD) será previsto com base nos métodos de Abspoel e Keeler. Por fim, serão realizadas simulações com o software Ansys Forming em duas peças estampadas distintas. A primeira envolve sete operações de conformação, enquanto a segunda se limita apenas à operação inicial. Na primeira peça, observou-se uma tendência aumentada à formação de rugas próximas aos entalhes, resultando em um aumento localizado de espessura. Na segunda peça, duas das três falhas observadas na produção industrial foram reproduzidas com as propriedades padrões. Em seguida, ao variar o coeficiente de Lankford em 10%, ocorreu a falha restante, destacando uma forte dependência da anisotropia na estampagem.

Palavras-chave: Método dos Elementos Finitos, estampagem a frio, ensaios de tração, Aços Inoxidáveis Ferríticos, Correlação de Imagem Digital, anisotropia, critério de escoamento, Diagrama de Limite de Conformação;

Contents

List of Tables

List of Figures

Chapter 1

Introduction

According to the European Commission, in 2020, the transport sector accounted for approximately 5% of the European Union (EU)'s total Greenhouse Gas (GHG) emissions, [1]. Furthermore, the sector provided employment to approximately 10 million individuals within the same year. While the sector's contributions are not entirely positive, they do represent a complex trade-off, as transport emissions also account for approximately 25% of the total GHG emissions, [1]. To address this issue, all 27 EU member states have committed to reducing 90% of transport related emissions by the year 2050, as outlined in the European Commission's Transport Green Deal, [1].

The car exhaust system plays a critical role in the emissions control process. Achieving the desired outcomes involves operating the emissions control catalysts at higher temperatures to ensure optimal conversion efficiency of the unburned carbon monoxide and the unburned hydrocarbons, [2]. In essence, the escalation in automotive emission standards has precipitated heightened discharge temperatures and the necessity for suitable materials, [2].

The main consequence is the rise in the corrosion damage and the loss of strength due to high temperature. In such instances, stainless steels, which possess an elevated degree of corrosion resistance demonstrates optimal performance, [3]. Modern ferritic stainless steels, such as the commercial grades 1.4509 and 1.4512 includes good formability, high corrosion resistance, and high strength at elevated temperatures.

In this context, several parts of automotive exhaust system are made by stamping processes. In the past, the design of forming processes was achieved through trial and error, relying heavily on the experience of skilled professionals, [4]. Since the creation of the FEM, it has been widely adopted by engineers worldwide to predict structural, thermal, chemical, and electrical behaviors. The stamping process is no exception, fabrication processes are also being simulated by FEM, [5]. It's so important as FEM has become an essential tool in optimizing and analyzing its outcomes.

The FEM can be used at several stages of the forming process, at the first stage the simulation can determine by a rough estimation if it can be formed or not. After that it can also be used to avoid some defects that appeared at the tryout stage, [5], [6] or in other words, at the performance analysis stage, [5].

To implement the FEM, various differential equations are employed to model and predict the behavior of the system under analysis. To achieve accurate results, it is essential to define appropriate boundary conditions and input material properties, which serve as the foundation for the simulation.

One of the most important material properties is the yield criteria which delimits the transition between the elastic and plastic behavior. The tresca and von mises criteria establishes an envelope that accounts for all possible stress combinations capable of causing ductile fracture in isotropic materials, [7]. However, these criteria are not applicable when dealing with anisotropic materials, as their mechanical behavior varies with direction, requiring alternative approaches for accurate analysis, [8].

The most used approach to measure the anisotropy coefficient is to perform tensile tests at zero or Rolling Direction (RD), forty-five or Diagonal Direction (DD) and ninety degrees or Transverse Direction (TD) with the RD to obtain the Lankford coefficient. This coefficient is a ratio which relates how true plastic thickness deformation is greater than true plastic width deformation, [9].

On one hand the vertical axis strain can be acquired quite easily by applying a traditional extensometer. On the other hand, it's not quite as easy to extract the horizontal axis strain by applying a traditional extensometer.

Typically, this objective is realized through approaches involving direct contact. Alternatively, the deformations in each direction can be obtained by employing non-contact methods.

One approach is the Circle Grid Strain Analysis, a technique developed by Keeler, involves the application of an electrochemical etching to coat the surface of the blank with circles of known diameter. The evaluation of strain levels in each section of the piece can be conducted through measurement subsequent to the straining process, [10]. Alternatively, a DIC technique that utilizes digital extensometers can be employed.

In summary, the aforementioned improvements have given rise to novel challenges within the industry, thereby necessitating the development of innovative solutions.

This work involves the simulation of the stamping cold work process using the FEM in the performance analysis stage, focusing on the anisotropic behavior of the material due to its prior rolling. The material properties will be characterized through tensile tests conducted in accordance with ISO 6892-1. Additionally, DIC will be employed to measure strain, and digital extensometers will be used to determine the Lankford coefficients (r-values). The extracted data will be integrated into the FEM to model the material's anisotropic deformation during the stamping process.

1.1 Goals

Contextualizing, some fractures were happening in the forming process of two pieces identified by the numbers x429 and x143. It's important to notice that this forming processes are already running in the industry and the main goal of this thesis is to verify if this fractures were predicted with the use of the FEM by a rough estimation.

In order to achieve these goals, a study of the material's behavior may be necessary. To characterize the material properties, several tensile tests will be conducted in different directions.

To facilitate understanding, the goals have been summarized in the following list:

- To carry out tensile tests according to ISO 6892-1 and ISO 10275;

- Understand the DIC method and the camera distortion effects to obtain the anisotropy coefficients;
- To model the anisotropic yield criterion;
- Implement the existing methods from the literature to forecast the FLC curve;
- Simulate by FEM the stamping process and verify if the fracture was expectated;
- By varying the anisotropy coefficients, understand how the anisotropy coefficients affects the stamping process;
- Present solutions to improve the drawability of the stamping parts.

These goals summarize a step-by-step used to reach the final goal of simulating the stamping process and can be seen in Fig. 1.1.

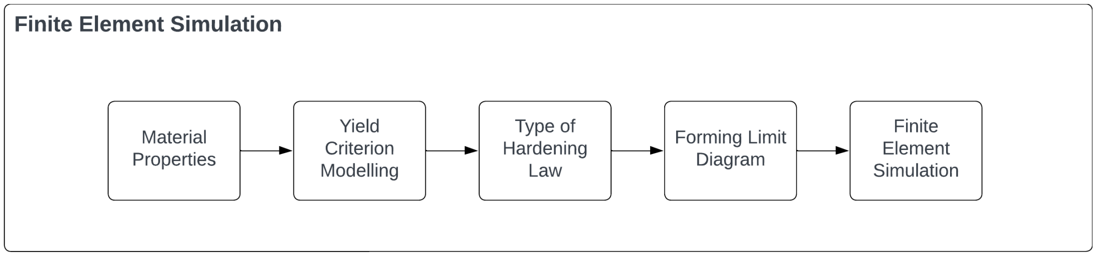

Figure 1.1: Step-By-Step

1.2 Documents Structure

The document is composed of five main chapters.

This chapter is devoted to the introduction of the theoretical framework and the problem under consideration.

The second chapter encompasses the state of the art and the theoretical foundation that were utilized in the development of this work. This chapter provides a comprehensive overview of the theoretical underpinnings of stamping, digital image correlation, anisotropy and finite element simulation.

The third chapter of this study delineates the methodological framework employed to achieve the delineated goals and objectives.

The fourth chapter is where the results and discussions are located. This includes the results from the tensile test, DIC, yield criterion modelling and the simulations.

In the conclusion, the final chapter offers a comprehensive synthesis of the most salient conclusions derived from this study.

Chapter 2

Theoretical Foundation

2.1 Stainless Steels behavior according to crystalline structure

The classification of an iron alloy as stainless steel depends on the presence of chromium in the alloy's composition, with a minimum requirement of 11% chromium, [11]. Chromium reacts with the oxygen in the atmosphere, forming a chromium oxide layer on the material's surface. This phenomenon is known as passivation, when it occurs it prevents the oxygen from reacting with iron, thus preventing corrosion.

The passive protective layer is susceptible to damage from scratching, however, it possesses the ability to self-repair through contact with air. Consequently, this material is widely adopted by the industry, because of its high corrosion resistance and the aesthetic appearance.

It is employed in industry in different sectors such as vehicle frames, wagons, conveyors, power generation and mining, [12].

Stainless steels can be classified into ferritic or austenitic according to their crystalline structure. It's well known that ferritic steels have a body centered cubic structure(BCC) and austenitic steels have face centered cubic crystalline structure(FCC), [13].

To achieve the austenitic phase, generally nickel or nickel-equivalent elements are used to stabilize the γ-phase. In contrast FSS grades generally are stabilized by addition of chromium or chromium-equivalent elements. This makes austenitic grades more expensive due to the their higher nickel contents, [12], [14]–[16].

FSS outperform austenitic grades in certain applications because of the lower linear thermal expansion coefficient and the higher thermal conductivity, [12], [15]. In addition, ferritic steels tend to have a higher resistance to cyclical thermal loading, [3], [14], [15].

In FSS the application of tensile stress in the RD gives rise to a phenomenon known as ridging or roping, [14], [17]. This results in the formation of a corrugated surface, which appears parallel to the rolling direction. In turn, it leads to a reduction in the sheet's overall surface quality, [18], [19]. The only method of addressing this issue is through polishing, which occurs subsequent to the formation of ridging, [14], [19]. Therefore, it is essential to prevent the occurrence of this phenomenon, particularly in components that are of aesthetic importance, [19].

In the context of forming, FSS tends to have the same formability as plain carbon steels. On the other hand, austenitic crystalline structures provide a higher formability due to martensite transformation, [20]–[22]. The FSS tends to have a maximum 35% of plastic deformation which limits its FLD.

Steels with a ferritic crystalline structure tend to have better deep drawability than those with an austenitic crystalline structure, while austenitic steels tend to have better stretchability, [14].

2.2 Exhaust System Requirements and Parts

The exhaust system is essentially composed by several parts. This parts can be seen in Fig. 2.1.

The exhaust gases enter the exhaust manifold and then pass through the primary or flexible pipe, which helps isolate engine vibrations. Next, the gases flow to the catalytic converter at high temperatures to ensure the complete breakdown of harmful gases. After that, they pass through the resonator, which reduces engine noise by canceling out certain sound frequencies. Finally, the gases exit through the muffler, which further dampens sound before the gases are released into the atmosphere, [3].

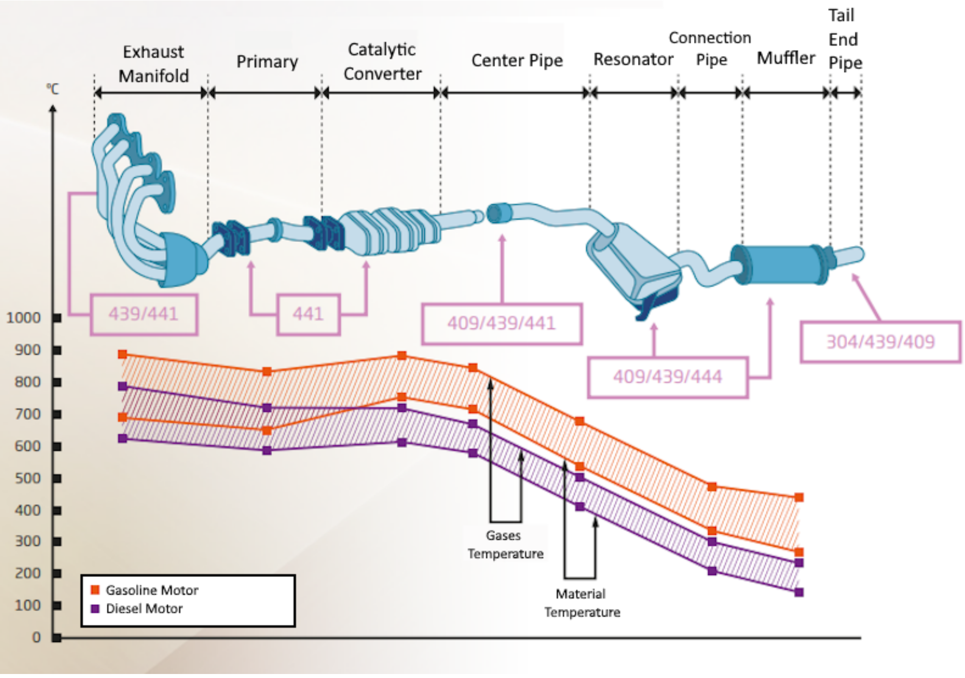

Figure 2.1: Inox in the Exhaust System

Source: Adapted from Aperam Inox, [23]

As the gases pass through the exhaust system components, their temperature gradually decreases, which affects the material requirements for each section. Depending on the specific function and operating conditions of each part, different materials are used. The exhaust system is generally divided into two sections: the hot end and the cold end, [3].

The hot end, which includes components near the engine such as the exhaust manifold and catalytic converter, must withstand high temperatures and requires materials with excellent thermal fatigue strength, oxidation resistance, and salt corrosion resistance at elevated temperatures. In contrast, the cold end of the exhaust system, including parts like the muffler and tailpipe, operates at lower temperatures and primarily requires oxidation and salt corrosion resistance, [3].

2.3 Sheet metal-working Processes

Metal forming is a family of processes that plastically shape materials without adding or removing material, essentially changing the shape of the material while maintaining its mass. Two major metal forming processes are rolling and sheet-metal processes.

Components are typically designed to operate within their elastic limit, incorporating a safety factor to ensure reliability. However, in forming processes, exceeding the elastic limit is necessary to achieve the desired shape. Consequently, the property which limit the formability is the maximum strain which an material can sustain.

Metal forming processes are classified as hot forming or cold forming, depending on whether they are conducted above or below the recrystallization temperature. Hot working relieves residual stresses but reduces dimensional accuracy, whereas cold working improves dimensional precision but increases residual stresses and work hardening effects, [24].

2.3.1 Rolling influences in the microstructure

Rolling is a process where a metal workpiece is passed through rollers to reduce its thickness. It is widely used in the industry due to its efficiency and capability for continuous production, [25]. However, one drawback of rolling is the development of anisotropy in the final product, caused by the high plastic deformations involved, [26]. As a result, material properties can vary depending on direction. In heavily deformed materials, the rolling direction becomes visually and structurally apparent, [27].

During rolling, metal grains elongate and align along a preferred crystallographic direction. This leads to texture strengthening, which enhances the material's strength but introduces directional dependence in its properties, [17], [22]. Therefore, when designing components or tooling, the rolling direction must be considered to prevent premature failure or manufacturing issues, [28].

Maruma *et al.* study examined the influence of both cold working and annealing temperature on various parameters, including the anisotropy of an AISI 441 metal sheet.

The results indicated a positive correlation between the increase in cold working and the increase in $\bar{r}$, [29].

2.3.2 Stamping and Cutting

Sheet metal processes include both stamping and cutting operations. These are typically carried out using a stamping press, where a die set shapes or cuts the material into the desired form, [24].

The die set used in stamping usually consists of three key components and can be seen in Fig. 2.2:

- Die – The lower tool that contains the negative shape of the final part. It provides the cavity where the sheet metal is shaped.
- Punch – The upper tool that presses the sheet metal into the die, forming or cutting the metal.
- Binder (or Blank Holder) – A piece that holds the sheet metal in place to prevent excessive movement or wrinkling during the stamping process.

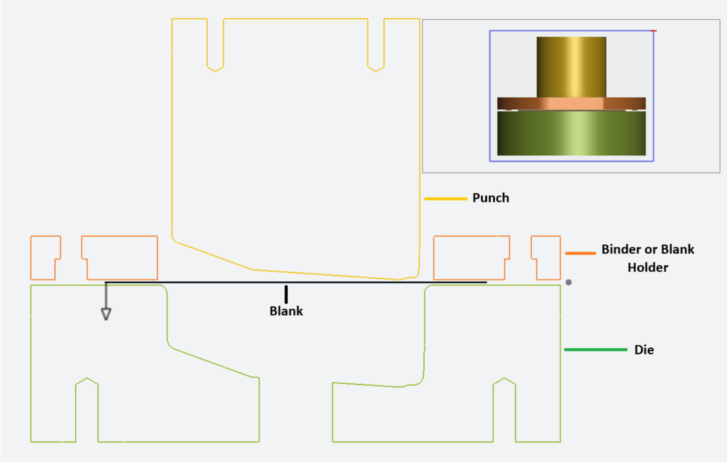

Figure 2.2: Stamping Die set

There are two ways of performing a stamping process, in a single phase or in multiple phases called by sequential stamping. When stamping the material's FLC highly depends on the strain path. It means that when realizing a sequential stamping process, the material can deform more than usual before leading to failure or to a critical necking.

Morais, Corrêa, and Lopes investigated the effect of the strain path on AISI 409 and observed an increase in the power-law hardening exponent n depending on the strain-path, [30].

Failure modes in metal forming can be categorized into three main types: Stress-Induced Defects (SID), Flow-Induced Defects (FID), and Material-Related Defects (MRD).

SIDs result from improper stress states during deformation. These can be:

- External, such as necking, fractures, excessive thinning or thickening, buckling, wrinkling, distortion, and springback;
- Internal, such as the formation of micro-voids and cracks due to localized stress concentrations.

SID are especially common in thin-walled components (sheet metal and tubes) due to their low stiffness and susceptibility to stress concentrations, [31].

FID arise from irregular or insufficient material flow. These defects include:

- External issues like buckling, folding, overfilling, underfilling, and surface imperfections;
- Internal problems such as flowline disruptions, laps, and flow incompatibility in composite materials.

FIDs are particularly prevalent in bulk-forming processes. Contributing factors include tool design, friction conditions, and processing velocities, all of which are critical in achieving defect-free thin-walled components, [31].

Microstructure-Related Defects (MRDs) originate at the microstructural level and affect both the internal and external quality of formed parts:

- Internal defects may involve abnormal grain structures, undesirable phase compositions, and non-uniform recrystallization.

- External manifestations include surface anomalies like orange peel, Lüder bands, and roping.

MRDs influence the mechanical properties of the final part and typically stem from initial material characteristics (inclusions, grain boundaries). Under certain stress and strain conditions, MRD can evolve into SID or disrupt material flow, thereby leading to FIDs, [31].

2.4 How the traditional tensile test is carried out?

In a tensile test an specimen is subject to an increased tension load until rupture. The final objective of this test is to collect some quantitative data about the material and characterize their properties.

While the test happens all the data is being stored to plot a curve that relates stress σ and strain ε of the specimen.

There are two types of stress-strain curves, in one hand the engineering-strain engineering-stress curve that only consider the initial area and in the other hand the true-stress true-strain curve which consider the instantaneous area, [32]. For most cases, the engineering stress curve suffices, but when dealing with stamping, true-stress curves might need to be considered, [33]. It happens essentially because of the approximation characteristic of the engineering curve.

An stress test could be subdivided in three or four different regions.

The initial interval is characterized by the material's exposure exclusively to elastic deformations, as stipulated by Hooke's laws. During this interval, the material undergoes a return to its original form upon the removal of a certain load.

The elastic limit point is determined by yield criteria, which delineate the transition between elastic and plastic deformations. It is noteworthy that certain materials exhibit a clearly defined yield stress, while others do not manifest it. When a material doesn't show a defined yield criteria by a plateau, generally it's obtained by the intersection between the curve and a line with the same slope than the elastic modulus offset by 0.2% of strain.

Then the second interval are dictated by the work hardening and flow rules. This interval is ruled by volume continuity as the volume changes are almost insignificant.

$$\frac{\partial V}{\partial t} = \frac{\partial V_x}{\partial t} + \frac{\partial V_y}{\partial t} + \frac{\partial V_z}{\partial t} \tag{2.1}$$

2.5 Digital Image Correlation

A DIC refers to any non-contact methods who involves acquiring images, storing and post-processing to retrieve a full-field shape, deformation and/or motion measurements. When only one camera is used it's called by 2D-DIC. However when two or more cameras are employed this is called by stereo-DIC.

To achieve this results, a random speckle pattern must be applied to the surface being analyzed. This speckle pattern will be processed by a correlation matrix which correlates between subsequent frames the position of each pattern.

In some type of applications, there are some difficulties associated with adopting direct contact methods. In such cases the employment of DIC is recommended.

When stereo-DIC approach is used, two images with different angles of the same object are captured and by triangulation the three dimensional coordinates estimated. Then by using a correlation matrix, the coordinates of each of those points are related.

One of the barriers to employ this method is associated with some difficulties in synchronizing the time of two images and triangulate their coordinates.

When the 2D-DIC is employed, the synchronizing barrier is avoided and the cost is much cheaper despite the fact that this method is only limited to planar surfaces. And then, by using the same approach the coordinates of each pattern are related.

The main consequences of employing only one camera is the impossibility to capture out-of-plane motions. Even in a simple tensile test several source of errors which can cause out-of-plane motions can be listed: Poisson effect, local necking, bending and planar deviations, [34]. The effect of the out-of-plane motions and this source of errors were intensively studied by Sutton et al., [34].

To acquire this images a camera may be needed. Depending on the quality and purpose of the camera lenses it could introduce errors.

The technology evolved to a point where sub-pixel resolutions are used, [35].

There are several works in the literature which uses 2D-DIC and creates a digital extensometer to quantify anisotropy. Some of this authors don't even mention the camera calibration process, [36], [37]. Others consider the camera calibration process during the 2D-DIC processes, [38].

2.6 Camera Models and Calibration Process

The pinhole camera model is the simplest camera model, which assumes that light travels in a straight line through a small hole and forms an inverted image on the opposite side. However, because the hole cannot be made infinitely small, multiple rays from the same point on an object can pass through at slightly different angles. This causes a slight blurriness in the image, as the rays diverge and fail to converge perfectly on a single point on the imaging plane.

Modern cameras use a lens-based model to focus light rays precisely, resolving the primary issue of blurriness found in the pinhole camera model. However, lenses introduce new challenges, such as the fact that they can only achieve sharp focus at a specific distance, known as the focal distance. Additionally, the assumption of an ideal, infinitesimally thin lens can lead to distortions. For example, tangential and radial distortions may occur, where light rays bend unevenly. When magnification increases outward from the center, the effect is called barrel distortion, and when it decreases inward toward the center, it is called pincushion distortion.

To effectively eliminate camera distortion and ensure that it doesn't affect strain measurement results, camera calibration might be needed. Camera calibration involves removing distortions by remapping all the pixels in a image by a function, [39].

Traditionally, ten to twenty images with a checkerboard are used to calibrate the camera. The algorithm recognizes the corners and verify if all the lines are straight.

Wang, Jiang, Wanintrudal, *et al.* carried out a tensile test using the 2D-DIC technique and for the camera calibration he used 3-6 images, [38].

Zhang proposed a simple method for camera calibration which involves three parameters for radial distortion, three for tangential distortion and the camera matrix and this method is widely implemented in libraries for example in OpenCV 4.1, [40].

2.7 Anisotropy

Any material who has the same properties independent of the direction of analysis is called by isotropic. When a material has properties in which depends in the direction of analysis is called by anisotropic.

There's different types of anisotropy which includes transverse anisotropy and orthotropic. When a material has different properties along three orthotropic axis the material has orthotropic anisotropy. In rolled metals sheets there's three main different anisotropic directions and they are RD, Normal Direction (ND) and TD, [41].

The most used approach to determine the anisotropy ratio in orthotropic sheets is to perform the tensile test along different directions. Fig. 2.3 shows how the specimens are taken from the blank sheet. RD, DD and the TD.

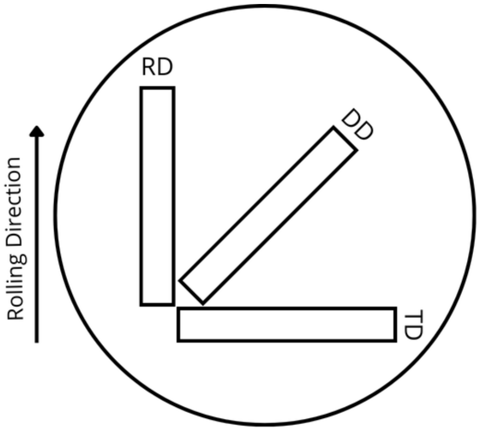

Figure 2.3: Specimen according to the angle with Rolling Direction

FSS are known to have to a high anisotropic mechanical properties, while austenitic stainless steel to have a much lower anisotropy, [14]. Additionally, the anisotropy can exert a positive or negative influence on the forming processes.

The primary property that governs the formability of a metal sheet is the phenomenon of localized necking [42]. If the material is considered to be isotropic, the thickness strain and the width strain tends to be equal. However, in anisotropic materials this ratio is different from one. Consequently, by verifying how the plastic thickness strain behaves it can be evaluated how fast the material becomes thinner and leads to a localized necking.

To evaluate the localized necking behavior the most used approach is to measure the Lankford coefficient. Several terms have been proposed in the literature to describe this anisotropy coefficient, including plastic strain ratio and r-value. This property is defined as the ratio of true plastic width strain to true plastic thickness strain as shown in Eq. 2.2. In other words, it represents how much more the material elongates in width (ε_{pb}) compared to its thinning in the thickness direction (ε_{pa}).

$$r = \frac{\varepsilon_{pb}}{\varepsilon_{pa}} \tag{2.2}$$

$$\begin{cases} \text{r>1,} & \text{the width strain more than the thickness} \\ \text{r=1,} & \text{they strain at the same rate} \\ \text{r<1,} & \text{the material strain more in thickness than width.} \end{cases} \tag{2.3}$$

Thickness can be measured in two different ways. The first is to measure the thickness directly using an extensometer or by the constant volume assumption. Since it's easier to measure length and width than thickness, the constant volume assumption is usually used, [43].

Two important indices for evaluating the formability of a material can be extracted from its anisotropy: the average plastic strain ratio, $\overline{r}$, and the planar anisotropy, Δr.

The formula used to calculate the planar anisotropy is shown in Eq. 2.4. This value reflects the material's tendency to develop wrinkling or earing during forming. Some authors have also associated Δr with a material's resistance to ridging, particularly in cases where ridging is known to develop, [44].

When this value is negative, the material tends to form ears at 0° or 90° relative to the RD. When it is positive, earing tends to occur at 45° to the RD. Finally, when the value is close to zero, the material exhibits minimal earing.

$$\Delta r = \frac{r_0 - 2r_{45} + r_{90}}{2} \tag{2.4}$$

The average plastic strain ratio ($\overline{r}$) indicates how well a material performs in deep drawing processes. In general, the higher the $\overline{r}$, the better the material's deep drawability. Eq. 2.5 shows how this index is calculated.

$$\overline{r} = \frac{r_0 + 2r_{45} + r_{90}}{4} \tag{2.5}$$

Other indices, such as the limit drawing ratio (LDR), can also provide valuable insights into material formability, but they are beyond the scope of this work.

2.8 Anisotropic Yield Criteria

The yield criterion defines the transition between elastic and plastic deformation. The two most widely adopted criteria were formulated by Von Mises and Tresca. Both are valid only for isotropic materials. In the Huber–Von Mises criterion, failure occurs when the system reaches a certain deformation energy defined by a contour line. It is well known that the Tresca criterion is generally more conservative than Von Mises, [7].

The Eq. 2.6 shows the method for obtaining the equivalent stress according to Von Mises.

$$\sigma_v = \sqrt{\frac{1}{2}\left[(\sigma_{11}-\sigma_{22})^2 + (\sigma_{22}-\sigma_{33})^2 + (\sigma_{33}-\sigma_{11})^{2`} + 6(\sigma_{12}^2 + \sigma_{23}^2 + \sigma_{31}^2)\right]} \tag{2.6}$$

These yield criteria relates the state of stress with the failure condition. In a plane stress state σ_3 is equal to zero and the σ_1 and σ_2 are the principal stresses. Note that this terms refers to the principal stresses and can or not coincide with x, y and z axis.

However when dealing with anisotropic materials different approaches and yield criteria are needed. The most known yield criteria for anisotropic systems is the Hill Yield Criterion 1948 (Hill48) (Eq. 2.7) . This criteria consider coefficients which changes the proportionality of the Von-Mises envelope. Consequently, Von-Mises envelope is a particular case of the Hill48, [45]. More details will be shown in Chapter 3.

$$2f(\sigma) = F(\sigma_{yy}-\sigma_{zz})^2+G(\sigma_{zz}-\sigma_{xx})^2+H(\sigma_{xx}-\sigma_{yy})^2+2(L\sigma_{yz}^2+M\sigma_{zx}^2+N\sigma_{xy}^2) = 1 \tag{2.7}$$

Further, Barlat and Lian succeeded in proposing a contour which takes into account the crystalline structure of the material. And they demonstrated that when the exponent m equals to two it coincides with the Hill48. They also determined that $m = 6$ when the crystalline structure is body centered cubic, [46]. Eq. 2.8 shows Barlat89. Refer to **??** for more details.

$$f(\sigma) = a\left|K_1 + K_2\right|^M + a\left|K_1 - K_2\right|^M + c\left|2K_2\right|^M = 2\overline{\sigma}^M \tag{2.8}$$

Lou, Bae, Lee, *et al.* compared the performance of several yield contour equations and found that the Hill48 and Barlat89 models do not accurately predict the biaxial stress state, [47].

As materials harden, the initial yield criterion evolves and the yield surface expands. The isotropic hardening law is one of the most common approaches and assumes that as the material plastically deforms, the yield surface expands symmetrically. Fig. 2.4 shows how the yield contour evolves during plastic deformation, [48].

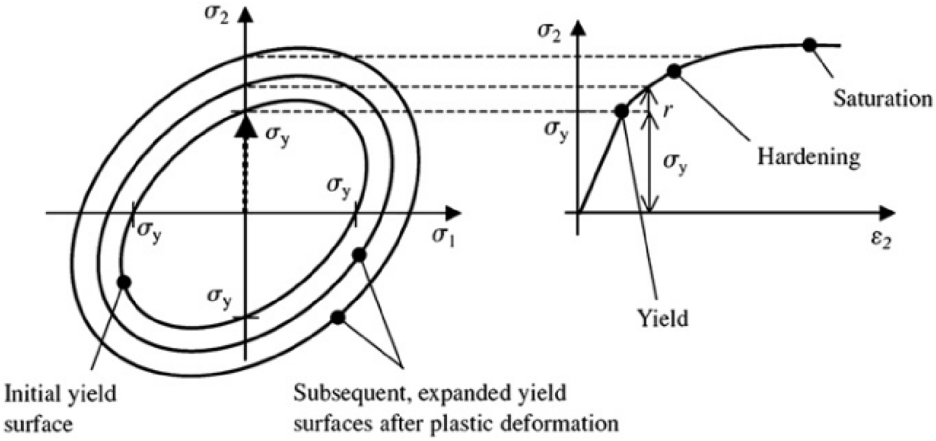

Figure 2.4: Isotropic Hardening Law

Source: [48], [49]

2.9 Forming Limit Diagram

Essentially, the state of strain can be expressed by the following relations,

$$\varepsilon_1 \geq \varepsilon_2 \geq \varepsilon_3$$

Where ε_1, is the largest principal strain, ε_2 is the intermediate principal strain and ε_3 is the smallest principal strain. In a plane-stress condition, ε_1 is the major strain and ε_2 is the minor strain.

During the forming operation, the material undergoes plastic deformation. The extent to which the material can be formed is limited by the amount of strain it can sustain. Once this strain exceeds a certain threshold, localized necking occurs, leading to failure. This failure criterion is described by the forming limit curve (FLC), which defines the combinations of major and minor strains that result in failure. These strain combinations are typically represented in a forming limit diagram (FLD) [42].

The FLD contains the onset necking under different loading conditions. For example, the tensile test only presents the onset necking under an uniaxial load. Although, sheets subjected to forming processes are subjected to different loading conditions in different parts of a piece even in the same process. Fig. 2.5 shows an example where some parts can be experiencing uniaxial loading, while others can be experiencing biaxial stretching. Further, the same part can be experiencing different stress state and strain state.

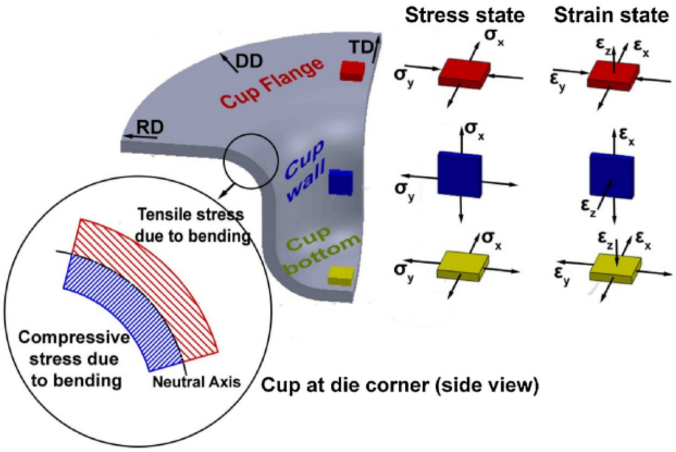

Figure 2.5: State of Stress and Strain

Source: [50]

The left side is associated with the drawing and the right side is associated with stretching conditions. The most relevant points to determine are the equibiaxial tension, uniaxial tension and plane strain(FLD_0). Fig. 2.6 shows the FLD with the defined conditions.

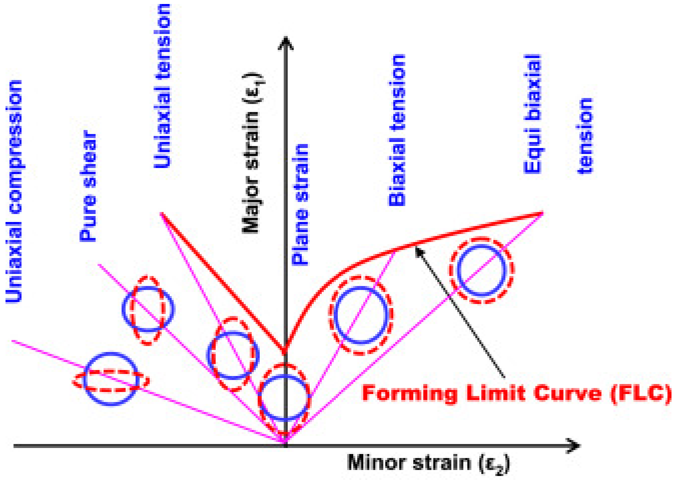

Figure 2.6: Forming Limit Diagram loads

Source: [42]

The most widely adopted experimental procedure for determining the FLD is the Nakajima test, as described in ISO 12004-2. This method involves deforming flat sheet specimens of varying gauge widths using a hemispherical punch with a radius of 100[mm], until necking or fracture occurs. By adjusting the specimen width, different strain paths can be obtained, ranging from uniaxial to equibiaxial tension, **iso12004-2**. Fig. 2.7 illustrates the variation in specimen geometry used to achieve different loading paths and their corresponding positions on the FLD.

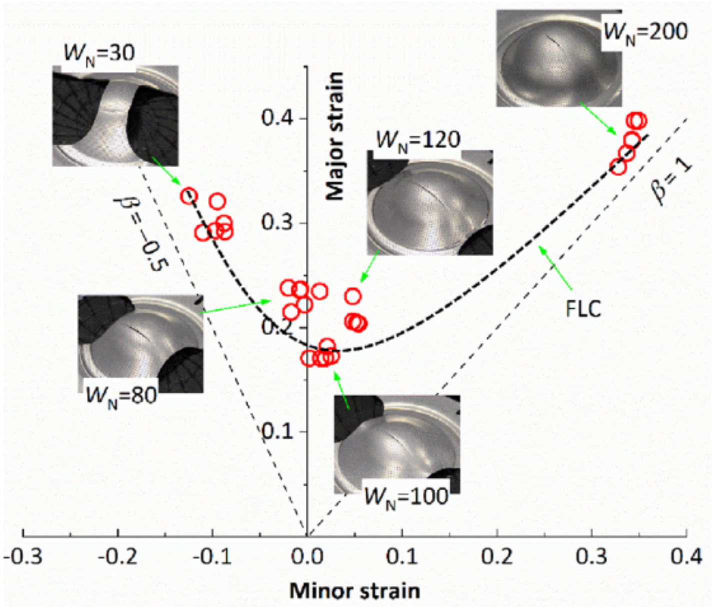

Figure 2.7: Nakajima Test Specimens compared to the FLC
Source: [51]

Each region of the FLD also represents a specific tendency, the Fig. 2.8 specifies each the associated effects for each region of the FLD. For more details associated with the FLD refer to the following reference, [42].

It is important to note that, in practice, industries often use thinning as a constraint during the forming process. Additionally, a safety margin is applied to ensure that the material does not fail. To incorporate this safety margin, the FLC is usually reduced by a certain percentage.

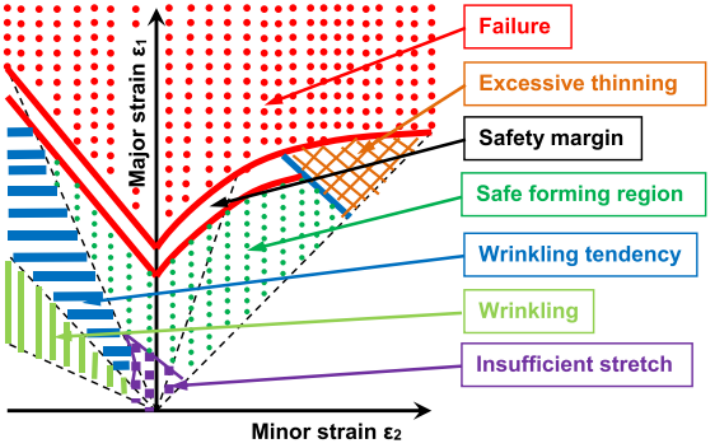

Figure 2.8: Forming Limit Diagram Regions

Source: [42]

Some difficulties have been associated with the Nakajima test, as it is time-consuming and requires a large amount of material. Consequently, various alternative approaches have been proposed in the literature to predict forming limit curves (FLCs).

Among these, well-established methods include the Keeler and Brazier, and Abspoel techniques, [52], [53].

Furthermore, the incremental sheet metal stamping process cannot be accurately described using the conventional FLC. In such cases, the fracture forming limit curve (FFLC) is typically employed. However, in a contrary way of the FLD, methods for obtaining the fracture forming limit curves have been not standardized yet, [51].

2.10 Ansys Forming and Finite Element Method

Essentially the software Ansys Forming is a graphic user interface(GUI), which uses the LS-DYNA solver. This software facilitates the developing the stamping line in the well known solver LS-DYNA. Thereby, the GUI includes several phases.

This software utilizes the FEM which consists in dividing the problem which the we want to analyse in smaller problems.

The first is the process definition, which includes the stamping line processes definition (blanking, drawing, stretching, trimming, flanging or restriking). In this phase several steps can be added. Also, the finite element solving parameters can be configured and three main configuration are presented(fast solving, accurate and very accurate). This basic configurations includes the shell element type, time steps(explicit or implicit), contact stiffness, the tool element size, tool max velocity. In this step is also when a rough alignment of the tools is applied.

By default, the shell types for accurate solving are as follows: two for the explicit solver and sixteen for the implicit solver. Shell type 2 is associated with a physically stabilized solution that provides faster performance than fully integrated elements, while maintaining acceptable convergence time and accuracy compared to fully integrated elements, [54]. On the other hand, shell type 16 refers to the Bathe-Dvorkin element, which is a fully integrated element. For more information on this element, refer to, [55].

Next, the blank and material definitions, this is where the geometry of the blank is defined and the meshing process is performed.

The quality of the mesh will be particularly important to the accuracy of the analysis. The mesh can be either uniform or non-uniform. There is a particular case of non-uniform analysis called by Adaptive Mesh Refinement (AMR), [56]. AMR refers to the process of modifying the mesh during a simulation to improve accuracy or efficiency. This adaptation can be static (before the simulation) or dynamic (during the simulation), based on various error indicators or solution features.

There are two types of adaptive mesh refinement: p-refinement and h-refinement. The h-refinement (mesh refinement) refers to dividing each element into smaller sub-elements, thereby reducing the element size locally. In contrast, p-refinement involves increasing the polynomial order of the basis functions within the same element without changing the mesh topology. Both methods aim to improve solution accuracy by adapting the discretization according to the problem's local requirements, [57].

After defining the mesh, the next step is to specify the material properties. These include the elasticity modulus (E), the yield criterion model, the hardening law, and the forming limit curve (FLC) model.

Next, the tools are aligned and positioned, and their behavior is defined for each phase of the stamping process.

Finally, the simulation can be run.

2.11 Related Works

Recently, Krevicz tested a variety of materials and applied the DIC technique to obtain the Lankford Coefficients. He also obtained the FLC curve by using the Nakajima Test and compared with numerical simulations. Last, he reported a high degree of dependence on thickness in regard to the effects of anisotropy. Although, he doesn't succeeded in simulating the FLD, [37].

Barros successfully simulated forming processes involving advanced high strength steels using Stampack software. He proposed a modification to the geometry of the stamped part to address potential failure issues. Additionally, he identified significant variability in the material properties depending on the batch, and concluded that traditional tensile tests are not sufficient to fully characterize the material, as microstructural effects play a relevant role, [58].

Chapter 3

Materials and Methods

3.1 Material Properties Characterization

This section details the methodology for characterizing the material properties. First, an analysis of the metal sample based on its chemical composition will be presented. Next, the specimen preparation process for the tensile tests will be described, including the modifications required to enable the DIC technique. Finally, the setup used to perform the DIC measurements will be outlined. At the end, the post-processing of the acquired data will be presented.

Additionally, Fig. 3.1 shows an schematic to facilitate understanding.

3.1.1 Metal Sample

The company Catraport provided metal sheet samples of AISI 1.4509 and AISI 1.4512, both of which are ferritic stainless steels. These metal sheets are used in the production of exhaust system components through cold stamping. The supplier of the material is THYSSENKRUPP MATERIALS IBERICA S.A.

The metal is supplied in coil form, which is then cut into blanks of dimensions that maximize material utilization. The dimensions and quantity of the samples are presented in Tab. 3.1.

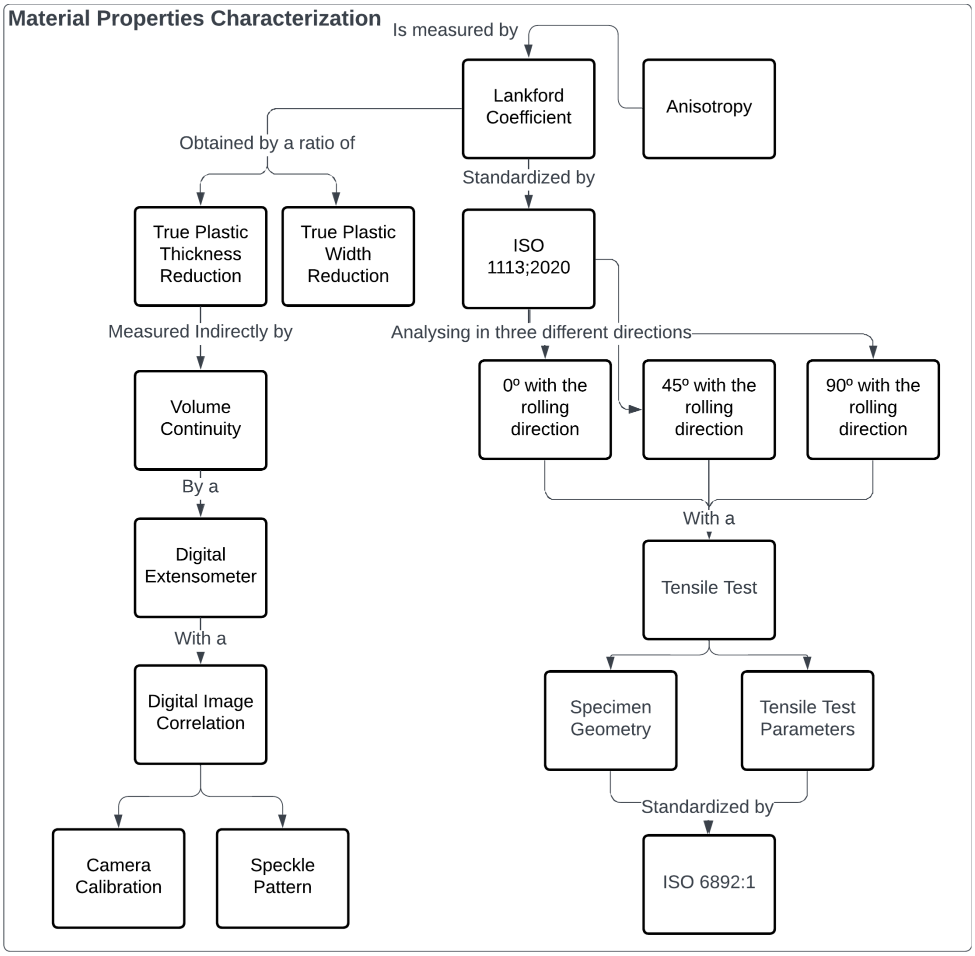

Figure 3.1: Material Properties Characterization Schematic

It's important to mention that this material, was not working correctly as it was leading to some failures in the cold stamping process. This material properties might be biased downward.

Material	EN 1.4509	EN 1.4512
Thickness t	$3.0[mm]$	$1.2[mm]$
Diameter $\varnothing$	$240.0[mm]$	$200.0[mm]$
Samples	6	5

Table 3.1: Dimensions of the provided metal sheets

The names of the stainless steels by chemical composition is standardized by European Standard EN 10088-1. EN 1.4512 and 1.4509 are equivalent to X2CrTi12 or AISI 409 and X2CrTiNb18 or AISI 441, respectively. The Table 3.2 shows the maximum chemical composition of each material according to EN 10088-1.

EN	%C	%Si	%Mn	%P	%S	%Cr	%Nb	%Ti
1.4512	0.030	1.00	1.00	0.040	0.015	10.5…12.5	-	$[6(C+N)]\ldots 0.65^{C}$
1.4509	0.030	1.00	1.00	0.040	0.015	17.5…18.5	$[3C+0.30]\ldots 1.00$	0.10…0.60

Table 3.2: Maximum Chemical Composition for EN 1.4512 and EN 1.4509

Source: Adapted from EN 10088:1, [13].

Each one of this elements has an important role on their formability. Usually, the amount of carbon is limited to around 0.1% as an increase in the amount of carbon could lead to an increase in the strength, reducing the formability[27].

There is two mainly families of elements which can alter the Fe-C diagram and helps developing differents phases γ or α which represents the austenitic and the ferritic phases of the steel, respectively. The first group is the austenitizing elements like Ni, N and C, and the ferritizing elements such as Cr, Ti, Nb, V, Al[17].

It can be clearly seen that both of this FSS have defined minimum limits related to the ferritizing elements (Cr, Nb and Ti) and a maximum amount of austenitizing element(C).

Two undesirable elements are the phosphorous and sulfur, this elements increases the chances of cracking and splitting, for example commercial-quality contains less than 0.035% P and 0.040% S. [27]

Titanium and niobium are alloy elements which helps developing a higher r, preventing the thinning during forming operations. Both of them helps the formation of carbides and nitrides[27].

Summarizing, many of this elements helps developing the desired ferritic phase.

The datasheet of the provided metal sheets are in annex. The chemical composition of each of this materials are shown in Tab. 3.3 and have been obtained from the metal datasheet.

EN	%C	%Si	%Mn	%P	%S	%Cr	%Nb	%Ti	%Ni	%Mo	%N
1.4512	0,010	0,55	0,39	0,020	0,001	11,47	0,008	0,240	0,140	0,035	0,012
1.4512	0,011	0,63	0,31	0,024	0,001	11,44	0,008	0,190	0,210	0,035	0,010
1.4509	0,014	0,50	0,31	0,025	0,001	17,82	0,37	0,14	0,250	0,060	0,017
1.4509	0,014	0,46	0,32	0,025	0,001	17,66	0,36	0,12	0,350	0,065	0,016

Table 3.3: Sample Chemical Composition

All this properties are according to EN 10088-1 as seen in Fig 3.2. The properties have been normalized according to the limits to ascertain their proximity to the limits. It is important to note that the nickel, molybdenum, and nitrogen elements do not have established limits and are therefore not included in the normalization process. Note that the niobium also don't have a defined interval Tab. 3.2

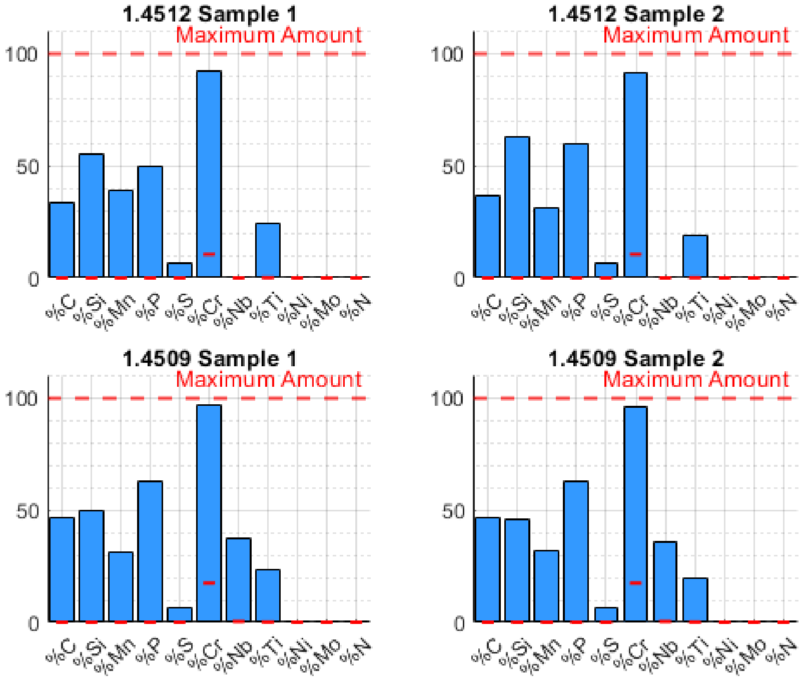

Figure 3.2: Normalized Chemical Composition

3.1.2 Specimen Preparation

The first part of this section consists of preparing the tensile test specimen. The dimensions range and the tensile test parameters are defined by ISO 6892-1:2009[59]. The ISO 6892-1:2009 contains all the details about the preparation of the tensile test specimen. Fig. 3.3 shows the details.

The chosen method for specimen preparation is punching. According to ISO 6892-1, materials with high work-hardening should not be prepared using this method [59]. However, the strain-hardening coefficient of the selected materials has been verified in the literature, justifying its use. Experimentally, Pisano determined the n-value of AISI 1.4509 to be approximately 0.22˘0.23 [60]. Similarly, Adriano reported comparable values ranging from 0.16 to 0.20 and from 0.15 to 0.24 for AISI 1.4509 and AISI 1.4512, respectively [37].

The metal sheets were cut initially in bands by a a guillotine. This cutting process, is referred as shearing. As it is mechanically calibrated, a test coupon was used to achieve

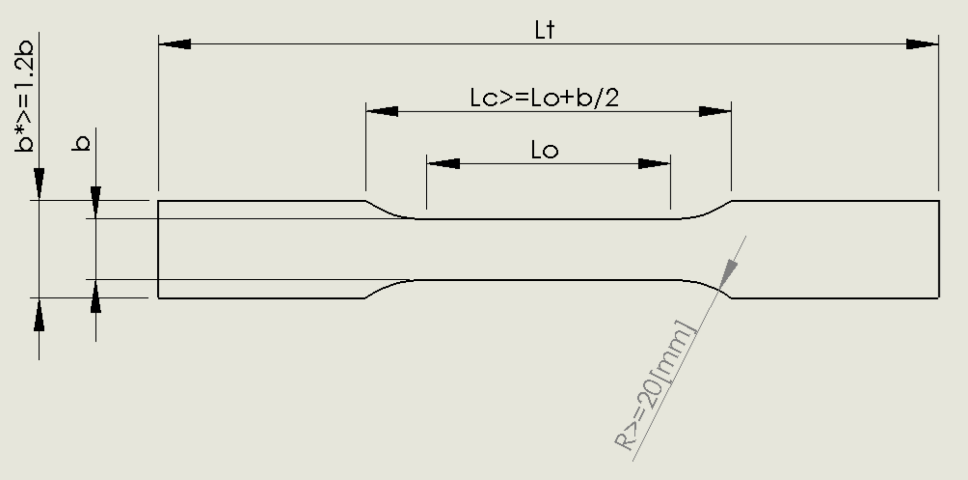

Figure 3.3: Specimen Dimensions According to Annex B

the desired dimensions and ensure that the maximum number of bands could be obtained.

With the assistance of the CAD Software Solidworks, the distance which maximizes the number of bands per metal sheet were obtained. Then the bands were die-cutted. Fig. 3.4 shows the planned SolidWorks model alongside the actual results for the smaller blank.

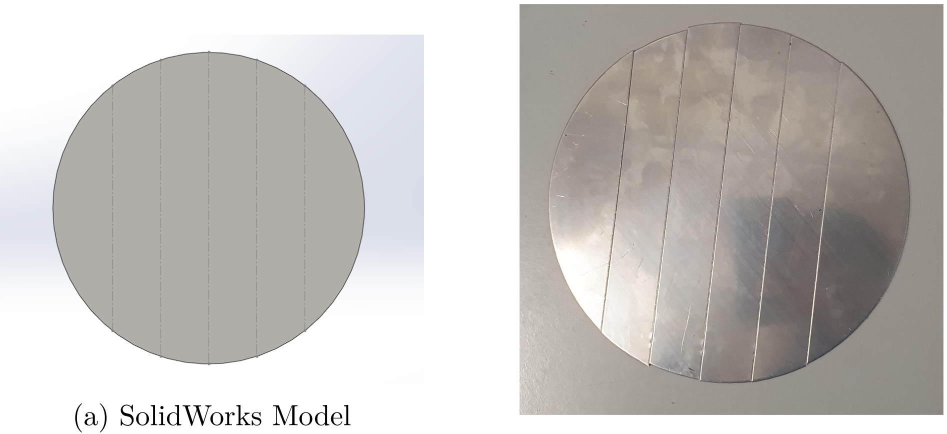

(a) SolidWorks Model

(b) Band Cutted

Figure 3.4: CAD Model and the achieved result

Then the bands were die-cutted by a press-anvil. The die with different mechanical clearance is shown on Fig. 3.6. The Fig. 3.5 shows the machine used to prepare the samples.

Figure 3.5: Laboratory Press MonTech LP 3000

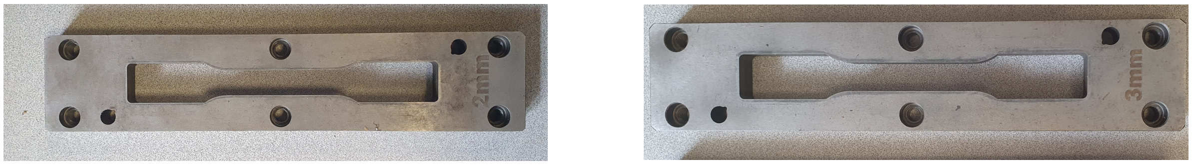

(a) 2mm Mechanical Clearance

(b) 3mm Mechanical Clearance

Figure 3.6: Interchangeable die with mechanical clearance up to 2mm and 3mm

The die and the punch are shown in the Fig 3.7. Right under the punch the interchangeable die for different mechanical clearances can be seen.

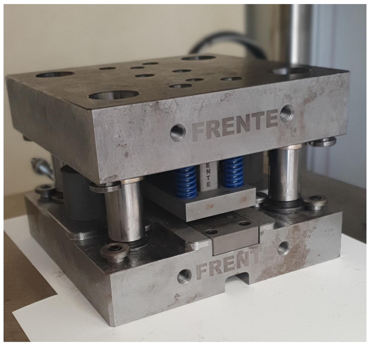

Figure 3.7: Die and Punch

The Fig. 3.8 shows the CAD model of the specimens in comparison to the real geometry.

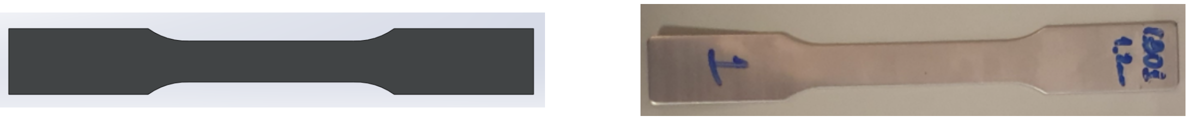

(a) CAD Model

(b) Tensile Test Specimen

Figure 3.8: Comparison between the CAD and the real specimen.

After producing all the specimens, they are disposed in a single frame in Fig. 3.9. Note that each one is being identified by it's own thickness and with the angle with the rolling direction.

Figure 3.9: Specimens grouped by different directions

The specimens were measured before applying the ink layer, as it could affect the dimensions. Each dimension needed to obtain the tensile stress was measured six times. Tab. 3.4 presents the average dimensions.

To measure this dimensions, a Digimatic caliper has been used. According to the instruction manual, the caliper external measurements have an uncertainty of $0.02[mm]$ if the dimensions are less than $200[mm]$. For six measurements it resulted in uncertainty of $0.0082[mm]$.

ID	w_0 $[mm]$	Thickness $t[mm]$	ID	w_0 $[mm]$	Thickness $t[mm]$
T12A00N1	12.70	1.13	T30A00N1	12.68	2.93
T12A00N2	12.68	1.12	T30A00N2	12.69	2.90
T12A00N3	12.70	1.12	T30A00N3	12.77	2.90
T12A00N4	12.72	1.11	T30A00N4	12.75	2.89
T12A45N1	12.65	1.09	T30A00N5	12.66	2.88
T12A45N2	12.67	1.11	T30A00N6	12.71	2.90
T12A45N3	12.67	1.10	T30A45N1	12.72	2.88
T12A45N4	12.67	1.11	T30A45N2	12.75	2.89
T12A90N1	12.76	1.15	T30A45N3	12.74	2.89
T12A90N2	12.75	1.15	T30A45N4	12.77	2.90
T12A90N3	12.77	1.14	T30A45N5	12.82	2.91
T12A90N4	12.67	1.07	T30A45N6	12.78	2.88
T30A90N1	12.75	2.90	T30A90N4	12.75	2.88
T30A90N2	12.79	2.89	T30A90N5	12.77	2.86
T30A90N3	12.77	2.87	T30A90N6	12.72	2.85

Table 3.4: Dimensions of each of the tensile test specimens

To ensure proper adhesion of the white ink to the specimen's surface, acetone was used to clean the specimens. A white matte layer (RAL 9016) was then applied, followed by drying. The matte effect will be important as the light reflex could disturb the recording. Poncelet demonstrated that light reflexes can increase local displacement uncertainty by up to five times [61].

Subsequently, a matte black dotted pattern (RAL 9005) was applied to the surface through the utilization of a speckling technique. This speckle plays a pivotal role in the generation of a stochastic pattern, thereby enabling the correlation matrix to differentiate between each pattern.

During the tests it was verified that if the ink was applied and the test was not realized soon it could lead to cracks in the ink which could affect the end of the DIC technique.

3.1.3 Tensile Test with Digital Image Correlation

The main objective of this section is to perform a tensile test using a DIC technique. This will be needed for acquiring material properties for further stamping simulations.

As defined in ISO 6892-1, for each analysis at least three tests have to be made [59]. At total eighteen tensile tests needs to be performed.

To ensure the specimen's alignment, a stop was utilized to facilitate the alignment. Preliminary experimental tests indicated the necessity of employing extensometers to avert slippage and ensure precise deformation measurement.

The tests were conducted using a Canon EOS R10 camera and an INSTRON 4485 tensile testing machine. The machine was configured to operate in position control mode, and a $200[kN]$ load cell was used. The sampling rate was set to 4 data points per second.

After some experimental tests, it has been decided to realize the camera calibration.

Since the cameras could have some intrinsic errors and extrinsic errors a calibration pattern was used to calibrate and undistort the image using the OpenCV library from python. The calibration pattern is shown in Figure 3.10.

Twenty images were used from different angles to calibrate the camera. A further analysis about the camera calibration are exposed in the results.

Figure 3.10: A grid pattern with 24 by 23 squares. Each square is $5[mm] \times 5[mm]$ in size.

The camera was set to record at Full HD, 25 FPS, with a shutter speed of 1/30, an aperture angle of 1/16 and ISO 5000.

Hijazi reported that misalignment errors of one or two degree can result in a 5μ-strains[62] error. The camera is equipped with an electronic level to maintain proper alignment. Fig. 3.11 illustrates the electronic level. Two angular adjustments were made—pitch and roll—using the electronic level for precise alignment. The yaw was manually calibrated based on the boundaries of the test machine.

To adjust the electronic level, it's needed to align the redlines in Fig. 3.11 with the yellow squares.

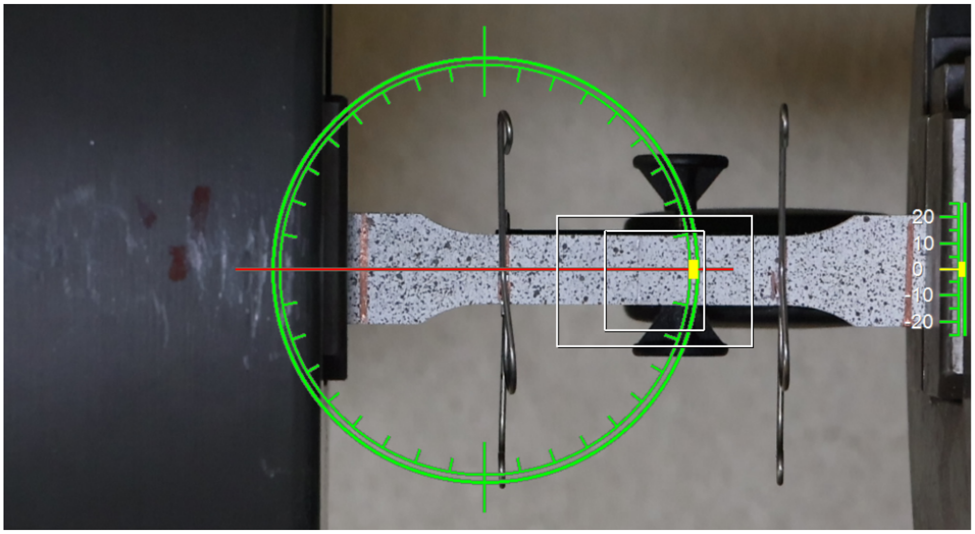

Figure 3.11: Electronic Level Adjustment

The advance velocity is setup to $2.54[mm \cdot min^{-1}]$ according to ISO 6892:1. After ensuring that the camera was level with the ground and orthogonal to the sample, the tests were performed.

The full setup is shown in Fig. 3.12, including a lighting system, a mount to rotate the camera 90º, two tripods, the camera itself, and the recording software.

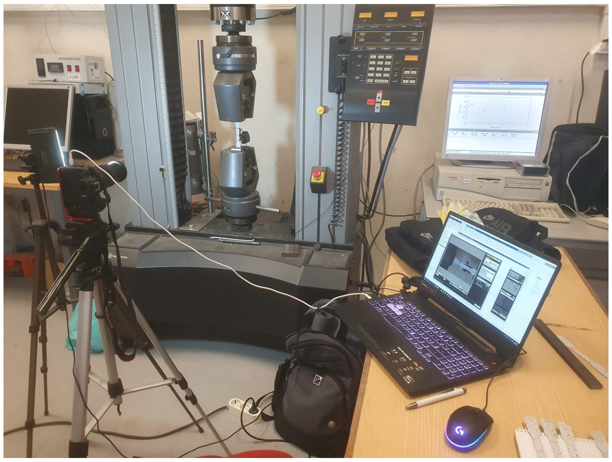

Figure 3.12: Full Experimental Recording Setup

3.1.4 Obtaining the tensile test related data

This subsection contains the all the post-processing method for the test data.

An algorithm was developed in *MatLab* to post-process tensile test data, which includes force and deformation measurements. From the initial values the maximum force is extracted. Then using the specimen dimensions, the algorithm calculates and plots the engineering stress and engineering strain. It should be noted that the dimensions of each specimen were presented in Tab. 3.4.

The elastic modulus was obtained directly from the literature. As the material obtained has no yield point elongation, by offsetting this linear equation by 0.2% strain and finding its intersection with the engineering stress-strain curve, the yield strength σ_y^{eng} and corresponding strain are determined. Fig. 3.13 illustrates an resume about how the algorithm works.

Afterward, the maximum deformation ε_{max}^{eng} and the tensile ultimate yield strength σ_{ut}^{eng} are obtained.

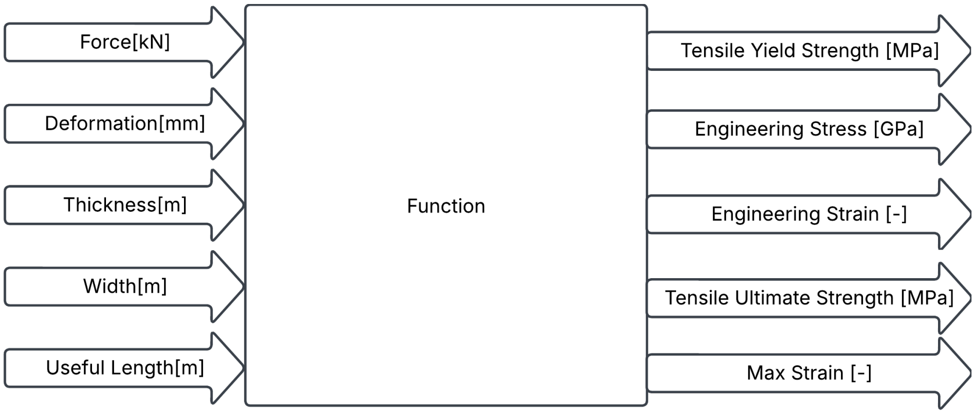

Figure 3.13: Input Variable and Output Variables

The true stress-strain curve was then calculated according to ISO 10275:2007. Note that by using the natural logarithm, it is still an approximation, but it's not significantly different from the real curve[63].

$$\sigma^{true} = \left(\frac{F}{w_o \cdot t_o}\right) \cdot \left[\frac{L_e + \Delta L}{L_e}\right] \tag{3.1}$$

$$\varepsilon^{true} = ln\left|\frac{L_e + \Delta L}{L_e} - \frac{F}{w_o \cdot t_o \cdot E}\right| \tag{3.2}$$

After that this values were converted to the logarithmic scale to perform a linear regression.

$$\begin{cases} x = ln|\varepsilon^{true}| \\ y = ln|\sigma^{true}| \end{cases} \tag{3.3}$$

Using the true yield strength, linear fitting was performed based on Eq. 3.4. In this fitting, the terms a and b correspond to the strain hardening exponent n and the logarithm of the strength coefficient $ln|K|$, respectively. As ISO 10275:2007 don't define an interval as long it's greater than 2%, the interval from 2% to the maximum force strain A_g was selected. Fig 3.14 resumes how does this function works.

$$f(x) = ax + b \tag{3.4}$$

To obtain the point where exists 2% and A_g of plastic deformation it's needed to intersect the curve with the elasticity modulus line offset by $0.02[adm]$ and $A_g[adm]$.

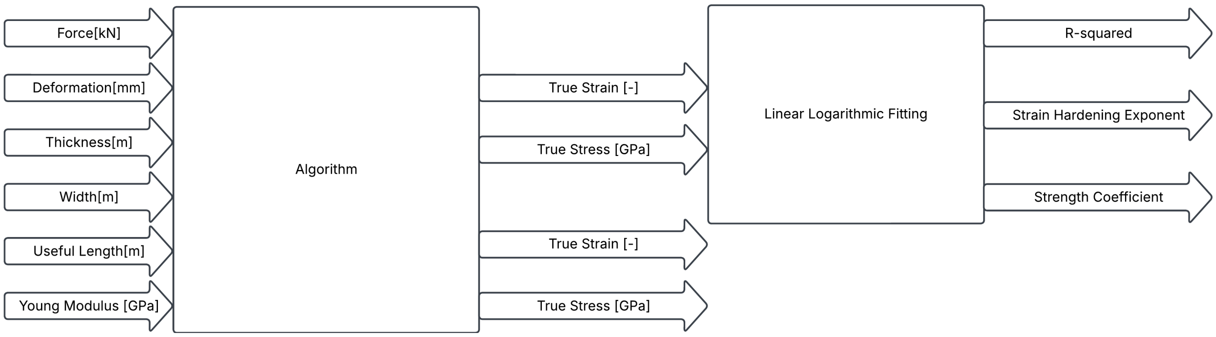

Figure 3.14: Input Variable and Output Variables

The postprocess DIC method was realized with a software program known as Zeiss Correlate. This software emerged following Zeiss's acquisition of GOM, a widely recognized software for such applications, while maintaining the same functionality[64].

ISO 11003:2020 standardises the method for determining the Lankford coefficient. To obtain the anisotropy ratio, it is required to calculate the ratio between true thickness plastic strain and true width plastic strain. The constant volume assumption is used to obtain true thickness strain data, as it is difficult to obtain accurate thickness measurements as proposed in Eq. 2.1.

In order to ascertain the number of frames per second (FPS) required for DIC processing, the crosshead speed was converted to millimeters per second. Subsequently, the region of interest, in other words, the distance between grips of the extensometer was measured in pixels, and the ratio of pixels per millimeter was calculated. Then, by multiplying the crosshead speed with the conversion ratio, the number of pixels per second was achieved. The adopted methodology is delineated in Eq. 3.5.

$$CrossheadSpeed\left[\frac{px}{s}\right] = CrossheadSpeed\left[\frac{mm}{s}\right] Ratio\left[\frac{px}{mm}\right] \tag{3.5}$$

The result of this equation refers to how fast pixels progress during the tensile test. Additionally, the minor camera resolution is one pixel in a photo, in other words the camera doesn't capture half of a pixel displacement.

By calculating the crosshead speed lead to a result of at least 0.5 FPS. However, Zeiss Correlate works with a subpixel resoultion[65]. Because of this situation, the number of FPS have been set to 1 FPS.

Then a Python algorithm using the OpenCV library have been created to change the FPS, to separate the video in a serie of images, to undistort, to cut and rotate these images. Given that the camera records at a rate of 25 FPS, the algorithm extracts a single frame at the interval of twenty-five frames.

By using Zeiss Correlate the region of interest has been set. Then the distance between the specimen borders have been set to correlate the number of milimeters per pixel. This distance was set as the measured useful length width.

After that, a total of eight digital extensometers have been evaluated. Three for the strains in $y - axis$ and five for the $x - axis$ strains. These $x - axis$ extensometers have been set to have the width of the specimen, while $y - axis$ $50[mm]$.

The methodology employed in the creation of the extensometers involved the determination of the body's center, followed by the summation or subtraction of a proportion of the total length. The method is elucidated in Tabs. 3.5.

	x	y
Top	-	$y_{center} + 48/2$
Middle Top	-	$y_{center} + 48/4$
Middle	x_{center}	y_{center}
Middle Bottom	-	$y_{center} - 48/4$
Bottom	-	$y_{center} - 48/2$

(a) $x - axis$ aligned extensometer

	x	y
Right	$x_{center} + w_0/2 - 1$	-
Middle	x_{center}	y_{center}
Left	$x_{center} - w_0/2 + 1$	-

(b) $y - axis$ aligned extensometer

Table 3.5: Extensometer Center Coordinates

The mean value between the extensometers was used. At times, specimen movement caused a loss of reference in the digital extensometers, and the missing values were filled in using linear interpolation.

Afterward, the length change data was extracted. It's important to remember that the data was collected directly as a true strain and exported as an .csv archive. So on, an additional MATLAB algorithm was developed to calculate the anisotropy ratio. The true plastic strains used to obtain the Lankford coefficient were determined using Eqs. 3.6 in accordance with ISO 10113:2020[43].

$$\begin{cases} \varepsilon^{true}_{plastic-length} = ln\left|\frac{L_e+\Delta L}{L_e} - \frac{F}{S_0 \cdot m_e}\right| \\ \varepsilon^{true}_{plastic-width} = ln\left|\frac{w_0+\Delta w}{w_0} + \frac{\nu F}{S_0 \cdot m_e}\right| \end{cases} \tag{3.6}$$

Note that the right term in these equations refers to the elastic deformation. It's obtained by dividing the stress by the elasticity modulus. In order to subtract this data, a synchronization between the two systems is needed.

Although the camera and the tensile test data are two asynchronous systems. To synchronize this data, it must first be verified if the vertical digital extensometer gives similar results to the measurements of the specimen after the testing.

Subsequently, to synchronize the systems the data values obtained by DIC were related by linear interpolation using the engineering strain stress curve. After synchronizing data between the camera and the tensile test, the elastic part was removed by calculating the elastic strain.

The standard stipulates that when employing the automatic method, the data must be collected at a plastic strain range of 8% to 12% during the uniform plastic strain range. After that the linear regression method needs to be applied[43].

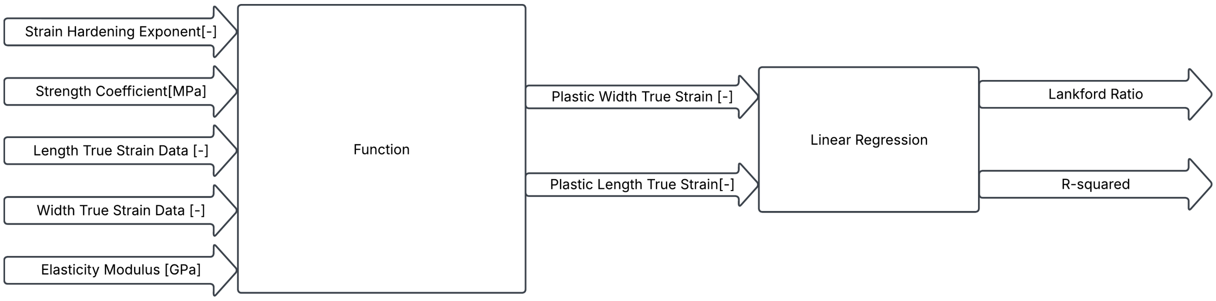

Figure 3.15: Input Variable and Output Variables

After applying the linear regression method, the slope m_r can be used to obtain the anisotropy ratio r according to Eq. 3.7.

$$r = \frac{-m_r}{1 + m_r} \tag{3.7}$$

3.1.5 Yield Criterion Modelling

To assure the representativeness of the mathematic model of the yield criterion, the experimental values will be evaluated in relation to the modelling. Then the difference between the experimental value and the theoretical value have been compared.

The system will be modeled according to Hill48 and Barlat89 yield criterions [45], [46]. And then, for comparison purposes the Von Mises plastic potential equation will be added to the graph.

The plastic potential proposed by Hill for a tridimensional state of stress is presented in Equation 3.8.

$$2f(\sigma) = F(\sigma_{yy}-\sigma_{zz})^2+G(\sigma_{zz}-\sigma_{xx})^2+H(\sigma_{xx}-\sigma_{yy})^2+2(L\sigma_{yz}^2+M\sigma_{zx}^2+N\sigma_{xy}^2) = 1 \tag{3.8}$$

These are the F, G, H, L, M, N Hill coefficients. These coefficients are responsible for widening or narrowing the ellipse and changing the shape according to the degree of anisotropy.

And the σ_{xx}, σ_{yy} and σ_{zz} the components along the x,y and z directions. Note that this components are different from the principal directions which remains in a plane defined by the Mohr's Circle. Look at Section A.1 for more details.

For a plane stress condition, some of this stresses are null $\sigma_{zz} = \sigma_{zx} = \sigma_{yz} = 0$ and results in a simplified equation. Eq. 3.9.

$$2f(\sigma) = (G+H)\sigma_{xx}^2 + (F+H)\sigma_{yy}^2 - 2H\sigma_{xx}\sigma_{yy} + 2N\sigma_{xy}^2 = 1 \tag{3.9}$$

The most common way to estimate this parameters is by using the anisotropy ratio R_0, R_{45} and R_{90} in the Eq. 3.10 [66].

$$\begin{cases} \dfrac{H}{G} = R_0 \\ \dfrac{F}{G} = \dfrac{R_0}{R_{90}} \\ \dfrac{N}{G} = \left(R_{45} + \dfrac{1}{2}\right)\left(\dfrac{R_0}{R_{90}} + 1\right) \end{cases} \tag{3.10}$$

These parameters can also be estimated by using the initial tensile yield stress according to Eq. 3.11 or Eq. 3.12. Note that there's a difference between tensile yield stress and initial tensile yield stress because of the hardening effects.

$$\begin{cases} H = \dfrac{R_0}{(1+R_0)\sigma_0^2} \\ G = \dfrac{H}{R_0} \\ F = \dfrac{1}{\sigma_{90}^2} - H \\ N = \dfrac{2}{\sigma_{45}} - \dfrac{(G+F)}{2} \end{cases} \tag{3.11}$$

or

$$\begin{cases} H = \dfrac{R_{90}}{(1+R_{90})\sigma_{90}^2} \\ G = \dfrac{H}{R_{90}} \\ F = \dfrac{1}{\sigma_0^2} - H \\ N = \dfrac{2}{\sigma_{45}} - \dfrac{(G+F)}{2} \end{cases} \tag{3.12}$$

It's important to emphasize that the Eq. 3.12 will appear rotated in the tensile yield stress graph because the coefficients are being obtained from properties from the TD.

If the state of stress is a uniaxial tensile test the components σ_{xx}, σ_{xy} and σ_{yy} can be rewrited as σ tensions multiplied by a rotation matrix with the angle θ with the RD.

$$\begin{cases} \sigma_{xx} = \sigma cos^2(\theta) \\ \sigma_{xy} = \sigma cos(\theta) sin(\theta) \\ \sigma_{yy} = \sigma sin^2(\theta) \end{cases} \tag{3.13}$$

And this components in different plane from the principal directions implemented in the contour. This process results in the contour for the specific case of the uniaxial testing. This leads to a contour to compare with the experimental results.

Then the *MatLab* will be utilized to numerically obtain the points. As there is two variables, θ will be taken as a known value varying from $0[rad]$ to $2\pi[rad]$ and the roots from σ be obtained from the *root* command.

The *root* command finds the real and imaginary roots of a certain problem by isolating their coefficients a_1, a_2, ..., a_{n+1} which accompanies the variable x. Eq. 3.14 shows an example.

$$a_1x^n + a_2x^{n-1} + ... + a_nx^1 + a_{n+1}x^0 \rightarrow [a_1\ a_2\ ...\ a_n\ a_{n+1}] \tag{3.14}$$

For the case of the Hill48 the isolated coefficients are shown in Eq. 3.15. The $\overline{\sigma}$ is initial yield aligned with RD.

$$\Big[(G+H)cos^4\theta + (F+H)sin^4\theta + (N-H)2cos^2\theta sin^2\theta, 0, -1\Big] \tag{3.15}$$

From this, a vector which relates the angle with the RD and the $\sigma_y(\theta)$ have been extracted. Also, Hill proposes an equation for visualizing the Lankford Coefficient with θ with RD shown in Eq. 3.16.

$$r_\theta = \frac{(2N-G-F)sin^2\theta cos^2\theta + Hcos^2 2\theta}{Fsin^2\theta + Gcos^2\theta} \tag{3.16}$$

The Barlat89 is essentially a plastic potential yield criterion for a plane stress and don't need to be simplified with the plane stress condition as Hill48. The equation which delimits this contour is illustrated in Eq. 3.17.

$$f(\sigma) = a\left|K_1 + K_2\right|^M + a\left|K_1 - K_2\right|^M + c\left|2K_2\right|^M = 2\overline{\sigma}^M \tag{3.17}$$

Where a, c, h, p and M are constants and the variables K_1 and K_2 are stress invariants shown in Eq. 3.18. Note that K_1 and K_2 are equal to the principal stresses σ_1 and σ_2 when applying the Mohr's Circle.

$$\begin{cases} K_1 = \frac{\sigma_{xx} + h\sigma_{yy}}{2} \\ K_2 = \sqrt{\left(\dfrac{\sigma_{xx} - h\sigma_{yy}}{2}\right)^2 + p\sigma_{xy}^2} \end{cases} \tag{3.18}$$

Barlat proposed a method for determining the a, c and h parameters from the anisotropy ratio, the equations needed are shown in Eq. 3.19[46]. While the M is a coefficient related to the cristalline arrangement of the material which for the ferritic structure is adopted

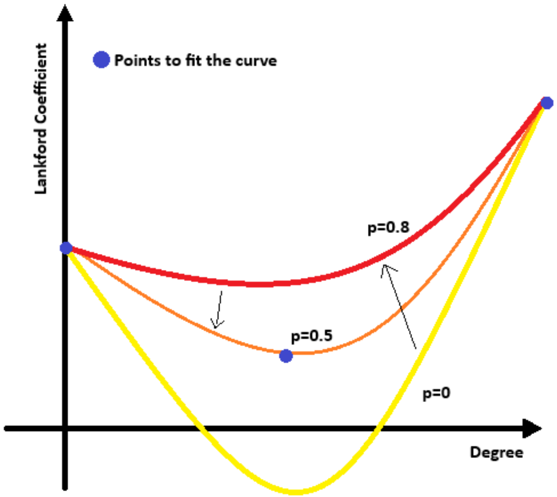

Figure 3.16: Iterative process to fit p

as six.

The p coefficient have been calculated by trial-and-error curve adjustment of the Lankford Coefficient because the p coefficient cannot be calculated analitically[46]. Fig. 3.16 shows how the p affects the curve.

$$\begin{cases} a = 2 - 2\sqrt{\dfrac{R_0}{1+R_0}\dfrac{R_{90}}{1+R_{90}}} \\ c = 2 - a \\ h = \sqrt{\dfrac{R_0}{(1+R_0}\dfrac{1+R_{90}}{R_{90}}} \end{cases} \tag{3.19}$$

The same procedure have been made with the θ taken as a known value varying from $0[rad]$ to $2\pi[rad]$ to obtain the roots.

Subsequently, the stress along the angle with RD can be plotted for each of the yield criteria. This approach facilitates enhanced visualization of the discrepancies between the physical problem and its mathematical representation.

Barlat also proposes an equation for visualizing the anisotropy ratio according to the angle with the RD[46].

$$R_\theta = \frac{2M\overline{\sigma}^M}{\left(\frac{\partial f}{\partial \sigma_{xx}} + \frac{\partial f}{\partial \sigma_{yy}}\right)\sigma} \tag{3.20}$$

Where

$$\begin{split}\frac{\partial f}{\partial \sigma_{xx}} = M \Bigg\{ a(K_1 - K_2)|K_1 - K_2|^{M-2}\left(\frac{1}{2} - \frac{\sigma_{xx} - h\sigma_{yy}}{4K_2}\right) \\ + a(K_1 + K_2)|K_1 + K_2|^{M-2}\left(\frac{1}{2} + \frac{\sigma_{xx} - h\sigma_{yy}}{4K_2}\right) \\ +2^M c K_2^{M-1}\frac{\sigma_{xx} - h\sigma_{yy}}{4K_2}\Bigg\}\end{split} \tag{3.21}$$

$$\begin{split}\frac{\partial f}{\partial \sigma_{yy}} = M \Bigg\{ a(K_1 - K_2)|K_1 - K_2|^{M-2}\left(\frac{h}{2} - h\frac{\sigma_{xx} - h\sigma_{yy}}{4K_2}\right) \\ + a(K_1 + K_2)|K_1 + K_2|^{M-2}\left(\frac{h}{2} + h\frac{\sigma_{xx} - h\sigma_{yy}}{4K_2}\right) \\ -2^M c K_2^{M-1}\frac{\sigma_{xx} - h\sigma_{yy}}{4K_2}\Bigg\}\end{split} \tag{3.22}$$

3.1.6 Blank Direction Optimization

This subsection contains an approach which considers some critical zones in the stamping process and by rotating the blank sheet, the mechanical properties along that direction can be maximized.

Given the following considerations, this problem can be defined.

- Lankford Coefficient refers to the capacity of the material to deform more in width than thickness. Consequently, it represents a resistance to necking.

- The Lankford Coefficient in function of the angle with RD have been modelled in the past section.

- The final geometry of the piece.

As the first statement is just an affirmation, and the second is already modelled, it just leaves the last statement to be defined. The geometry of the piece and where are the critical zones.

To do this the critical zones will be rewritten in a function of the angle with a fixed reference frame.

Fig. 3.17 shows a cone. A piece which makes part of the exhaust system. This cone is radially symmetrical in exception of three wedges which are not equispaced.

There are two wedges which their centers are spaced by $90[degrees]$. Their angular spacing coincides with the material properties regularly repeated pattern. Because of that the reference stationary frame was defined exactly in the middle of these two adjacent wedges.

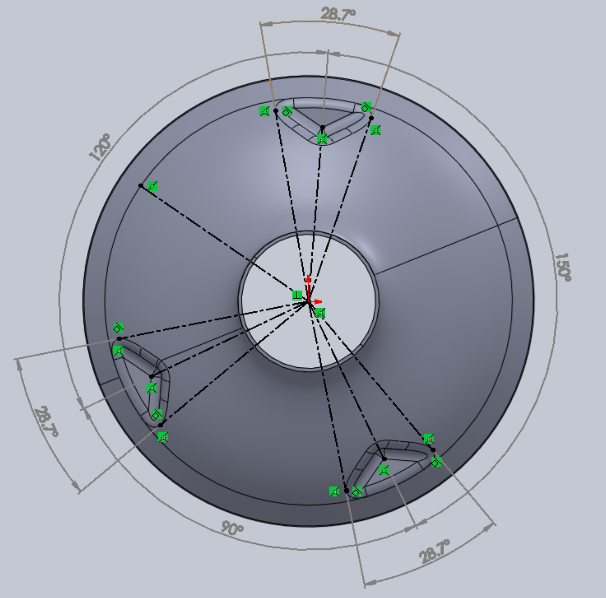

Figure 3.17: Critical Zone Analysis

This analysis leads to three critical intervals I_1, I_2 and I_3 rewritten in function of the angle in Eq. 3.23.

$$\begin{cases} I_1, & \theta + 45[^\circ] - 14.35[^\circ] \leq I_1 \leq \theta + 45[^\circ] + 14.35[^\circ] \\ I_2, & \theta - 45[^\circ] - 14.35[^\circ] \leq I_2 \leq \theta - 45[^\circ] + 14.35[^\circ] \\ I_3, & \theta - 165[^\circ] - 14.35[^\circ] \leq I_3 \leq \theta - 165[^\circ] + 14.35[^\circ] \end{cases} \tag{3.23}$$

By defining an objective function with represents the problem of maximizing the $R(\theta)$ the angle which maximizes the Lankford Ratio was obtained. Eq. 3.24 shows the optimization problem.

$$\begin{gathered} max\ f(\theta) = \sum_{I=0}^{28.7} [R(I_1) + R(I_2) + R(I_3)] \\ \text{where } -90 \leq \theta \leq 90 \end{gathered} \tag{3.24}$$

3.1.7 Forming Limit Curve

The forming limit curve determines the combination of the major and minor deformation which leads to a fracture.

Since Nakajima test or others experimental tests demands a high amount of material and time, the forming limit curve will be predicted, then compared to the literature. There are several well employed methods to predict FLD such as Keeler, NADDRG and Abspoel.

The Keeler method depends only on the thickness and work hardening exponent n. On the other hand, Abspoel predicted FLD uses Lankford coefficient, maximum strain and has a thickness dependency as their input variables.

Keeler and Brazier(1977) model

The Keeler and Brazier FLC prediction method uses as input the thickness t and the power-hardening law coefficient n.

The intercept with the major strain axis can be calculated by Eq. 3.25. This value defines the localized neck starting point while subject to a plane strain condition.

$$FLC_0 = ln\left[1 + \left(\frac{23.3 + 14.13t}{100}\right)\frac{n}{0.21}\right] \tag{3.25}$$

The left side of the FLC is calculated by creating a straight line with a -1 slope which intercepts the major strain axis in the FLC_0-value. Eq. 3.26 delineates the condition that defines the onset of localized necking under uniaxial tension.

$$\varepsilon_1 = FLC_0 - \varepsilon_2 \tag{3.26}$$

The right-hand side can be obtained from Equation 3.27; in other words, it represents the biaxial stretching limit.

$$\varepsilon_1 = (1 + FLC_0)(1 + \varepsilon_2)^{0.5} - 1 \tag{3.27}$$

Abspoel et. al model

The Abspoel method depends on the $r-$value, maximum strain A_{80} and a thickness dependency t. It's subdivided into five points, the biaxial stretching point, an intermediate biaxial stretching point, the plane strain and the uniaxial tensile point.

The point corresponding to localized necking under uniaxial tensile conditions is obtained from Equation 3.28. Since the FLD is plotted as major strain versus minor strain, ε_1 represents the major strain, while ε_2 corresponds to the minor strain.

$$\begin{cases} \varepsilon_2^{TE} = -\frac{(0.0626 \cdot A_{80}^{0.567} + (t-1) \cdot (0.12 - 0.0024 A_{80})) \cdot 0.797 \cdot r^{0.701}}{\sqrt{(1 + (0.797 \cdot r^{0.701})^2}} \\ \varepsilon_1^{TE} = (1 + 0.797 \cdot r^{0.701}) \frac{(0.0626 \cdot A_{80}^{0.567} + (t-1) \cdot (0.12 - 0.0024 A_{80}))}{\sqrt{(1 + (0.797 \cdot r^{0.701})^2}} \end{cases} \tag{3.28}$$

The plane strain localized necking limit is calculated by Eq. 3.29.

$$\varepsilon_2^{TE} = 0.0084 \cdot A_{80} + 0.0017 \cdot A_{80} \cdot (t - 1) \tag{3.29}$$

The intermediate biaxial point (Eq. 3.31) and the biaxial point (Eq. 3.32) have a thickness dependency. Eq. 3.30 shows transition thickness t_{trans}.

$$t_{trans} = \frac{1.5 - 0.00215 \cdot A_{80}^{MIN}}{0.6 + 0.00285 \cdot A_{80}^{MIN}} \tag{3.30}$$

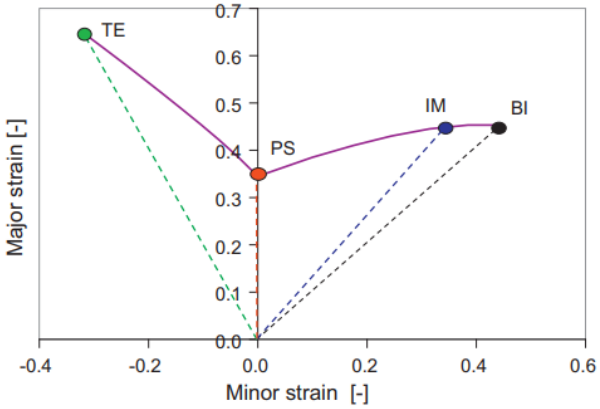

Figure 3.18: Calculated Points
Source:[53]

Consequently, if the $t \geq t_{trans}$, the t_{trans} will be used instead of t.

$$\begin{cases} \varepsilon_1^{IM} = 0.0062 \cdot A_{80} + 0.18 + 0.0027 \cdot A_{80} \cdot (t-1) \\ \varepsilon_2^{IM} = 0.75 \varepsilon_1^{IM} \end{cases} \tag{3.31}$$

$$\begin{cases} \varepsilon_1^{BI} = 0.00215 \cdot A_{80}^{MIN} + 0.25 + 0.00285 \cdot A_{80}^{MIN} \cdot t \\ \varepsilon_2^{BI} = \varepsilon_1^{BI} \end{cases} \tag{3.32}$$

For better understanding the Fig. 3.18 shows the points calculated before.

3.2 Sequential Stamping and Finite Element Method

The software adopted for this thesis is Ansys Forming, an application within the Ansys suite that utilizes the LS-DYNA solver.

Two components will be simulated in this work: the 429x and the 143x. These are made of FSS—EN 1.4512 and EN 1.4509, respectively.

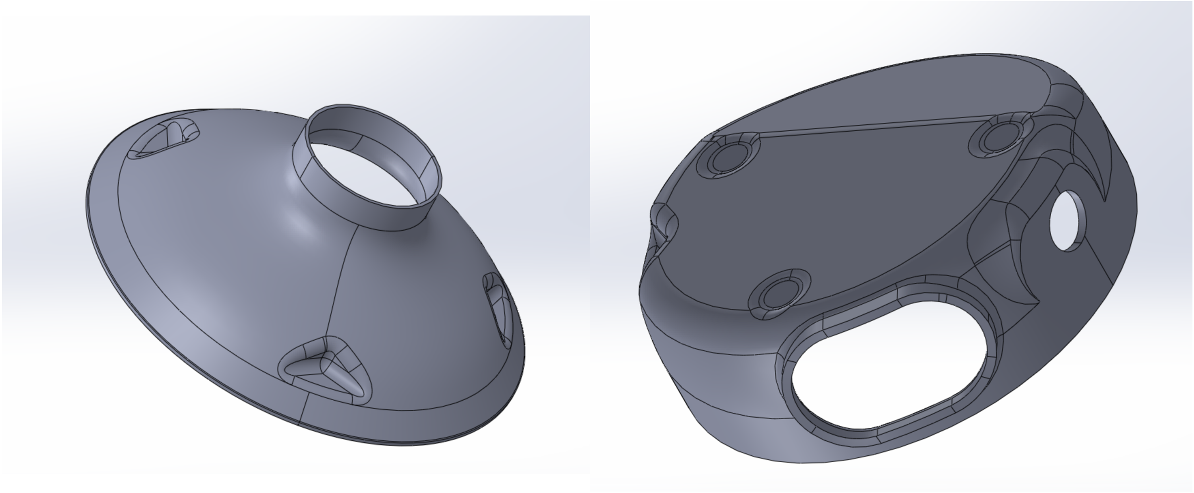

(a) Piece 429x

(b) Piece 143x

Figure 3.19: Isometric View of each of the stamping parts

3.2.1 Part 429x

The manufacturing process of component 429x is comprised of seven distinct operations. Each of these operations is designated by the letter "OP" followed by a number, such as "OP1," "OP2," and so on. The initial operation is the operation that forms the blank. However, the blank was delivered after OP1, thereby precluding consideration of the initial operation.

As a sequential stamping process, three preliminary draw operations will be executed, encompassing the OP2, OP3, and OP4 stages. Subsequently, the process of forming the stamping collar will be initiated. The initial step involves trimming, which results in the formation of a hole designated as OP5. Subsequently, the flanging operation is initiated, wherein a punch with a diameter that exceeds the hole's diameter is inserted, thereby forming the collar (OP6 and OP7). The dies and punches are presented in Fig. 3.20.

It's important to remember that the failures occurs during the final stage, specifically the formation of the collar, as illustrated in Fig. 3.21.

The first part of the finite element method involves characterizing the material. The blank sheet dimension was set according to Tab. 3.1 which in this case has a 1.2$[mm]$

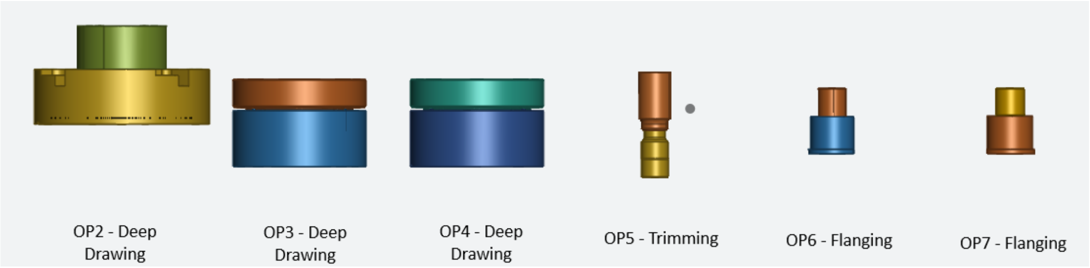

Figure 3.20: Sequential Stamping Method

Figure 3.21: Crack in the collar
Source: Catraport

thickness and 200$[mm]$ diameter and the lubrication coefficient is set to $\mu_c = 0.11$ [67]. The mesh size of the blank was set to 2.5$[mm]$ with the mesh adaptation option turned on allowing one iteration.

EN 10088-1 proposes that the elasticity modulus E should be 220$[GPa]$, although some authors proposes the use of a different value of 200$[GPa]$ for FSS [12], [13]. The elasticity modulus has been set as 200$[GPa]$. The n coefficient from Swift power hardening law and the initial yield stress has been set according to Tab. 4.1 according to the RD.

The FLD has been calculated from Abspoel method and inputed into the software.

After defining the material properties, the next step consists in defining the stamping processes, OP2 is divided into two phases/stages the closing and the drawing.

In the first stage(closing), the binder lowers until it presses the blank counter the die, then in the second stage(drawing) it remains stationary offering some resistance to movement to the blank.

Differently, the punch remains stationary at the first stage, then it travels down until an specified position. The die remains fixed into the bed during the whole process. Tab. 3.6 shows the methodology applied to the OP2.

	Closing	Drawing
Punch	Stationary	Travel to position zero
Binder	Closing to the Die	Stationary
Die	Fixed	Fixed

Table 3.6: Stamping Process Methodology

In later operations, as binders were not employed, the stamping process reduces to a single phase (drawing). Tab. 3.7 shows the methodology.

	Drawing
Punch	Travel to position zero
Die	Fixed

Table 3.7: Stamping Process Methodology

As the tools don't have the blank offset an offset of $1.1 \times \textit{blank thickness}$ has been applied to the dies with exception to the OP6 and OP7 dies which the offset has been taken as $1.583[mm]$ thick due to an error in the CAD model. The upper tools are left unmodified. During the trimming process OP5, a simplification has been made by only assuming a cutting tool with the same radius as the CAD.

This offset greater than the real geometry is important to let the material flow to the center during the drawing phases.

Tab. 3.8 shows the tools employed in each operation. Note that only the first considers a binder/blankholder. Consequently, the closing phase is not taken into consideration in later operations

Note that the OP5 doesn't employs any tools as the software provides a different methodology while operating trimming operations.

Then the simulation general parameters was set as accurate and was run.

	OP2	OP3	OP4	OP5	OP6	OP7
Punch	X	X	X	-	X	X
Binder	X	-	-	-	-	-
Die	X	X	X	-	X	X

Table 3.8: Tools employed in each operation

3.2.2 Part 143x

The same methodology has been employed in the part 143x. This mechanical part sequential stamping process encompasses five operations at total.

The main difference between this simulation and the previous one lies in the mesh size. Due to the more severe fractures observed in this part, higher stress concentrations were expected, necessitating a finer mesh refinement to accurately capture the localized deformation and failure behavior.

In this simulation the mesh size was set to $1[mm]$ and the mesh adaptive was set to two iterations.

The initial operation is blanking (OP10), yet as previously mentioned, the material has already been received in the form of a blank. The sequence of operations begins with a drawing operation (OP20), followed by a trimming operation (OP30) that initiates collar formation. Subsequently, the flanging operation (OP40) is performed, and the final operation is another trimming(OP50).

Although, in this piece just the first operation(OP20) will be analyzed.

This drawing operation follows the same methodology as shown in Tab. 3.6.

Fig. 3.22 shows the common failures during the production of the part 143x. Initially the images (a), (b) and (d) can be associated with a stress-induced defects(SID) while the (c) associated with a material-related defect(MRD).

It can be observed in (c) the phenomenon of ridging accompained by a crack, probably this fracture happened because of excessive uniaxial elongation.

(a) Failure during OP1

(b) Failure during Collar Formation

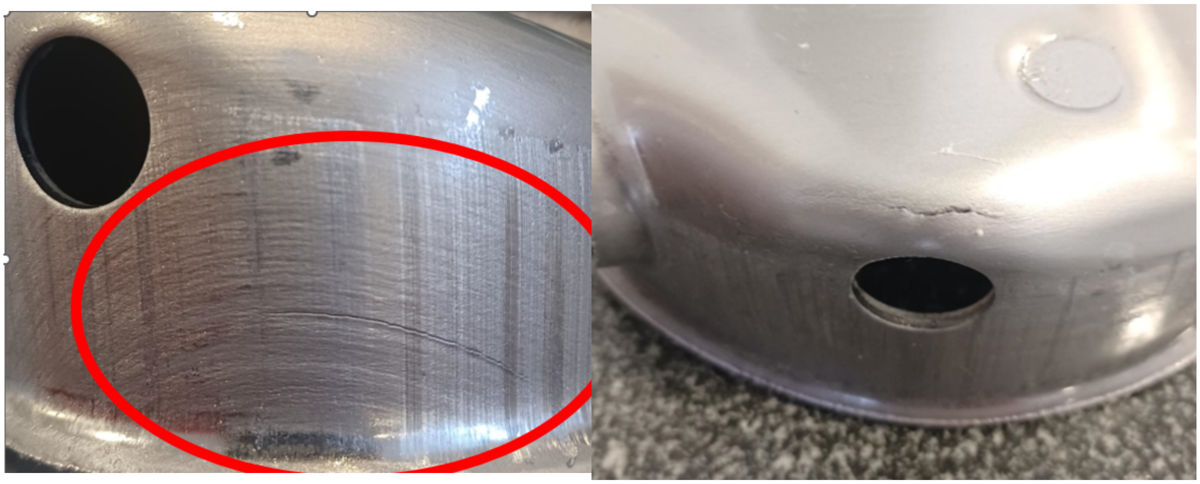

(c) Ridging and a Crack

(d) Crack next to the hole

Figure 3.22: Defects in the Piece 143x

Source: Catraport

Chapter 4

Results and Discussion

Chapter 4 presents the results obtained throughout this study and a brief discussion about each result. First, the results related to the tensile tests are presented. Then, the DIC results, including the $r-$values, are discussed. Next, a comparison between the different yield criteria is carried out. Following that, the predicted FLCs, obtained using the two different methods, are evaluated and compared. Finally, after the material properties have been fully characterized, the FEM simulation results are presented.

As illustrated in Fig. 4.1, the tensile test specimens exhibited a phenomenon of ridging or roping, a material related defect[31] characterized by the formation of ridges or protrusions on the surface of the material. It is evident that this phenomenon is more pronounced in the specimen aligned with RD. This phenomenon occurs in rolled FSS, although it has also been reported in aluminum sheets and copper alloys[68].

4.1 Tensile Test

Three tests were conducted for each direction, as previously defined.

From the engineering strain stress curve the main results obtained are the tensile yield strength σ_y, the tensile ultimate strength S_{ut} and the maximum strain ε_{max}.

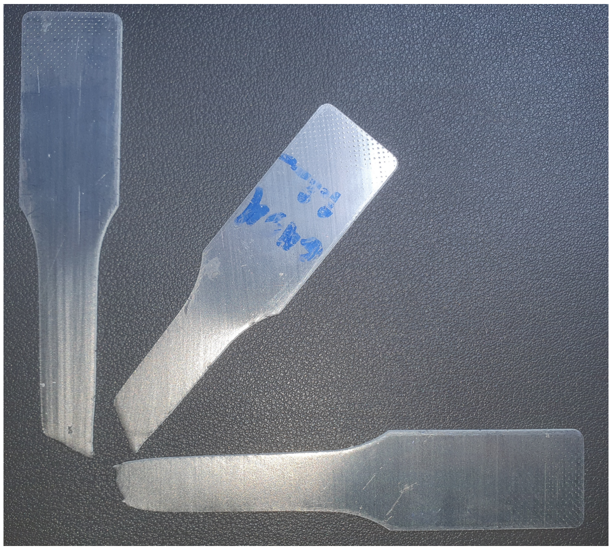

Figure 4.1: Ridging

Material	Direction	$S_{ut}[MPa]$	A_{max}[adm]	$\sigma_y[MPa]$
1.4512	RD	399.27 ± 3.48	0.33 ± 0.01	291.63 ± 4.50
1.4512	DD	394.85 ± 18.35	0.28 ± 0.01	301.8 ± 17.68
1.4512	TD	398.17 ± 8.15	0.31 ± 0.01	310.40 ± 6.25
1.4509	RD	462.33 ± 6.37	0.33 ± 0.01	354.48 ± 8.89
1.4509	DD	471.25 ± 22.36	0.33 ± 0.01	382.48 ± 18.26
1.4509	TD	480.86 ± 6.82	0.31 ± 0.01	382.90 ± 5.27

Table 4.1: Tensile test results

In both materials, the initial tensile yield strength tends to increase as the angle with the RD increases, whereas the maximum elongation (A_{max}) generally decreases with increasing angle to the RD.

A higher mean deviation is also observed in specimens tested along the DD, indicating greater mechanical instability in this orientation.

Additionally, the EN 1.4512 blank exhibits nearly constant ultimate tensile strength across all directions, indicating nearly isotropic behavior in this regard. In contrast, the 1.4509 material shows an increasing trend in ultimate strength with increasing angle to the RD, reflecting anisotropic characteristics.

Compared with the inspection certificates, all measured values are consistent with those provided by the supplier. Additionally, EN 1.4512 shows slightly lower values in the ultimate tensile strength (S_{ut}) than those obtained experimentally, but they remain within the acceptable tolerance range.

The parameters n and K of the power-law hardening model were determined via linear regression from the true-stress true-strain curve and the mean values and the standard deviation exhibited in Tab. 4.2.

Material	Direction	$K[MPa]$	$n_{2-A_g}[adm]$	$R-square$
1.4512	RD	621.67 ± 6.07	0.1584 ± 0.0013	0.9976 ± 0.0003
1.4512	DD	599.83 ± 23.20	0.1434 ± 0.0034	0.9990 ± 0.0004
1.4512	TD	594.85 ± 12.20	0.1359 ± 0.0013	0.9976 ± 0.0005
1.4509	RD	695.60 ± 7.84	0.1383 ± 0.0024	0.9987 ± 0.0004
1.4509	DD	690.84 ± 32.19	0.1260 ± 0.0020	0.9976 ± 0.0004
1.4509	TD	708.70 ± 9.92	0.1271 ± 0.0001	0.9992 ± 0.0002

Table 4.2: Experimental K and n

It can be observed that the n coefficient have a tendency to reduce as the angle with the RD rises. Additionally, the high R-square values indicates that the coefficients K and n can represent accurately the results.

4.1.1 Camera Calibration and Digital Image Correlation

This section aims to assess the necessity of camera calibration in the image processing pipeline. To achieve this, a fully random grayscale image was generated using Python. The camera calibration procedure was then applied to this image, resulting in an undistorted version of the speckle pattern.

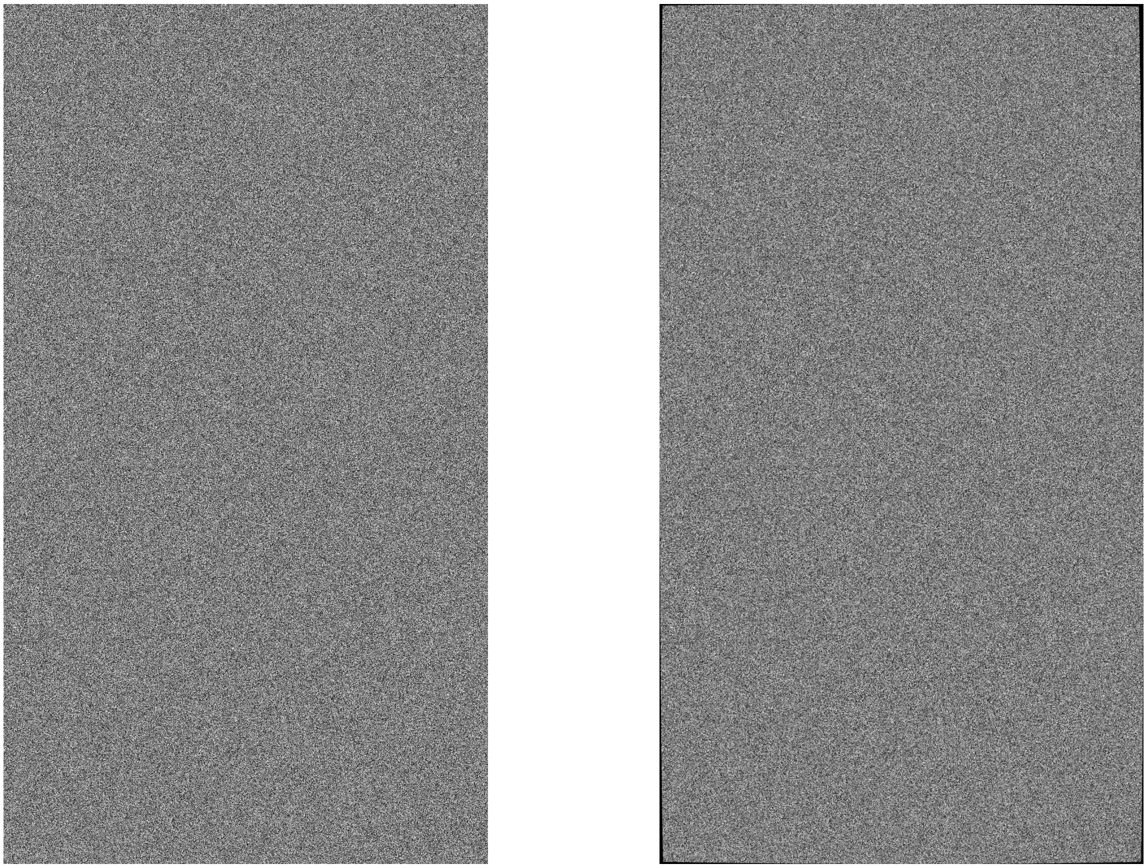

(a) Random Speckle - Original

(b) Undistorted Random Speckle

Figure 4.2: Comparison between distorted and undistorted

As shown in Fig. 4.2, a barrel distortion is visible in the original image. This is evident from the appearance of black borders at the corners of the undistorted image, indicating the correction of the distortion.

Fig. 4.3 presents the results of applying the DIC (Digital Image Correlation) technique between the original and undistorted images. This technique analyzes pixel displacement between the two images to quantify the geometric distortion.

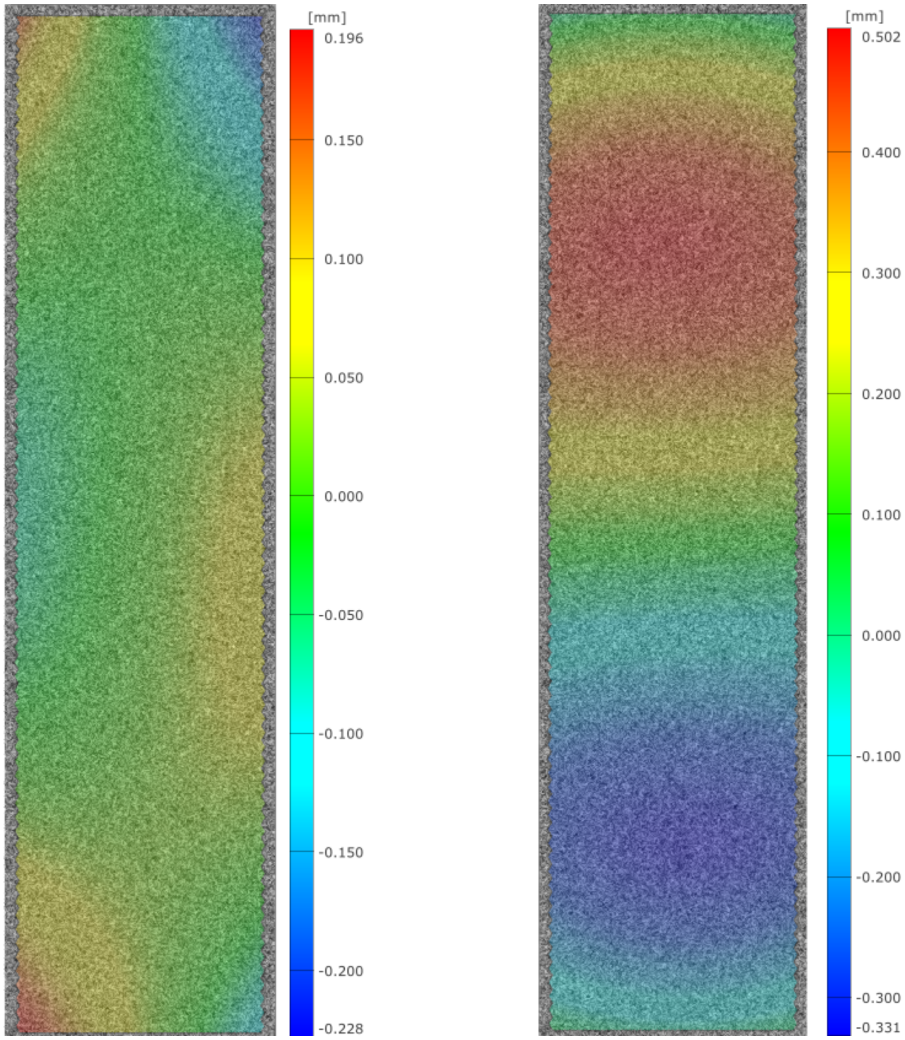

(a) X distortion (b) Y distortion

Figure 4.3: Comparison between distorted and undistorted

The red zones indicates that the point moved right or up and the blue zones indicates that the point moved right or down. Notably, the distortion in the Y-direction is significantly greater than that in the X-direction, which emphasizes the non-uniformity of the lens distortion.

To further illustrate the impact of camera calibration, Fig. 4.4 presents the X and Y digital extensometer positions as identified in both the initial(circle marker) and final frames(x marker).

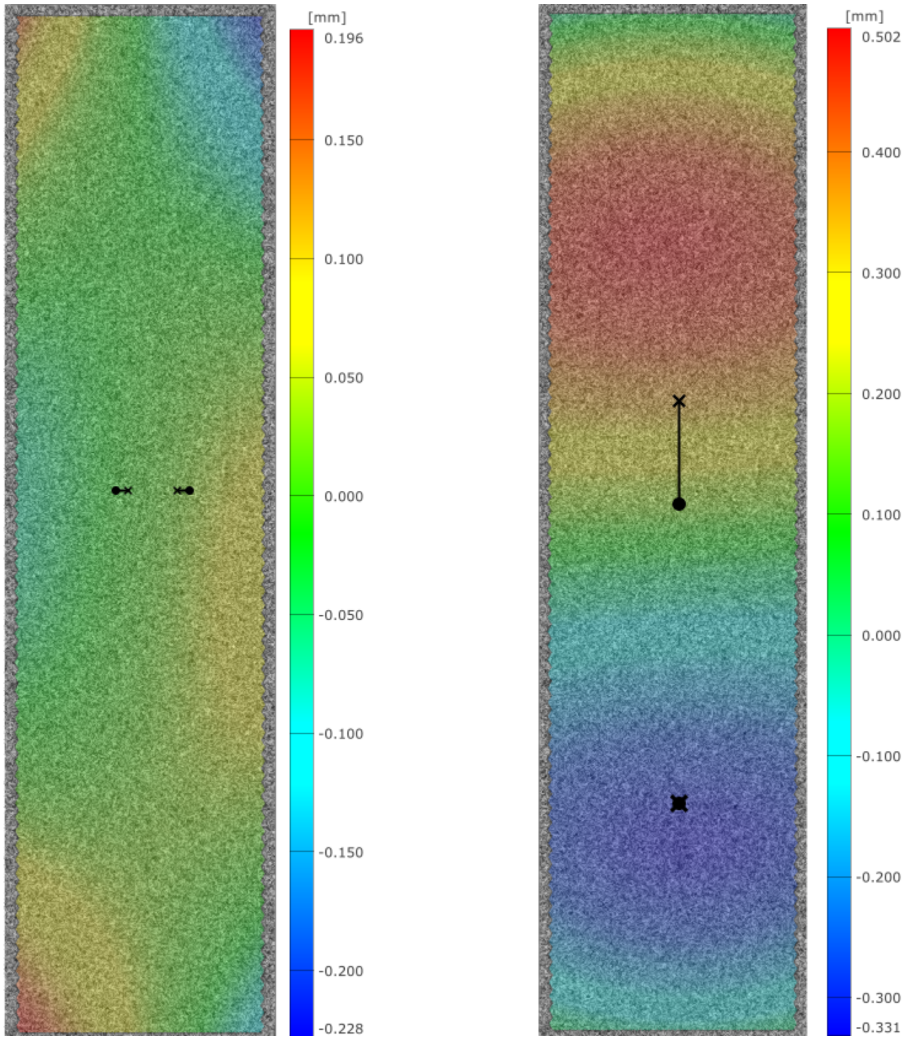

(a) X extensometer position change

(b) Y extensometer position change

Figure 4.4: Extensometer position change between initial and final frames

In the X-direction, both left and right points of the extensometer tend to move inward toward the center during the tensile test. In contrast, the Y-direction shows an upward movement of the upper point, while the lower point remains mostly stationary.

As observed in Fig. 4.4, the displacement in the X-direction is minimal. However, when evaluating the effect of camera calibration in the Y-direction, a difference of approximately 0.3 mm is evident in the heatmap between the upper point initial and final positions. This suggests that, in this setup, neglecting camera calibration could introduce an error of up to 0.3 mm in the measurement.

After using the Zeiss Correlate software, results directly obtained from the DIC and from measurements have been compared.

The r-value according to the RD have been calculated for each of the three specimens according to Eq. 3.7 and the standard deviation obtained.

Material	$t[mm]$	$r_0[adm]$	$r_{45}[adm]$	$r_{90}[adm]$
1.4512	1.2	1.2295 ± 0.0641	1.0725 ± 0.0707	1.5722 ± 0.1491
1.4509	3.0	0.7690 ± 0.08772	0.6846 ± 0.05624	1.3276 ± 0.1021

Table 4.3: Experimental Lankford Coefficients

It can be verified in Tab. 4.3 that both materials exhibit a U-shaped trend in their Lankford coefficients. The r-value initially decreases from the RD (r_0) to the DD (r_{45}), reaching its minimum at r_{45}, and subsequently increases toward the TD (r_{90}), where the highest anisotropy is observed.

Comparable values were gathered from literature and presented in Tab. 4.4 and 4.5.

Material	$t[mm]$	$r_0[adm]$	$r_{45}[adm]$	$r_{90}[adm]$
AISI 441[69]	0.84	1.078	1.019	1.417
AISI 441[60]	2.00	1.330	0.980	1.790
EN 1.4509[37]	3.00	0.670	0.850	1.390

Table 4.4: EN 1.4509 - Literature Values

Material	$t[mm]$	$r_0[adm]$	$r_{45}[adm]$	$r_{90}[adm]$
AISI 409[21]	1.00	1.715	1.521	2.620
AISI 409[70]	1.00	0.767	0.835	1.194
EN 1.4512[37]	1.20	1.210	0.840	1.710

Table 4.5: EN 1.4512 - Literature Values

The literature values values obtained from Tab. 4.4 and Tab. 4.5 were verified. Then, it can be concluded that the the obtained values were consistent with the expected outcomes.

The anisotropy is highly dependent on the hot/cold work strain history as demonstrated by Maruma[29].

Tab. 4.6 shows the calculated values of the planar anisotropy (Δr) and the average plastic strain ratio ($\overline{r}$) for each material.

Material	Δr	$\overline{r}$
EN 1.4512	0.3284	1.2367
EN 1.4509	0.3637	0.8664

Table 4.6: Experimental average plastic strain ratio and planar anisotropy

It can be observed that the planar anisotropy values (Δr) are low for both materials, suggesting a low tendency for earing during deep drawing. In contrast, the average plastic strain ratio ($\overline{r}$) shows distinct differences. EN 1.4512 exhibits a high $\overline{r}$, indicating good deep drawability due to its higher resistance to thinning. Conversely, EN 1.4509 has a much lower $\overline{r}$, reflecting limited drawability, as the material is more prone to thinning under tensile stress during forming.

4.2 Yield Criterion Modelling

4.2.1 EN 1.4512 - Yield Criterion

The anisotropy coefficients F, G, H and N from Hill48 were calculated using Eqs. 3.10, 3.11 and 3.12 . The Barlat89 coefficients a, c and h were determined from Eq. 3.19, while the coefficient p was obtained through curve fitting. All these coefficients are presented in Tab. 4.7.

Method	F	G	H	N
Hill48-FromStress0	0.3432	0.4605	0.5395	1.5308
Hill48-FromStress90	0.3312	0.4485	0.5515	1.5427
Hill48-FromAnisotropy	0.3508	0.4485	0.5515	1.2569

Method	a	c	h	p
Barlat89-FromAnisotropy	0.8388	1.1612	0.9499	0.9146

Table 4.7: EN 1.4509 - Anisotropy Coefficients

Since the Hill48 coefficients must be $F = G = H = 0.5$ and $N = 1.5$ for the isotropic case, the obtained parameters indicate a significant deviation from isotropy, particularly in F. Similarly, for the isotropic case in the Barlat89 model, the parameters must be $a = c = h = 1$ and $p = 2$, indicating a notable deviation from isotropy in a, c, and p.

The Hill48 yield surfaces, obtained using different identification methods, and the Barlat89 model were plotted alongside the von Mises yield contour in Fig. 4.5. All yield surfaces were normalized using the yield stress in the rolling direction (RD). For this illustration, a section was taken in the σ_1–σ_2 plane, assuming zero shear stress.

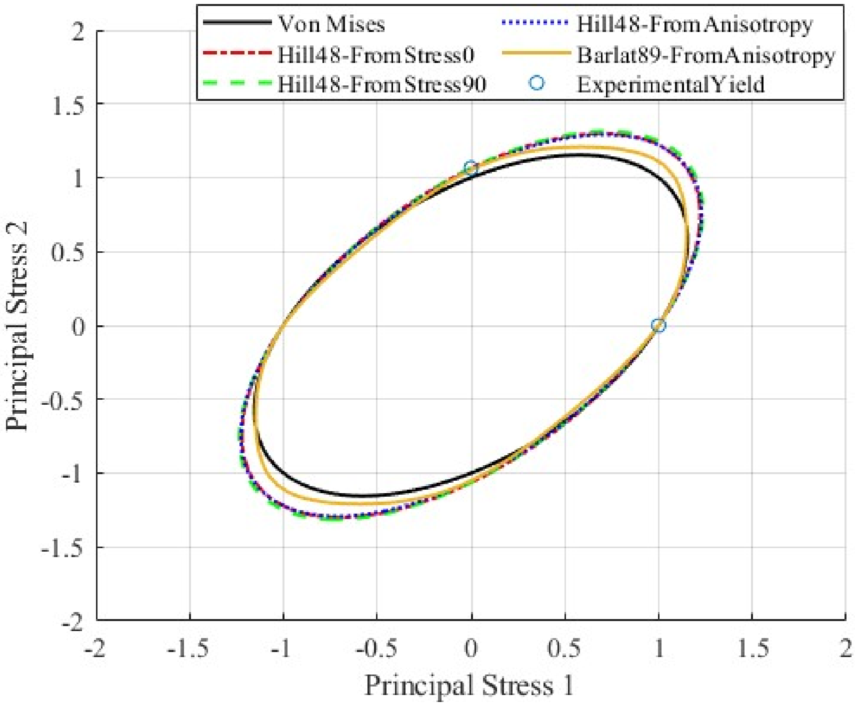

Figure 4.5: EN 1.4512 - Normalized Yield Contour

Note that normalizing the yield points by directly scaling with the yield stress in the RD can lead to an expanded contour, as the material exhibits hardening along this direction.

It is noteworthy that the curves from Hill48 nearly coincide, whereas the Barlat89 curve appears slightly less elongated. The von Mises curve only pass through the calibration point(yield stress with RD), while the Hill48 and Barlat89 pass through both points.

It's interesting to see the von Mises curve because it shows how different from an isotropic material the anisotropic curve is.

Assuming the uniaxial tensile test is aligned with the rolling direction (RD), and applying the previously defined rotation matrix to the load, the anisotropy and normalized yield stress with respect to RD were plotted. Figure 4.6 shows the Lankford coefficient and normalized tensile yield stress as functions of the angle relative to the RD.

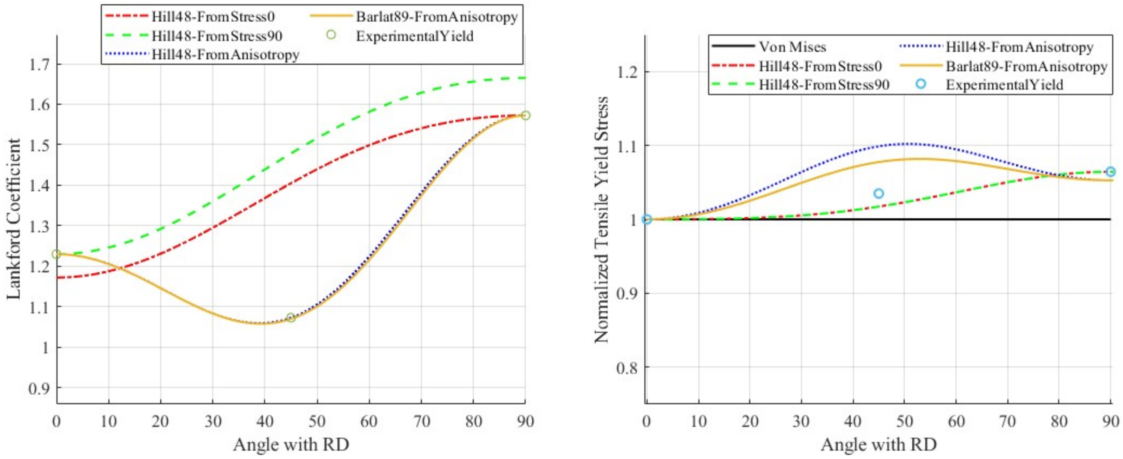

(a) Anisotropy with RD

(b) Yield Stress with RD

Figure 4.6: EN 1.4512 - Anisotropy and Yield Stress with RD

Note that the stress calibrated models(Hill48-FromStress0 and Hill48-FromStress90) won't pass through the experimental anisotropy. Differently, when calibrating through the anisotropy(Hill48-FromAnisotropy and Barlat89-FromAnisotropy) a different pattern can be observed.

Differently, in relation to the normalized yield stress, the stress calibrated models seems more precise.

After subtracting the r-values obtained from the models from the experimental values, the resulting deviations are presented in Tab. 4.8.

Model	r_0	Dev. 1	r_{45}	Dev. 2	r_{90}	Dev. 3	**Mean Error**
HillStress0	1.1717	-0.057	1.4048	0.3323	1.5722	0	0.1124
HillStress90	1.2295	0	1.4784	0.40590	1.6648	0.0926	0.1388
HillAnisotropic	1.2295	0	1.0725	0	1.5722	0	0
BarlatAnisotropic	1.2295	0	1.0725	0	1.5722	0	0

Table 4.8: EN 1.4512 - Comparison of r-values and deviations from experimental value for different models

Note in Tab. 4.8 that the deviations related to the anisotropy calibrated models are zero. However, the stress calibrated model displays higher deviations.

In addition r_{45} displays a much lower deviation when it's calculated from anisotropy.

Model	σ_{y0}	Dev. 1	σ_{y45}	Dev. 2	σ_{y90}	Dev. 3	**Mean Error**
HillStress0	1	0	1.0173	-0.01759	1.0644	0	0.00586
HillStress90	1	0	1.0173	-0.01759	1.0644	0	0.00586
HillAnisotropic	1	0	1.0988	0.06392	1.0528	-0.01157	0.02165
BarlatAnisotropic	1	0	1.0775	0.04262	1.0528	-0.01157	0.01472

Table 4.9: EN 1.4512 - Comparison of normalized yield strengths (S_y) and deviations from experimental value for different models

Otherwise, the stresses are much better approximated when using the stress to calculate the coefficients from Hill48 theory.

Then, to define the best method the root mean square error will be calculated for each of this methods, considering the three normalized yield stress deviations and the three anisotropy deviations the root mean square error will be calculated from Eq. 4.1.

$$RMSE = \sqrt{\frac{1}{n}\sigma_i(x_{EXP} - x_{ADJUSTED})^2} \tag{4.1}$$

Tab. 4.10 displays the results.

	HillStress0	HillStress90	HillAniso.	BarlatAniso.
RMSE	0.052 138	0.069 394	0.009 050 2	0.005 626 5

Table 4.10: EN 1.4512 - Root Mean Square Error

This indicates that the anisotropy calibrated models represents better the stress and the anisotropy at the same time than stress calibrated models. It is interesting as the yield stresses only carries information about the transition between plastic and elastic deformations, while the anisotropy carries information about all the uniform plastic deformation.

Furthermore, the Barlat89 is the best approach between this four different methods. This results was expectated because Barlat89 includes the cristalline structure and the Body Centered Cubic (BCC) contour tends to be smaller[46].

4.2.2 EN 1.4509 - Yield Criterion

The aforementioned analysis was subsequently subjected to further evaluation with respect to the EN 1.4509 material.

To calculate the Barlat89 and the Hill48 yield contour, the coefficients have been calculated according to Eqs. 3.10, 3.11 and 3.12.

Method	F	G	H	N
Hill48-FromStress0	0.3682	0.5112	0.4888	1.4139
Hill48-FromStress90	0.4224	0.5653	0.4347	1.3598
Hill48-FromAnisotropy	0.3274	0.5653	0.4347	1.0575
Method	a	c	h	p
Barlat89-FromAnisotropy	1.0041	0.9959	0.8730	0.8618

Table 4.11: EN 1.4509 - Anisotropy Coefficients

Tab. 4.11 shows the obtained coefficients. These values indicate a significant deviation from isotropy, particularly in the F term. Similar deviations can be observed in h and p.

The same methodology employed to plot Fig. 4.5 was employed in Fig. 4.7. Conversely, this material exhibits a different behavior from the past one. All the models tends to exhibit the same size, in exception of Hill48-FromStress90 which tends to be smaller.

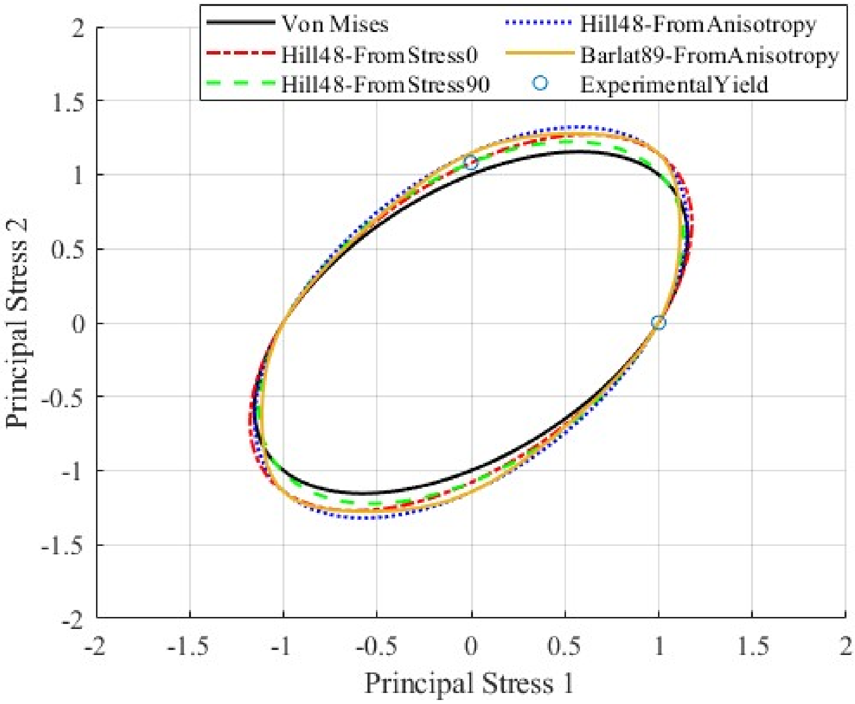

Figure 4.7: EN 1.4509 - Normalized Yield Contour

The Lankford Coefficient and the Normalized tensile yield stress have been plotted along to the RD in Fig. 4.8.

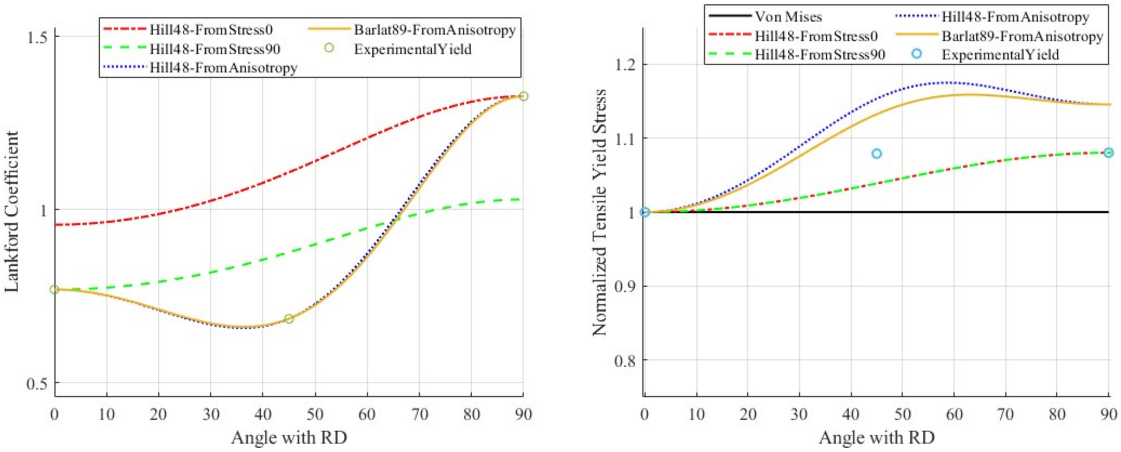

(a) Anisotropy with RD

(b) Yield Stress with RD

Figure 4.8: EN 1.4509 - Anisotropy and Yield Stress with RD

The same pattern is observed: the anisotropy-calibrated curves closely fit all anisotropy (r-value) points, while the stress-calibrated curves align more accurately with the yield stress data.

Next, by calculating the deviations from the experimental values, the accuracy of each model can be further assessed, as shown in Tab. 4.12 and 4.13.

Model	r_0	Dev. 1	r_{45}	Dev. 2	r_{90}	Dev. 3	**Mean Error**
HillStress0	0.9564	0.1874	1.1079	0.4233	1.3276	0	0.1543
HillStress90	0.7690	0	0.8768	0.1922	1.0293	-0.2984	0.1183
HillAnisotropic	0.7690	0	0.6846	0	1.3276	0	0
BarlatAnisotropic	0.7690	0	0.6848	0.0002	1.3276	0	0.0001

Table 4.12: EN 1.4509 - Comparison of anisotropy coefficients (r-values) and deviations from experimental value for different models

Model	σ_{y0}	Dev. 1	σ_{y45}	Dev. 2	σ_{y90}	Dev. 3	**Mean Error**
HillStress0	1	0	1.0387	-0.0402	1.0802	0	0.0134
HillStress90	1	0	1.0387	-0.0402	1.0802	0	0.0134
HillAnisotropic	1	0	1.1532	0.0742	1.1455	0.0653	0.0329
BarlatAnisotropic	1	0	1.1322	0.0532	1.1455	0.0653	0.0281

Table 4.13: EN 1.4509 - Comparison of normalized yield stresses (S_y) and deviations from experimental value for different models

Then the root mean square error can be calculated from Eq. 4.1.

	HillStress0	HillStress90	HillAniso.	BarlatAniso.
RMSE	0.061 397	0.049 854	0.010 07	0.008 956 1

Table 4.14: EN 1.4509 - Root Mean Square Error

The same pattern can be observed as Barlat89 tends to be more accurate while representing the anisotropy and the tensile yield strength at the same time. On the other hand, the difference between the HillAnisotropy and the Barlat89 RMSE was minor.

The yield stress is noteworthy in that it conveys information exclusively regarding the transition between plastic and elastic deformation. In contrast, the anisotropy is pertinent as it conveys information concerning the complete uniform plastic deformation behavior.

4.2.3 Forming Limit Diagram

The Forming Limit Diagram was predicted by Keeler and Abspoel et. al. method and the results have been exposed in Fig. 4.9.

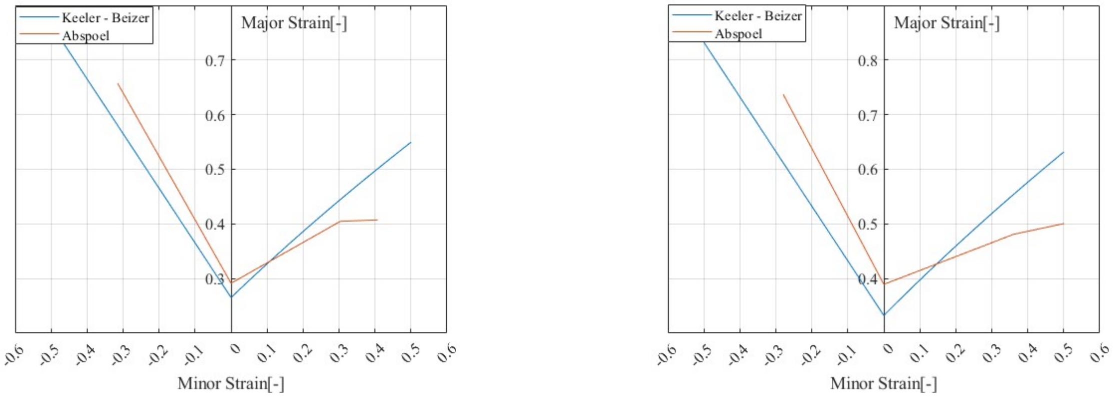

(a) EN 1.4512

(b) EN 1.4509

Figure 4.9: Predicted FLC for different materials

It is evident that the Keeler method is more conservative than the Abspoel method. The only region where the Keeler curve lies above the Abspoel curve is on the right-hand side of the diagram. Given that the Abspoel method provides a more accurate representation of material behavior, this suggests that it offers a better prediction of the localized necking occurance under a biaxial strain state.

Additionally, for both cases FLC_0 point in Keeler's method is lower than that of the plane strain from Abspoel method, which results in the entire curve being shifted downward.

4.3 Part 429x - Finite Element Method

After running the simulations the following results were obtained. It is imperative to note that all simulations will be incorporated into the Annex. However, a more thorough exposition will be allocated for the OP4, 5, and 7.

The left column includes the a view of the elements and the right column the FLD associated with each step.

As delinated in the Chapter 2 the FLC contains multiple lines that delineate significant intervals. The orange points means that the elements subject to this state of strain are exhibiting symptoms of excessive thinning and the red points are susceptible to cracking. The safety margin was set as 20[%].

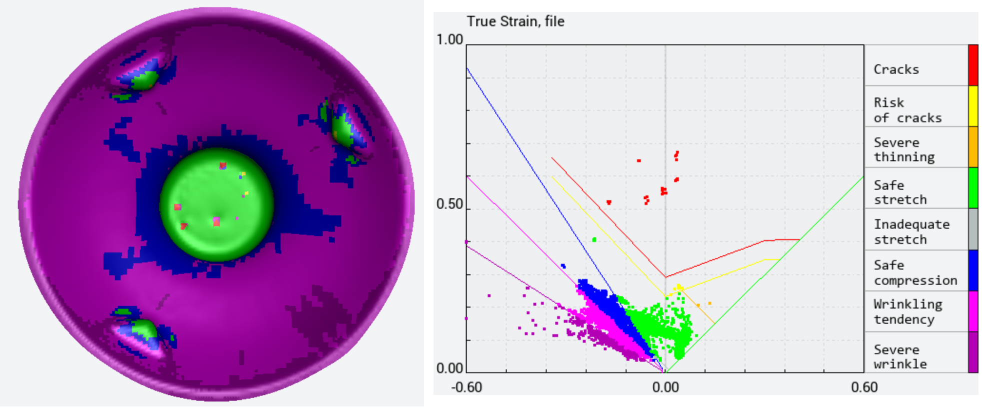

(a) OP4 - Part

(b) OP4 - FLD

Figure 4.10: Forming Limit Curve after OP4

Note that until OP4, it can be confirmed in the graph that the material is suffering a drawing operation because almost all the points are located to the left side of the FLD. Another important information is that the usable part of the piece is starting to show risk of cracks in the central part of the cone.

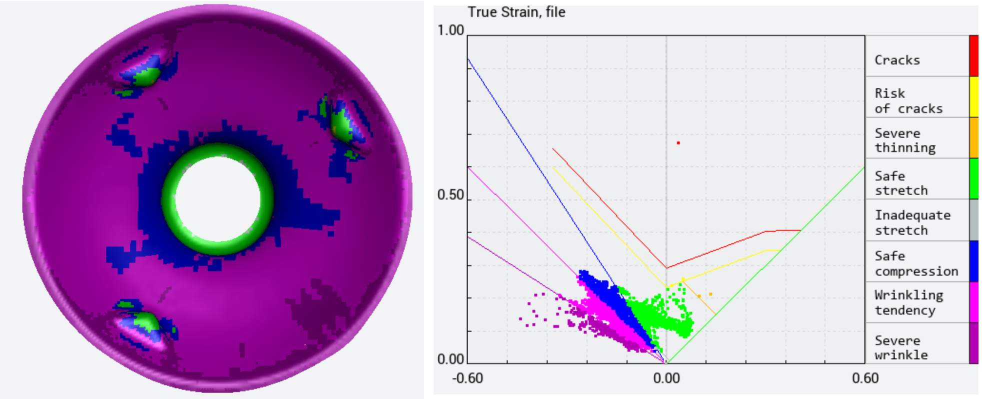

(a) OP5 - Part

(b) OP5 - FLD

Figure 4.11: Forming Limit Curve after OP5

The outcomes resulting from the trimming process are illustrated in Fig. 4.11. Note that the trimming operation will result in negligible deformation, as the FLD will not undergo significant progression.

Although, the crack region will be removed from the piece.

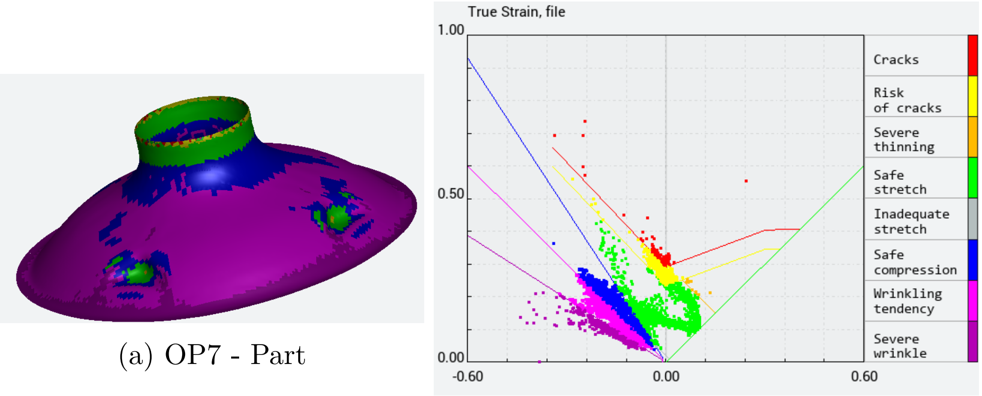

(a) OP7 - Part

(b) OP7 - FLD

Figure 4.12: Forming Limit Curve after OP7

The flanging operation, illustrated in Figure 4.12, represents the most critical stage of the forming process, as indicated by the red failure points. These points correspond with the defects observed in Figure 3.21. This is likely due to the onset of material stretching, as the forming limit diagram (FLD) shifts toward the right side of the curve, indicating higher strain levels. Additionally, some areas of the component exhibit excessive thinning, further confirming the severity of this operation.

The FSS has a lower resistance in the stretching part of the FLD[14] which justifies this behavior.

4.3.1 Extra observations

In between the moment where the punch press the blank counter the die and the initial movement of the punch an important behavior has been observed. Fig. 4.13 shows the associated results.

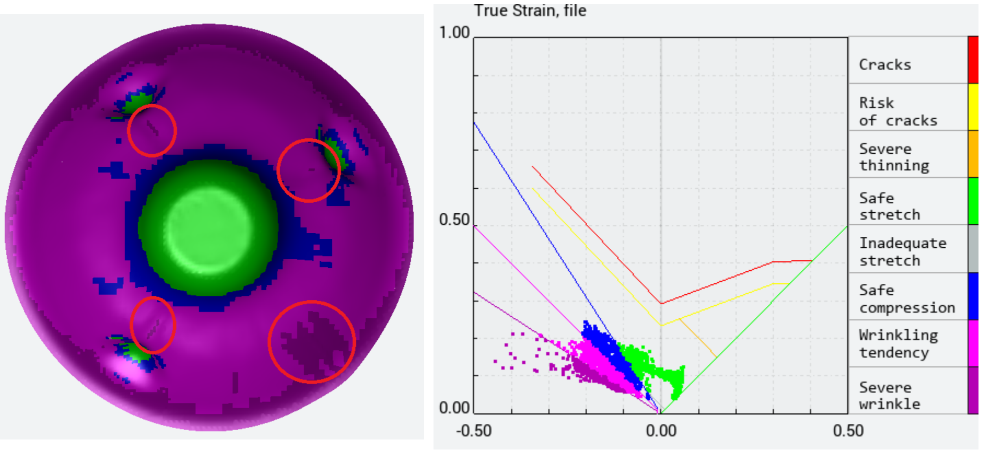

(a) During OP2 - Part

(b) During OP2 - FLD

Figure 4.13: Forming Limit Curve during OP2

During the forming process, additional phenomena were observed that, while not part of the main analysis, offer valuable insights into the behavior of the material and the forming tool interaction. Notably, regions adjacent to the notches exhibited significant wrinkling. This deformation results from the material being compressed between the punch and the die, leading to localized thickness increases.

These areas correspond to those shown in Figure 3.21, where the wrinkling can be linked to surface inconsistencies on the final part.

Also a section of the blank during the OP2 will be shown in Fig. 4.15. This section will be according to Fig. 4.14

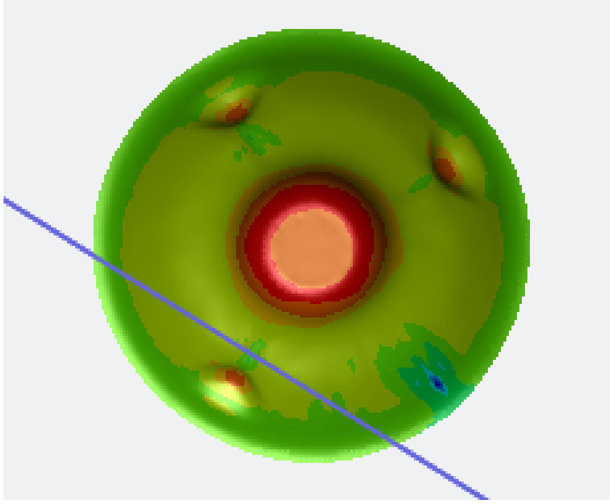

Figure 4.14: Section View

Fig. 4.15 shows a comparison of the section view during the operation and after the operation.

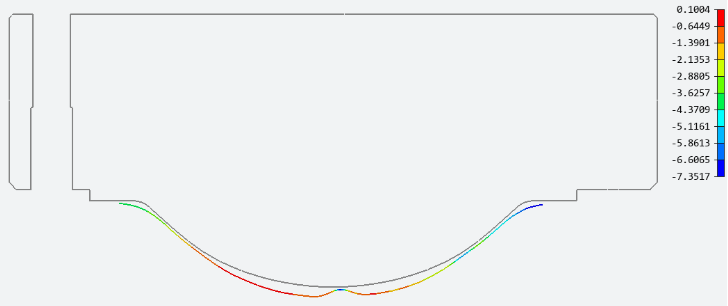

(a) During OP2 - Before pressing

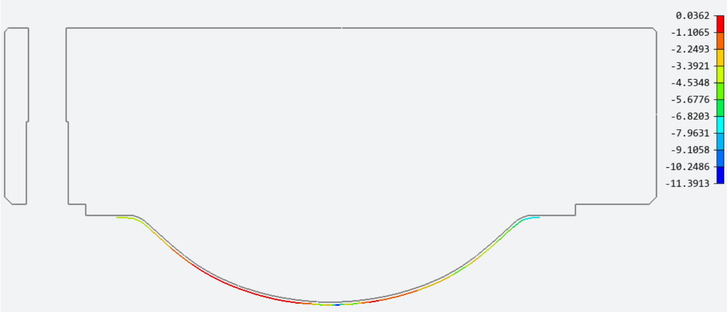

(b) During OP2 - After pressing

Figure 4.15: Thickening in the Stamping Part

The right scale represents the amount of thinning during the process. Negative values indicate a thickening tendency, while positive values indicate a thinning tendency.

It is clearly observed that wrinkling tends to occur at the central point, and in this region, the material exhibits a tendency to thicken.

4.3.2 The Lankford Ratio Optimized Aligned Blank

From the critical zone analysis, it has been discovered that by applying a rotation in the blank according to the reference axis. The r-value can be maximized in the desired locations.

By applying the obtained rotation angle, the Fig. 4.16 shows a contour plot containing the thinning percentage over the entire piece.

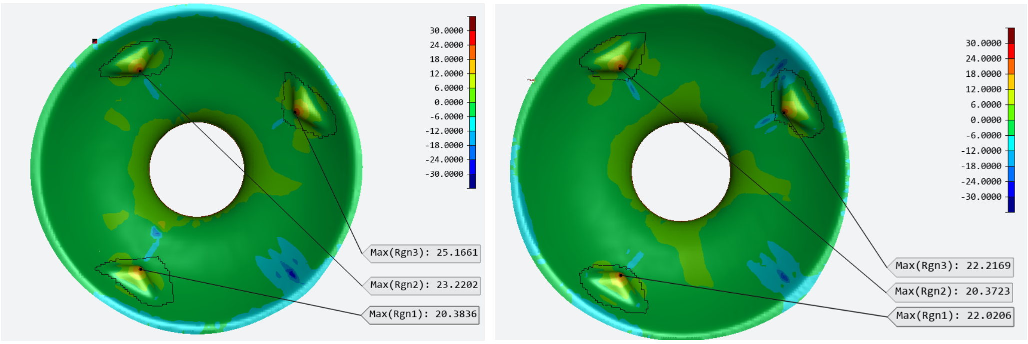

(a) Before Optimization (b) After Optimization

Figure 4.16: Thinning Percentage on the last stage

The three notches were defined as regions (1-3) and the maximum value extracted from each zone. By comparing the two contour plots, it can be verified that the maximum thinning at the notch was reduced from 25.1661[%] to 22.2169[%]. Also it can be observed a higher tendency to increase the thickness in front of the notches after optimization.

	Before[%]	After[%]
Region 1	20.3836	22.0206
Region 2	23.2202	20.3723
Region 3	25.1661	22.2169
Standard Deviation	1.964	0.827

Table 4.15: Thinning after and before optimization in each notch

Table 4.15 presents a comparison between the non-optimized and optimized blanks. The thinning reduction indicates better homogenization after optimization, as reflected by a lower standard deviation.

4.4 Piece 143x - Finite Element Method

Since only the first operation OP1 was evaluated. A more detailed result will be shown in this Section.

The FLD can be presented according to three different layers. The external layer, the middle layer and the internal layer. Fig. 4.17 shows the middle layer elements strain states.

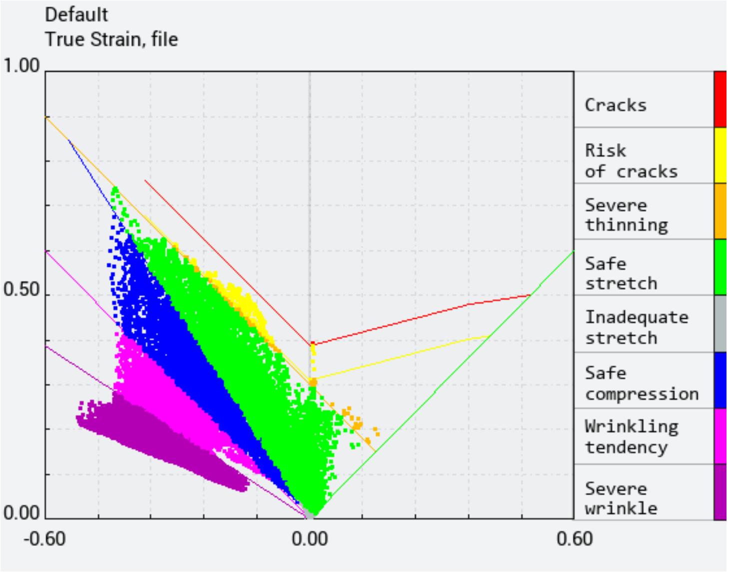

Figure 4.17: FLD Default settings - Middle Layer

The middle layer represents the neutral axis of the FLD which is under the less intense strain and stress states. It can be observed that the most part of the elements are at the left side of the FLD which is in accordance with the deep drawing process.

Fig. 4.18 shows the FLD behavior when evaluating the internal part of the stamping part.

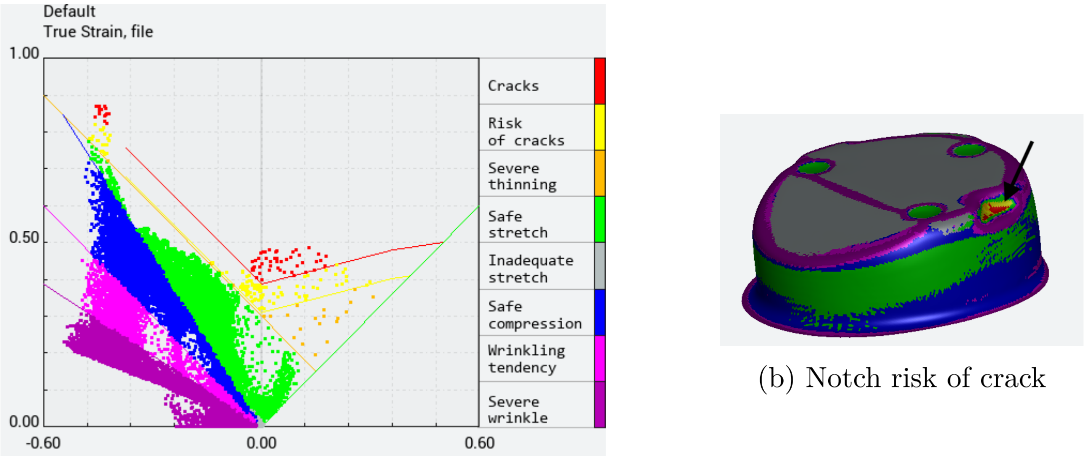

(a) FLD Default settings

(b) Notch risk of crack

Figure 4.18: Internal Layer Simulation

It can be observed that most of the part is subjected to safe strain levels, with the exception of two regions. The upper point on the FLD corresponds to the notch shown in (b). This notch is one of the regions subjected to tensile stress, which explains the high deformation intensity. In contrast, most of the part remains within the safe zone due to being primarily under compressive stress.

And the external layer of the Piece 143x is shown in Fig. 4.19.

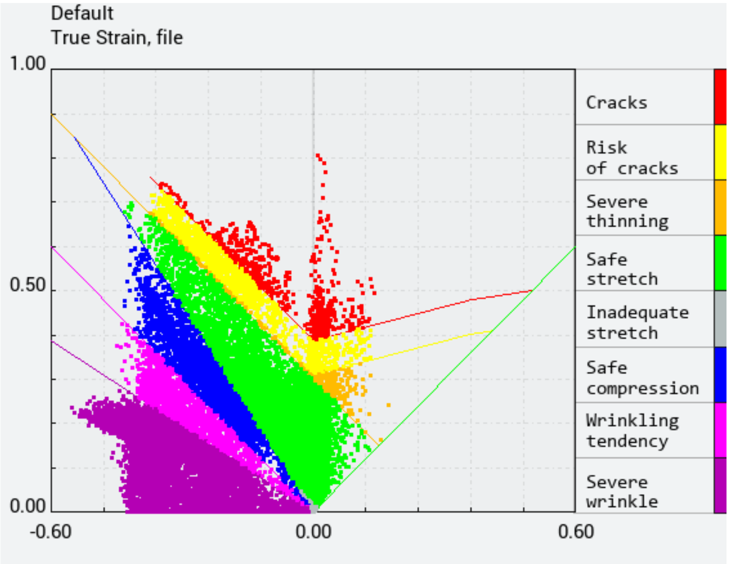

Figure 4.19: FLD Default settings - External Layer

As expected, this layer is where the most intense deformations occur due to the characteristic tensile stresses to which the part is subjected.

Now the failures which are occuring in the industry will be compared with the expected failures in the FEM model. Initially the crack next to the hole is shown in Fig. **??**. The location of the intended hole is indicated by a circle.

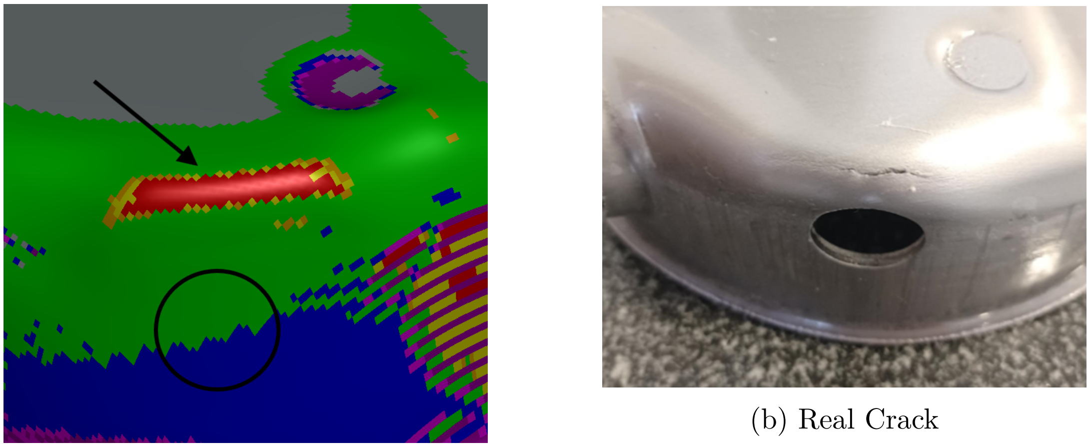

(a) Finite Element Model

(b) Real Crack

Source: Catraport

Figure 4.20: Failure Next to The Hole

It can be confirmed that this failure occurred exactly where it was expected for the measured properties.

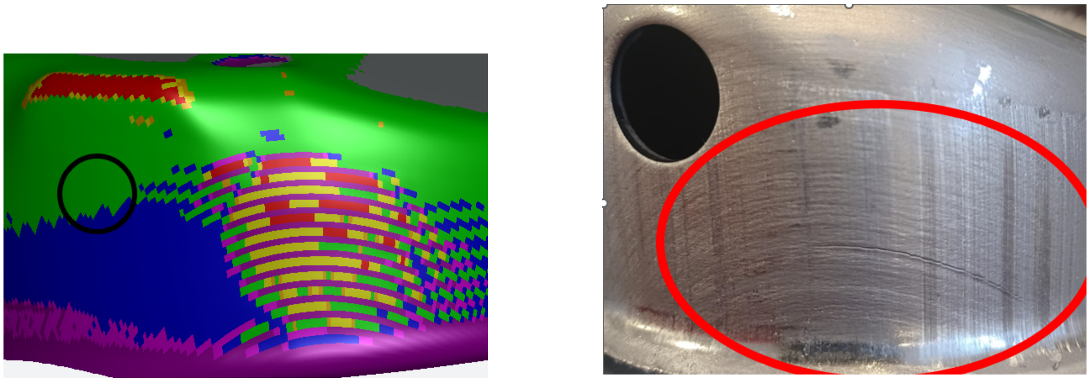

(a) Finite Element Model

(b) Real Crack and Ridging

Source: Catraport

Figure 4.21: Failure Left to the Hole

Additionally, at the left of the hole another failure can be seen. Fig. 4.21 shows the obtained results. It can be seen that the failures occurred as expected, following the same pattern observed in the FEM model. Additionally, this failure differs from the other due to ridging effects, which indicate that it is associated with extensive elongation in a uniaxial direction.

Lastly, the thinning was verified through the entire piece, but the most important results are exposed in Fig. 4.22.

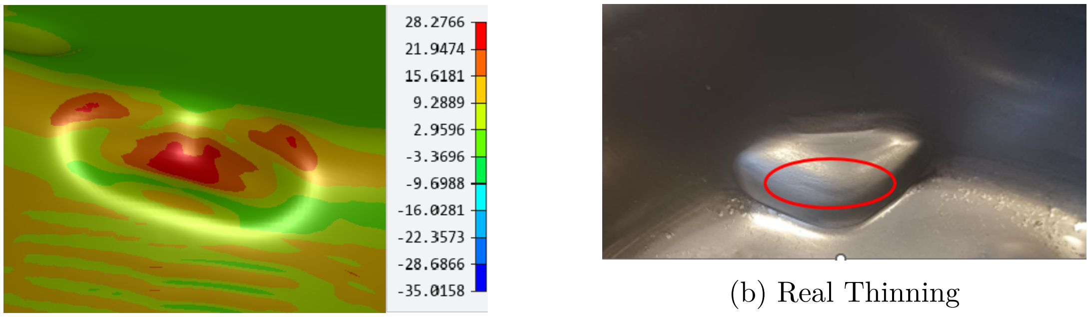

(a) Finite Element Model

(b) Real Thinning

Source: Catraport

Figure 4.22: Failure Left to the Hole

The (a) shows the percentage thinning associated in each section of the part. As the maximum amount allowed is 30%. It shows a really low tolerance as it reaches values as high as 28.2766 thinning percentage.

4.4.1 The effect of the R-value in the properties

The r_0, r_{45} and the r_{90} were increased and decreased by 10% simultaneously. The effect in the FLD and each simulation has been evaluated and compared.

Fig. 4.23 presents the results after reducing the r-values by 10%. For comparison, the default result is shown on the left. It can be clearly observed that as the r-value decreases, the crack region and areas of severe thinning become more pronounced.

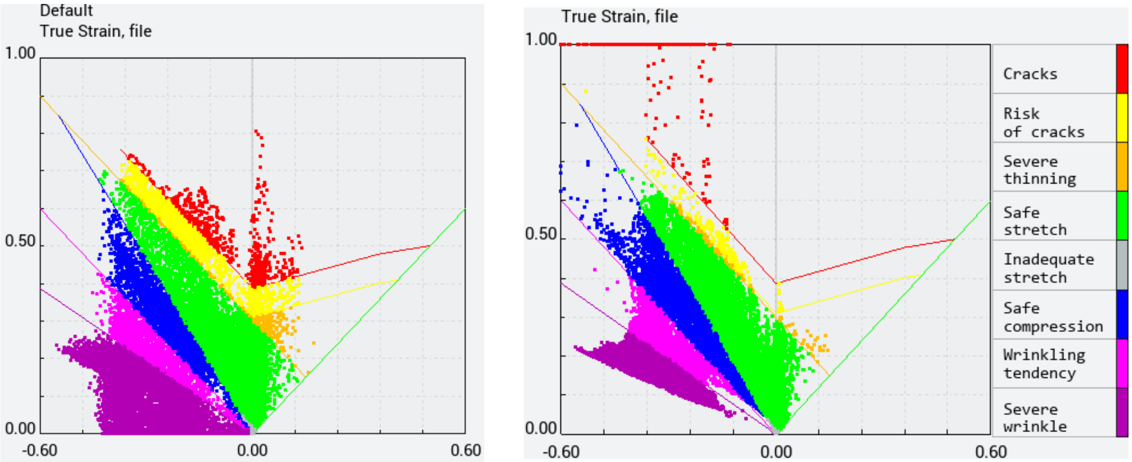

(a) Default

(b) Minus 10%

Figure 4.23: Forming Limit Diagrams after OP1 - Minus 10% case

Alternatively, it can be observed in Fig. 4.24 that the failure during OP1 begins to appear. This suggests that a slight deviation of 10% in the r-value could be one of the factors contributing to the occurrence of this failure.

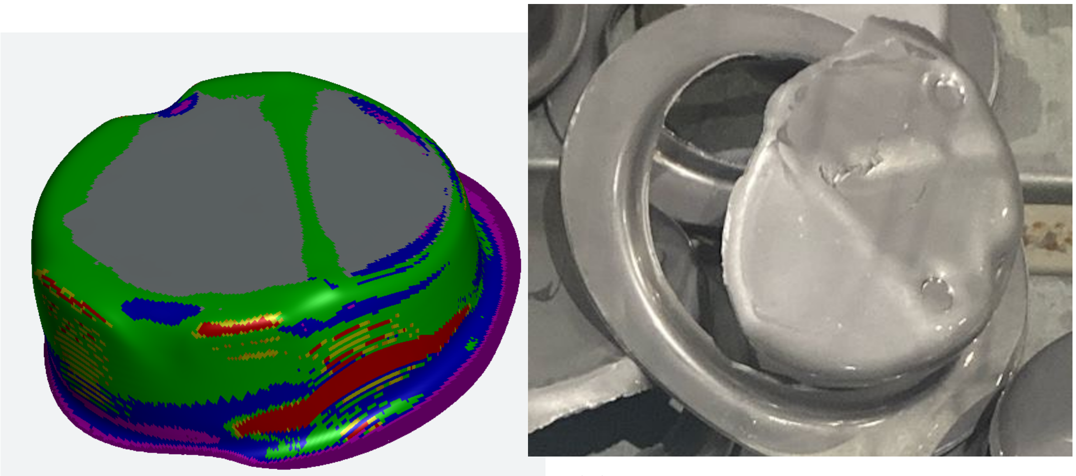

(a) Anisotropy with RD

(b) Part 143x - Failure During OP1

Source: Catraport

Figure 4.24: Minus 10%

Fig. 4.25 shows the results after increasing the $r-$values.

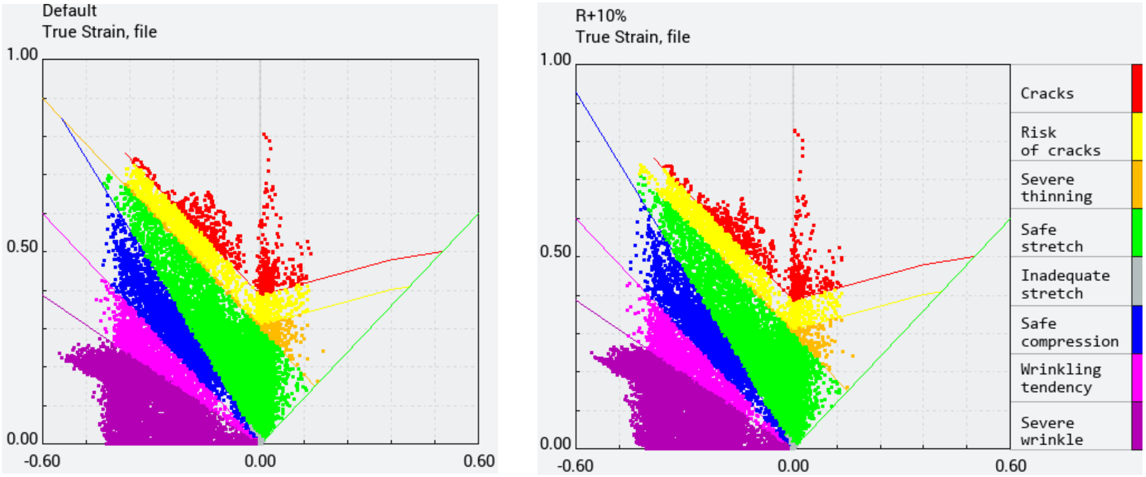

(a) Default

(b) Plus 10%

Figure 4.25: Forming Limit Diagrams after OP1 - Plus 10% case

Observe that as the $r-$value increases, a reduction in thinning points can be observed. Also, the crack susceptible points have been reduced.

Subsequently, the aforementioned procedure was replicated for an isotropic material. This indicates that the Lankford coefficients are being treated as a singular value. The results are shown in Fig. 4.26.

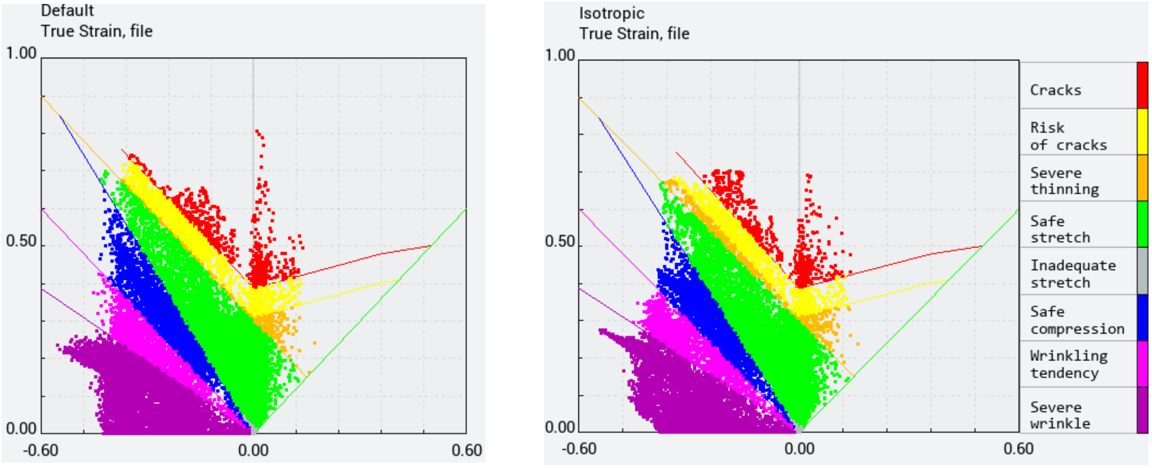

(a) Default

(b) Isotropic

Figure 4.26: Forming Limit Diagrams after OP1 - Isotropic case

It is noteworthy that the severe thinning points have substantially increased. This result is consistent with the theory, as the Lankford ratio measures a material's resistance to thinning during a tensile test.

Additionally, the strain states tend to concentrate more toward the center. When the material is isotropic, the strain distribution tends to be more uniform and well-distributed across the entire sheet, whereas anisotropy leads to localized deformation.

Chapter 5

Conclusions and Future Works

This chapter presents the main conclusions obtained from this work and the improvement possibilities.

5.1 Conclusions

This work provided valuable learning opportunities throughout its duration. Key topics included the tensile test, DIC, anisotropy, and finite element simulations.

After performing experimental camera calibration, the need for calibration in this setup was confirmed. The error along the abscissa (x-axis) was negligible, whereas the uncalibrated camera could introduce errors of up to $0.3[mm]$ along the ordinate (y-axis).

After obtaining the anisotropy results, both materials exhibited a U-shaped pattern with respect to the rolling direction. This trend is also reported in the literature, confirming the validity of the results. The EN 1.4512 sheet ($1.2[mm]$) showed higher anisotropy, whereas the EN 1.4509 sheet ($3.0[mm]$) exhibited lower values. However, as noted by Maruma *et al.*, anisotropy is highly dependent on the material's strain history, [29]. As a result, no consistent or definitive value can be established. Furthermore, Krevicz observed a strong dependence of anisotropy on sheet thickness [37], suggesting that thinner materials undergo more plastic deformation during processing, which leads to increased anisotropy.

This information could be particularly interesting as Barros verified that the traditional tensile test cannot characterize completely the material because it's behavior is highly dependent on the microstructure, yet in advanced high strength steels, [58].

Reducing the r-values by 10% led to the most critical failure in Part 143x, indicating that even slight variations in anisotropy—while maintaining the same mechanical properties—can significantly affect formability. This confirms that traditional tensile tests alone are insufficient to fully characterize material behavior. In such cases, information about the material's processing history, including hot and cold working or annealing treatments, could be particularly valuable.

Overall, the FEM proved to be an excellent tool for evaluating failures in the stamping process, identifying critical regions, and supporting process optimization. Every failure reproduced in the simulated operations was accurately identified using FEM. Moreover, the simulations revealed additional phenomena—such as local thickening tendencies—that were not initially recognized as failures. Further investigation is needed, as the observed thickening could potentially restrict material flow during the stamping operation.

Additionally, it was observed that a simple analytical approach, such as rotating the blank, can be effective in reducing thinning. When compared with simulation results, this strategy led to a more uniform thickness distribution. However, this method is inherently limited by the geometry of the part.

5.2 Future Works

Setting up the Nakajima test within the FEM environment and calibrating it experimentally could be particularly interesting, as this approach could later be extended to a wide range of materials.

To calibrate the Nakajima test, employing three-dimensional DIC presents a promising opportunity—not only to improve the precision of the test but also to deepen my skills in working with DIC.

Another valuable learning opportunity could be conducting biaxial testing to investigate its influence on yield stress contours. Previous research has indicated that models such as Hill48 and Barlat89 may not accurately predict material behavior in the biaxial stretching region, [47].

Additionally, evaluating the effects of die wear on formability could be an important improvement and contribute to a better understanding of the forming process under realistic manufacturing conditions.

Determining the changes in material properties along the thickness (normal) direction of the blank could also be of interest, as these properties may vary due to the rolling and cooling processes. This analysis is particularly important because each layer of the stamped component experiences different stress and strain states during forming.

Bibliography

[1] European Commission, *Transport and the green deal*, Accessed: 2025-02-20, 2025. [Online]. Available: `https://commission.europa.eu/strategy-and-policy/priorities-2019-2024/european-green-deal/transport-and-green-deal_en`.

[2] E. Kritsanaviparkporn, F. M. Baena-Moreno, and T. R. Reina, "Catalytic converters for vehicle exhaust: Fundamental aspects and technology overview for newcomers to the field," *Chemistry*, vol. 3, no. 2, pp. 630–646, 2021.

[3] Y. Inoue and M. Kikuchi, "Present and future trends of stainless steel for automotive exhaust system," *High-temperature*, vol. 950, p. 750, 2003.

[4] T. Ohata, Y. Nakamura, T. Katayama, E. Nakamachi, and K. Nakano, "Development of optimum process design system by numerical simulation," *Journal of Materials Processing Technology*, vol. 60, no. 1, pp. 543–548, 1996, Proceedings of the 6th International Conference on Metal Forming, ISSN: 0924-0136. DOI: `https://doi.org/10.1016/0924-0136(96)02384-9`. [Online]. Available: `https://www.sciencedirect.com/science/article/pii/0924013696023849`.

[5] J. Fish and T. Belytschko, *A First Course in Finite Elements.* Wiley, 2007, ISBN: 9780470035801.

[6] A. Makinouchi, "Sheet metal forming simulation in industry," *Journal of Materials Processing Technology*, vol. 60, no. 1, pp. 19–26, 1996, Proceedings of the 6th International Conference on Metal Forming, ISSN: 0924-0136. DOI: `https://`

doi.org/10.1016/0924-0136(96)02303-5. [Online]. Available: https://www.sciencedirect.com/science/article/pii/0924013696023035.

[7] R. Norton, K. Stavropoulos, J. de Aguiar, *et al.*, *Projeto de Máquinas: Uma Abordagem Integrada*. Bookman, 2013, ISBN: 9788582600221.

[8] J. Hu, Z. Marciniak, and J. Duncan, *Mechanics of Sheet Metal Forming*. Elsevier Science, 2002, ISBN: 9780080496511.

[9] I. O. for Standardization, *Iso 10113: Metallic materials – determination of planar anisotropy*, Standard, Provides methods for determining the planar anisotropy of metallic materials, particularly sheet metals., Geneva, Switzerland: International Organization for Standardization, 2020.

[10] *Metallic materials — sheet and strip — determination of forming-limit curves — part 2: Determination of forming-limit curves in the laboratory*, Standard, Geneva, Switzerland: International Organization for Standardization, 2008.

[11] K. Lo, C. Shek, and J. Lai, "Recent developments in stainless steels," *Materials Science and Engineering: R: Reports*, vol. 65, no. 4, pp. 39–104, 2009, ISSN: 0927-796X. DOI: https://doi.org/10.1016/j.mser.2009.03.001. [Online]. Available: https://www.sciencedirect.com/science/article/pii/S0927796X09000461.

[12] K. Cashell and N. Baddoo, "Ferritic stainless steels in structural applications," *Thin-Walled Structures*, vol. 83, pp. 169–181, 2014, ADVANCES IN STRUCTURAL STAINLESS STEEL RESEARCH, ISSN: 0263-8231. DOI: https://doi.org/10.1016/j.tws.2014.03.014. [Online]. Available: https://www.sciencedirect.com/science/article/pii/S0263823114001074.

[13] European Committee for Standardization, *EN 10088-1: Stainless steels - Part 1: List of stainless steels*, Brussels, 2014.

[14] J. Charles, J.-D. Mithieux, P.-O. Santacreu, and L. Peguet, "The ferritic stainless family: The appropriate answerto nickel volatility?" *Metallurgical Research & Technology*, vol. 106, no. 3, pp. 124–139, 2009.

[15] Y. Zhao, H.-L. Liu, L.-L. Wei, and L.-Q. Chen, “An overview on the novel heat-resistant ferritic stainless steels,” *Tungsten*, vol. 5, no. 4, pp. 467–480, Dec. 2023, ISSN: 2661-8036. DOI: `10.1007/s42864-022-00171-4`. [Online]. Available: `https://doi.org/10.1007/s42864-022-00171-4`.

[16] Y. Yu, S. Shironita, K. Souma, and M. Umeda, “Effect of chromium content on the corrosion resistance of ferritic stainless steels in sulfuric acid solution,” *Heliyon*, vol. 4, no. 11, e00958, 2018, ISSN: 2405-8440. DOI: `https://doi.org/10.1016/j.heliyon.2018.e00958`. [Online]. Available: `https://www.sciencedirect.com/science/article/pii/S2405844018315226`.

[17] B. Fatfat, “Niobium-alloyed stainless steel for automotive exhaust systems,” Ph.D. dissertation, Politecnico di Torino, 2021.

[18] P. Wu, H. Jin, Y. Shi, and D. Lloyd, “Analysis of ridging in ferritic stainless steel sheet,” *Materials Science and Engineering: A*, vol. 423, no. 1, pp. 300–305, 2006, Mechanical Behaviour of Micro- and Nano-scale Systems, ISSN: 0921-5093. DOI: `https://doi.org/10.1016/j.msea.2006.02.043`. [Online]. Available: `https://www.sciencedirect.com/science/article/pii/S0921509306002450`.

[19] H.-C. Chao, “Recent studies into the mechanism of ridging in ferritic stainless steels,” *Metallurgical Transactions*, vol. 4, no. 4, pp. 1183–1186, 1973, ISSN: 2379-0083. DOI: `10.1007/BF02645630`. [Online]. Available: `https://doi.org/10.1007/BF02645630`.

[20] V. Talyan, R. Wagoner, and J. Lee, “Formability of stainless steel,” *Metallurgical and Materials Transactions A*, vol. 29, pp. 2161–2172, 1998.

[21] W. Lopes, “Estudo do encruamento dos aços aisi 304 e aisi 409 com uso da técnica de cisalhamento planar simples,” Tese de Doutorado, Universidade Federal de Minas Gerais, Belo Horizonte, Brazil, 2009. [Online]. Available: `http://hdl.handle.net/1843/BUOS-8DVHHY`.

[22] F. Gao, Q. Zhu, W. Xue, *et al.*, “Correlation between formability, ridging and recrystallization texture development in ferritic stainless steel fabricated by introducing intermediate annealing during cold rolling,” *Materials Characterization*, vol. 205, p. 113 296, 2023, ISSN: 1044-5803. DOI: `https://doi.org/10.1016/j.matchar.2023.113296`. [Online]. Available: `https://www.sciencedirect.com/science/article/pii/S1044580323006551`.

[23] Aperam, *Inox no setor automotivo*, Accessed: 2025-04-24, n.d. [Online]. Available: `https://www.aperam.com/sites/default/files/documents/Aperam%20-%20Inox%20no%20setor%20Automotivo.pdf`.

[24] M. Groover, *Fundamentals of Modern Manufacturing: Materials, Processes, and Systems*. John Wiley & Sons, 2010, ISBN: 9780470467008.

[25] H. Gupta and P. (Firm), *Manufacturing Process*. New Age International Limited, 2009.

[26] G. Dieter and G. Dieter, *Mechanical Metallurgy*, ser. Metallurgy and metallurgical engineering series. CreateSpace Independent Publishing Platform, 2014, ISBN: 9781502528636.

[27] T. Lyman, *Metals Handbook: Vol.1: Properties and Selection of Metals*, vol. 1. ASM, 1961. [Online]. Available: `https://books.google.pt/books?id=dwHr0AEACAAJ`.

[28] B. K. Santos and M. L. Quadros, *Processo de conformação*. Grupo A, ISBN: 9788595024878. [Online]. Available: `https://integrada.minhabiblioteca.com.br/#/books/9788595024878/`.

[29] M. G. Maruma *et al.*, “Effect of composition and thermomechanical processing on the texture evolution, formability and ridging behavior of type aisi 441 ferritic stainless steel,” Ph.D. dissertation, University of Pretoria, 2013.

[30] F. L. D. de Morais, E. C. S. Corrêa, and W. Lopes, “Study of aisi 409 stainless steel formability under complex deformation routes,” pt, *Tecnologia em Metalurgia,*

Materiais e Mineração, vol. 18, e2336, 2021. DOI: `10.4322/2176-1523.20212336`. [Online]. Available: `http://dx.doi.org/10.4322/2176-1523.20212336`.

[31] J. Ma, X. Tang, Y. Hou, H. Li, J. Lin, and M. Fu, "Defects in metal-forming: Formation mechanism, prediction and avoidance," *International Journal of Machine Tools and Manufacture*, vol. 207, p. 104 268, 2025, ISSN: 0890-6955. DOI: `https://doi.org/10.1016/j.ijmachtools.2025.104268`. [Online]. Available: `https://www.sciencedirect.com/science/article/pii/S0890695525000239`.

[32] F. Beer, E. Jr. Johnston, J. DeWolf, and D. Mazurek, *Mechanics of Materials*. McGraw-Hill Education, 2011, ISBN: 9780073380285.

[33] Z. Marciniak and K. Kuczyński, "Limit strains in the processes of stretch-forming sheet metal," *International Journal of Mechanical Sciences*, vol. 9, no. 9, pp. 609–620, 1967, ISSN: 0020-7403. DOI: `https://doi.org/10.1016/0020-7403(67)90066-5`. [Online]. Available: `https://www.sciencedirect.com/science/article/pii/0020740367900665`.

[34] M. Sutton, J. Yan, V. Tiwari, H. Schreier, and J. Orteu, "The effect of out-of-plane motion on 2d and 3d digital image correlation measurements," *Optics and Lasers in Engineering*, vol. 46, no. 10, pp. 746–757, 2008, ISSN: 0143-8166. DOI: `https://doi.org/10.1016/j.optlaseng.2008.05.005`. [Online]. Available: `https://www.sciencedirect.com/science/article/pii/S0143816608000985`.

[35] N. McCormick and J. Lord, "Digital image correlation," *Materials Today*, vol. 13, no. 12, pp. 52–54, 2010, ISSN: 1369-7021. DOI: `https://doi.org/10.1016/S1369-7021(10)70235-2`. [Online]. Available: `https://www.sciencedirect.com/science/article/pii/S1369702110702352`.

[36] V.-T. Nguyen, S.-J. Kwon, O.-H. Kwon, and Y.-S. Kim, "Mechanical properties identification of sheet metals by 2d-digital image correlation method," *Procedia Engineering*, vol. 184, pp. 381–389, 2017, Advances in Material Processing Technologies Conference, ISSN: 1877-7058. DOI: `https://doi.org/10.1016/j.proeng.`

2017.04.108. [Online]. Available: https://www.sciencedirect.com/science/article/pii/S1877705817316132.

[37] A. R. Krevicz, "Simulação numérica e avaliação experimental dos parâmetros envolvidos na estampagem de chapas de aço," M.S. thesis, Instituto Politecnico de Braganca (Portugal), 2022.

[38] Y. H. Wang, J. H. Jiang, C. Wanintrudal, *et al.*, "Whole field sheet-metal tensile test using digital image correlation," *Experimental Techniques*, vol. 34, no. 2, pp. 54–59, 2010, ISSN: 1747-1567. DOI: 10.1111/j.1747-1567.2009.00483.x. [Online]. Available: https://doi.org/10.1111/j.1747-1567.2009.00483.x.

[39] F. Devernay and O. Faugeras, "Straight lines have to be straight," *Machine Vision and Applications*, vol. 13, no. 1, pp. 14–24, Aug. 2001, ISSN: 1432-1769. DOI: 10.1007/PL00013269. [Online]. Available: https://doi.org/10.1007/PL00013269.

[40] Z. Zhang, "A flexible new technique for camera calibration," *IEEE Transactions on Pattern Analysis and Machine Intelligence*, vol. 22, no. 11, pp. 1330–1334, 2000. DOI: 10.1109/34.888718.

[41] O. Cazacu and B. Revil-Baudard, *Plasticity of Metallic Materials: Modeling and Applications to Forming*, ser. Elsevier Series on Plasticity of Materials. Elsevier, 2020, ISBN: 9780128179857. [Online]. Available: https://books.google.pt/books?id=c0TsDwAAQBAJ.

[42] S. K. Paul, "Controlling factors of forming limit curve: A review," *Advances in Industrial and Manufacturing Engineering*, vol. 2, p. 100 033, 2021, ISSN: 2666-9129. DOI: https://doi.org/10.1016/j.aime.2021.100033. [Online]. Available: https://www.sciencedirect.com/science/article/pii/S2666912921000039.

[43] "Metallic materials — sheet and strip — determination of plastic strain ratio," International Organization for Standardization, Geneva, CH, Standard, Mar. 2020.

[44] R. Wang, Z. Li, X. Yang, and L. Cheng, "Effect of secondary cold-rolled and annealing on ridging and corrosion properties of 430 ferritic stainless steel," *Journal of Materials Research and Technology*, vol. 36, pp. 7783–7797, 2025, ISSN: 2238-7854. DOI: `https://doi.org/10.1016/j.jmrt.2025.05.048`. [Online]. Available: `https://www.sciencedirect.com/science/article/pii/S2238785425012037`.

[45] R. Hill and E. Orowan, "A theory of the yielding and plastic flow of anisotropic metals," *Proceedings of the Royal Society of London. Series A. Mathematical and Physical Sciences*, vol. 193, no. 1033, pp. 281–297, 1948. DOI: `10.1098/rspa.1948.0045`. eprint: `https://royalsocietypublishing.org/doi/pdf/10.1098/rspa.1948.0045`. [Online]. Available: `https://royalsocietypublishing.org/doi/abs/10.1098/rspa.1948.0045`.

[46] F. Barlat and K. Lian, "Plastic behavior and stretchability of sheet metals. part i: A yield function for orthotropic sheets under plane stress conditions," *International Journal of Plasticity*, vol. 5, no. 1, pp. 51–66, 1989, ISSN: 0749-6419. DOI: `https://doi.org/10.1016/0749-6419(89)90019-3`. [Online]. Available: `https://www.sciencedirect.com/science/article/pii/0749641989900193`.

[47] Y. Lou, G. Bae, C. Lee, C. Park, and H. Buh, "Performance evaluation of barlat's and bbc yield criteria based on directionalities of r-values and yield stresses," Korea Advanced Institute of Science and Technology (KAIST), Technical Report, Oct. 2009.

[48] M. Nurcheshmeh and D. E. Green, "Prediction of sheet forming limits with marciniak and kuczynski analysis using combined isotropic–nonlinear kinematic hardening," *International Journal of Mechanical Sciences*, vol. 53, no. 2, pp. 145–153, 2011, ISSN: 0020-7403. DOI: `https://doi.org/10.1016/j.ijmecsci.2010.12.004`. [Online]. Available: `https://www.sciencedirect.com/science/article/pii/S0020740310002791`.

[49] F. Dunne and N. Petrinic, *Introduction to computational plasticity*. Oxford University Press, 2005.

[50] A. Singh, S. Basak, L. P. P.S., *et al.*, "Prediction of earing defect and deep drawing behavior of commercially pure titanium sheets using cpb06 anisotropy yield theory," *Journal of Manufacturing Processes*, vol. 33, pp. 256–267, 2018, ISSN: 1526-6125. DOI: `https://doi.org/10.1016/j.jmapro.2018.05.003`. [Online]. Available: `https://www.sciencedirect.com/science/article/pii/S1526612518304286`.

[51] R. Zhang, Z. Shi, Z. Shao, V. A. Yardley, J. Lin, and T. A. Dean, "Biaxial test method for determination of flcs and fflcs for sheet metals: Validation against standard nakajima method," *International Journal of Mechanical Sciences*, vol. 209, p. 106 694, 2021, ISSN: 0020-7403. DOI: `https://doi.org/10.1016/j.ijmecsci.2021.106694`. [Online]. Available: `https://www.sciencedirect.com/science/article/pii/S0020740321004252`.

[52] S. Keeler and B. WG, "Relationship between laboratory material characterization and press-shop formability," 1975.

[53] M. Abspoel, M. E. Scholting, and J. M. Droog, "A new method for predicting forming limit curves from mechanical properties," *Journal of Materials Processing Technology*, vol. 213, no. 5, pp. 759–769, 2013, ISSN: 0924-0136. DOI: `https://doi.org/10.1016/j.jmatprotec.2012.11.022`. [Online]. Available: `https://www.sciencedirect.com/science/article/pii/S0924013612003470`.

[54] T. Belytschko and I. Leviathan, "Physical stabilization of the 4-node shell element with one point quadrature," *Computer Methods in Applied Mechanics and Engineering*, vol. 113, no. 3, pp. 321–350, 1994, ISSN: 0045-7825. DOI: `https://doi.org/10.1016/0045-7825(94)90052-3`. [Online]. Available: `https://www.sciencedirect.com/science/article/pii/0045782594900523`.

[55] E. N. Dvorkin and K.-J. Bathe, "A continuum mechanics based four-node shell element for general non-linear analysis," *Engineering computations*, vol. 1, no. 1, pp. 77–88, 1984.

[56] Z. Luo and Y. Zhao, "A survey of finite element analysis of temperature and thermal stress fields in powder bed fusion additive manufacturing," *Additive Manufacturing*, vol. 21, pp. 318–332, 2018, ISSN: 2214-8604. DOI: `https://doi.org/10.1016/j.addma.2018.03.022`. [Online]. Available: `https://www.sciencedirect.com/science/article/pii/S2214860417301148`.

[57] A. Papoutsakis, S. S. Sazhin, S. Begg, I. Danaila, and F. Luddens, "An efficient adaptive mesh refinement (amr) algorithm for the discontinuous galerkin method: Applications for the computation of compressible two-phase flows," *Journal of Computational Physics*, vol. 363, pp. 399–427, 2018, ISSN: 0021-9991. DOI: `https://doi.org/10.1016/j.jcp.2018.02.048`. [Online]. Available: `https://www.sciencedirect.com/science/article/pii/S0021999118301372`.

[58] A. F. R. Barros, "Simulação de processos de estampagem pelo método de elementos finitos," M.S. thesis, Instituto Politecnico do Porto (Portugal), 2023.

[59] I. O. for Standardization, *Iso 6892-1: Metallic materials – tensile testing – part 1: Method of test at room temperature*, Standard, Specifies the method for tensile testing of metallic materials at room temperature., Geneva, Switzerland: International Organization for Standardization, 2019.

[60] C. d. P. C. Pisano, "Caracterização e comparação dos procedimentos de obtenção da curva limite de conformação e das caracterısticas de estampagem dos aços inoxidáveis din 1.4509 e aisi 321.," Ph.D. dissertation, Universidade de São Paulo, 2017.

[61] M. Poncelet and H. Leclerc, "A Digital Image Correlation algorithm with light reflection compensation," *Experimental Mechanics*, vol. 55, no. 7, pp. 1317–1327, 2015. DOI: `10.1007/s11340-015-0037-x`. [Online]. Available: `https://hal.science/hal-01576735`.

[62] A. Hijazi, A. Friedl, and C. Kähler, "Influence of camera's optical axis non-perpendicularity on measurement accuracy of two-dimensional digital image correlation," *JJMIE*, vol. 5, no. 4, pp. 1–10, 2011.

[63] International Organization for Standardization, *Metallic materials — Sheet and strip — Determination of tensile strain hardening exponent*, Geneva, Switzerland, 2007.

[64] Z. I. Q. Solutions, *Metrology software*, Accessed: 2025-02-20, 2025. [Online]. Available: `https://www.zeiss.com/metrology/en/software/metrology-software.html`.

[65] ——, *Digital image correlation: Motion and deformation analysis*, Accessed: 2025-02-20, 2025. [Online]. Available: `https://www.zeiss.com/metrology/en/explore/topics/digital-image-correlation.html`.

[66] P. Dasappa, K. Inal, and R. Mishra, "The effects of anisotropic yield functions and their material parameters on prediction of forming limit diagrams," *International Journal of Solids and Structures*, vol. 49, no. 25, pp. 3528–3550, 2012, New Challenges in Mechanics Materials for Sheet Metal Forming, ISSN: 0020-7683. DOI: `https://doi.org/10.1016/j.ijsolstr.2012.04.021`. [Online]. Available: `https://www.sciencedirect.com/science/article/pii/S0020768312001680`.

[67] M. Schwarze, I. N. Vladimirov, and S. Reese, "Sheet metal forming and springback simulation by means of a new reduced integration solid-shell finite element technology," *Computer Methods in Applied Mechanics and Engineering*, vol. 200, no. 5, pp. 454–476, 2011, ISSN: 0045-7825. DOI: `https://doi.org/10.1016/j.cma.2010.07.020`. [Online]. Available: `https://www.sciencedirect.com/science/article/pii/S004578251000232X`.

[68] P. Wu, D. Lloyd, A. Bosland, H. Jin, and S. MacEwen, "Analysis of roping in aa6111 automotive sheet," *Acta Materialia*, vol. 51, no. 7, pp. 1945–1957, 2003, ISSN: 1359-6454. DOI: `https://doi.org/10.1016/S1359-6454(02)00600-6`. [Online]. Available: `https://www.sciencedirect.com/science/article/pii/S1359645402006006`.

[69] M. M. da Costa Neto, G. C. Silva, M. Matějka, *et al.*, *Study of the stampability of aisi 441 steel under different initial conditions*, version 1, Preprint, Mar. 2024. DOI: `10.21203/rs.3.rs-4177615/v1`. [Online]. Available: `https://doi.org/10.21203/rs.3.rs-4177615/v1`.

[70] L. L. Pessanha, M. B. Silva, J. J. Grácio, C. A. Barbosa, and L. A. Pessan, "Effect of shear direction on work-hardening evolution of aisi 409 steel under rolling/shearing loading," *Materials Research*, vol. 25, e20210398, 2022. DOI: `10.1590/1980-5373-MR-2021-0398`. [Online]. Available: `https://doi.org/10.1590/1980-5373-MR-2021-0398`.

Appendix A

Annexes

A.1 Mohr's Circle and Invariant Stresses for Barlat89

To find a plane which the shear stresses are null the principal directions must be find. There's two ways to find the principal directions, the first one is to obtain the eigenvalues and eigenvectors and find the diagonal matrix. The second form is to use the Mohr's Circle's method.

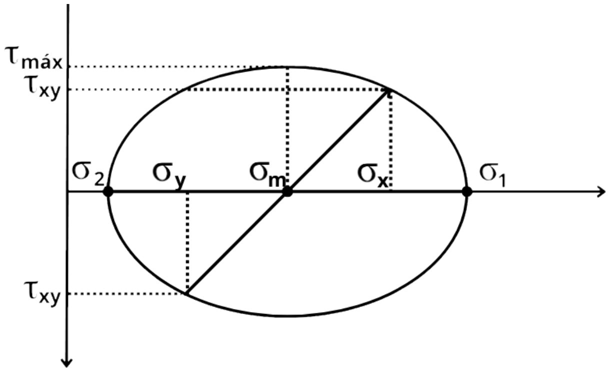

Figure A.1: Mohr's Circle

Fig. A.1 shows the Mohr's Circle. When the problem has initially the stresses σ_x, σ_y and τ_{xy} the principal stresses σ_1 and σ_2 can be find.

First, to calculate the σ_m the mean value between σ_x and σ_x can be obtained.

$$\sigma_m = \frac{\sigma_x + \sigma_y}{2} \tag{A.1}$$

As defined in Section 3.1.5 the K_1 therm Eq. 3.18 is equal to the Eq. A.1 for the isotropic case. The same occurs with the K_2 variable which is equal to the radius R.

$$R^2 = a^2 + b^2$$

Where R is the hypotenuse or the radius and $a = \pm\tau_{xy}$ and $b = |\sigma_x - \sigma_m| = |\sigma_m - \sigma_y|$ are the legs.

$$R = \sqrt{\tau_{xy}^2 + \left(\frac{\sigma_x - \sigma_y}{2}\right)^2} \tag{A.2}$$

Then by summing or subtracting the radius from the σ_m we can obtain σ_1 and σ_2.

$$\begin{cases} \sigma_1 = \sigma_m + R = K_1 + K_2 \\ \sigma_2 = \sigma_m - R = K_1 - K_2 \end{cases} \tag{A.3}$$

Then the Huber Von Mises yield criteria for plane stress is shown below.

$$f = \sigma_1^2 + \sigma_2^2 + (\sigma_2 - \sigma_1)^2 = 2\overline{\sigma}^2 \tag{A.4}$$

This equation can be rewritten by using K_1 and K_2.

$$f = (K_1 + K_2)^2 + (K_1 - K_2)^2 + (-2K_2)^2 = 2\overline{\sigma}^2 \tag{A.5}$$

A.2 MatLab Codes and Functions

A GitHub link will be provided with the all needed information. For further references acess GitHub Hyperlink

Acciai Speciali Terni S.p.A.
Viale B. Brin, 218 - 05100 Terni - Italia
AZIENDA CON SISTEMA DI GESTIONE CERTIFICATO SECONDO ISO 9001

CERTIFICATO DI COLLAUDO INSPECTION CERTIFICATE
CERTIFICATE DE RECEPTION ABNAHMEPRÜFZEUGNIS B*

EN 10204/3.1

1/1

AVV. DI SPEDIZ. N°: 0180650820
SHIPPING NOTICE N°
AVIS D'EXPEDITION N°
VERSANDANZEIGE Nr

ORDINE CLIENTE N°: OOA0108100F
CUSTOMER ORDER N°
COMMANDE DU CLIENT N°

ORDINE INTERNO N°: SA237996
INTERNAL ORDER N°
COMMANDE INT. N°
WERKS Nr

CERTIFICATO N°: 02254071
CERTIFICATE N°

CARICO N°: 0020031934

CLIENTE: THYSSENKRUPP MATERIALS IBERICA S.A.
CUSTOMER: POL. IND. MARTORELLES C/. SAINT MAR
CLIENT: MARTORELLES (BARCELONA)
BESTELLER: 08107 - 26 - Spagna

PRODOTTO: STAINLESS STEEL COILS
PRODUCT
PRODUIT
PRUFGEGENSTAND

DESTINATARIO: THYSSENKRUPP MATERIALS IBERICA
SHIP TO PARTY: S.A.
CLIENT LIVRÉ: POLIG. IND. ZONA FRANCA-CALLE 62
WARENEMPFÄNGER: SE

N° ROTOLO COIL N° N° BOBINE BAND Nr.	N° COLATA HEAT N° N° COULEE SCHMELZE Nr.	**COMPOSIZIONE CHIMICA** / CHEMICAL COMPOSITION / COMPOSITION CHIMIQUE/ CHEMISCHE ZUSAMMENSETZUNG													
		% C	% Mn	% Si	% P	% S	% Cr	% Ni	% Mo	% N	% Ti	NB %	%	%	%
187719	0470803	0,014	0,310	0,500	0,025	0,001	17,82	0,250	0,060	0,017	0,140	0,370			

SPECIFICA, SPECIFICATION, ANFORDERUNGEN:	**TIPO D'ACCIAIO,** STEEL TYPE, TYPE D'ACIER, MARKENBEZEICHNUNG:
EN 10088-2 AST	1.4509 441AR

TRATT. TERMICO - RICOTTURA DI SOLUBILIZZ. 850^C ARIA - ACQUANEBULIZZATA - ACQUA
HEAT TRATMENT - ANNEALING: AIR - WATER SPRAY - WATER COOLING
TRAITEMENT - THERMIQUE - HYPERTREMPE: AIR - EAU ATOMISEE - EAU
WARMEBEHANDLUNG - ABSCHRECKEN. °C/LUFT - SPRÜHWASSER - WASSER

PROCESSO DI ELABORAZIONE: E + AOD + CC
STEELMAKING PROCESS
PROCEDE D'ELABORATION
ERSCHMELZUNGSART

IL MATERIALE È RESISTENTE ALLA CORROSIONE INTERGRANULARE SECONDO:
THE MATERIAL IS RESISTANT TO INTERCRYSTALLINE CORROSION IN ACCORDANCE WITH:
LE MATERIEL EST RESISTANT A LA CORROSION INTERGRANULAIR SELON:
DAS MATERIAL IST BESTÄNDIG GEGEN INTERKRISTALLINE KORROSION GEMÄSS:

RISULTATI DELLE PROVE / TEST RESULTS / RESULTATS DES ESSAIS /ERGEBNIS DER PRÜFUNGEN (1 N / m m^2 = 1 M Pa)

N° COLLO PACKAGE N° N° COLIS KISTEN Nr.	**N° ROTOLO** COIL N° N° BOBINE BAND Nr.	**DIMENSIONI** DIMENSIONS ABMESSUNGEN mm	**N° PEZZI** PIECES N° N° PIECES STÜCKZAHL	**FINITURA** FINISH FINITION AUSFÜHRG	**PESO** WEIGHT POIDS GEWICHT Kg.	PRELIEVO (1)	SENSO (2)	**TRAZIONE** / TENSILE / TRACTION / ZUGVERSUCH ACCORDING TO EN 6892-1						**DUREZZA** HARDNESS DURETE HARTE		**PIEGA** BEND PLIAGE FALTVERSUCH	**GRANO** GRAIN KORN (size)		
								Rp 0.2%	Rp 1%	Rm	A %								
								N/mm^2	N/mm^2	N/mm^2	Lo = 2"	Lo = 80	Lo = A5	HRB					
CARATTERISTICHE RICHIESTE - REQUIRED CHARACTERISTICS -CHARACTERISTIQUES REQUISES - ANFORDERUNGEN								≥ 250	≥	430-630	≥	≥	≥ 18	≤	≤				
C0645326	187719	3.00X665.0	1	2B	4.970	T	T	344		539			31,1	81,0					
C0645326						C	T	346		501			36,7	82,0					
C0645327	187719	3.00X665.0	1	2B	4.820	T	T	344		539			31,1	81,0					
C0645327						C	T	346		501			36,7	82,0					

Certificato emesso automaticamente
COMPLIES WITH ED 2000/53/EC
MATERIAL IDENTIFICATION CHECK, SURFACE QUALITY AND DIMENSIONS = OK
The material meets the hardness requirements of NACE MR0175/MR0103/ISO 15156-3

Certifichiamo che i prodotti sopra elencati sono conformi alle prescrizioni dell'ordine.
We certify that products listed above comply with order requirements.
Nous certifions que les produits ci-dessus énumerés sont conformes aux prescriptions de la commande.
Wir bestaetigen, dass die Lieferung den Vereinbarungen der Bestallannahme entspricht.

TIMBRO DEL PRODUTTORE: **Acciai Speciali Terni S.p.A.**
PRODUCER TRADE MARK:
MARQUE DU PRODUCTEUR:
ZEICHEN DES LIEFERWERKS:

Acciai Speciali Terni S.p.A.
FIRMA DEL RESPONSABILE INCARICATO
INSPECTOR SIGNATURE
SIGNATURE DU RESPONSABLE CHARGÈ UNTERSCHRIFT
DES WERKSSACHVERSTÄNDINGEN

TERNI IL 11.12.2023 Responsabile del Laboratorio S. Contadini

1) Sampling - Location - Ort
T = Testa - Top - Téte - Kopf
C = Coda - Bottom - Pied - Fuss

2) Sens - Direction - Richtung
T = Trasversale - Transverse - Traverse - Quer
L = Longitudinale - Longitudinal - Long - Längs

Acciai Speciali Terni S.p.A.
Viale B. Brin, 218 - 05100 Terni - Italia
AZIENDA CON SISTEMA DI GESTIONE CERTIFICATO SECONDO ISO 9001

CERTIFICATO DI COLLAUDO INSPECTION CERTIFICATE CERTIFICATE DE RECEPTION ABNAHMEPRÜFZEUGNIS B*

EN 10204/3.1

1/1

AVV. DI SPEDIZ. N°: 0180616902
SHIPPING NOTICE N°
AVIS D'EXPEDITION N°
VERSANDANZEIGE Nr

ORDINE CLIENTE N°: OOA0107984F
CUSTOMER ORDER N°
COMMANDE DU CLIENT N°

ORDINE INTERNO N°: SA237780
INTERNAL ORDER N°
COMMANDE INT. N°
WERKS Nr

CERTIFICATO N°: 02238962
CERTIFICATE N°

CARICO N°: 0020030628

CLIENTE: THYSSENKRUPP MATERIALS IBERICA S.A.
CUSTOMER: POL. IND. MARTORELLES C/. SAINT MAR
CLIENT: MARTORELLES (BARCELONA)
BESTELLER: 08107 - 26 - Spagna

DESTINATARIO: THYSSENKRUPP MATERIALS IBERICA
SHIP TO PARTY: S.A.
CLIENT LIVRÉ: POLIG. IND. ZONA FRANCA-CALLE 62
WARENEMPFÄNGER: SE

PRODOTTO: STAINLESS STEEL COILS
PRODUCT
PRODUIT
PRUFGEGENSTAND

N° ROTOLO COIL N° N° BOBINE BAND Nr.	**N° COLATA** HEAT N° N° COULEE SCHMELZE Nr.	**COMPOSIZIONE CHIMICA** / CHEMICAL COMPOSITION / COMPOSITION CHIMIQUE/ CHEMISCHE ZUSAMMENSETZUNG													
		% C	% Mn	% Si	% P	% S	% Cr	% Ni	% Mo	% N	% Ti	NB %	%	%	%
134439	0469985	0,010	0,390	0,550	0,020	0,001	11,47	0,140	0,035	0,012	0,240	0,008			

SPECIFICA, SPECIFICATION, ANFORDERUNGEN:	**TIPO D'ACCIAIO,** STEEL TYPE, TYPE D'ACIER, MARKENBEZEICHNUNG:
EN 10088-2 AST	1.4512 409

TRATT. TERMICO - RICOTTURA DI SOLUBILIZZ. 820^C ARIA - ACQUANEBULIZZATA - ACQUA
HEAT TRATMENT - ANNEALING: AIR - WATER SPRAY - WATER COOLING
TRAITEMENT - THERMIQUE - HYPERTREMPE: AIR - EAU ATOMISEE - EAU
WARMEBEHANDLUNG - ABSCHRECKEN. °C/LUFT - SPRÜHWASSER - WASSER

PROCESSO DI ELABORAZIONE: E + AOD + CC
STEELMAKING PROCESS
PROCEDE D'ELABORATION
ERSCHMELZUNGSART

IL MATERIALE È RESISTENTE ALLA CORROSIONE INTERGRANULARE SECONDO:
THE MATERIAL IS RESISTANT TO INTERCRYSTALLINE CORROSION IN ACCORDANCE WITH:
LE MATERIEL EST RESISTANT A LA CORROSION INTERGRANULAIR SELON:
DAS MATERIAL IST BESTÄNDIG GEGEN INTERKRISTALLINE KORROSION GEMÄSS:

RISULTATI DELLE PROVE / TEST RESULTS / RESULTATS DES ESSAIS /ERGEBNIS DER PRÜFUNGEN (1 N / m m^2 = 1 M Pa)

N° COLLO PACKAGE N° N° COLIS KISTEN Nr.	**N° ROTOLO** COIL N° N° BOBINE BAND Nr.	**DIMENSIONI** DIMENSIONS ABMESSUNGEN mm	**N° PEZZI** PIECES N° N° PIECES STÜCKZAHL	**FINITURA** FINISH FINITION AUSFÜHRG	**PESO** WEIGHT POIDS GEWICHT Kg.	PRELIEVO (1)	SENSO (2)	**TRAZIONE** / TENSILE / TRACTION / ZUGVERSUCH **ACCORDING TO EN 6892-1**						**DUREZZA** HARDNESS DURETE HARTE		**PIEGA** BEND PLIAGE FALTVERSUCH	**GRANO** GRAIN KORN (size)		
								Rp 0.2%	**Rp 1%**	**Rm**	**A %**								
								N/mm^2	N/mm^2	N/mm^2	Lo = 2"	Lo = 80	Lo = A5	HRB					
CARATTERISTICHE RICHIESTE - REQUIRED CHARACTERISTICS -CHARACTERISTIQUES REQUISES - ANFORDERUNGEN								≥ 220	≥	380-560	≥	≥ 25	≥	≤	≤				
C0617942	134439	1.20X557.0	1	2B	3.242	T	T	269		421		32,6		67,0		GOOD			
C0617942						C	T	283		438		33,7		71,0		GOOD			
C0618413	134439	1.20X557.0	1	2B	3.242	T	T	269		421		32,6		67,0		GOOD			
C0618413						C	T	283		438		33,7		71,0		GOOD			

Certificato emesso automaticamente
COMPLIES WITH ED 2000/53/EC

Valore della prova di durezza convertito secondo ASTM E140
MATERIAL IDENTIFICATION CHECK, SURFACE QUALITY AND DIMENSIONS = OK
The material meets the hardness requirements of NACE MR0175/MR0103/ISO 15156-3

Certifichiamo che i prodotti sopra elencati sono conformi alle prescrizioni dell'ordine.
We certify that products listed above comply with order requirements.
Nous certifions que les produits ci-dessus énumerés sont conformes aux prescriptions de la commande.
Wir bestaetigen, dass die Lieferung den Vereinbarungen der Bestallannahme entspricht.

TIMBRO DEL PRODUTTORE: **Acciai Speciali Terni S.p.A.**
PRODUCER TRADE MARK:
MARQUE DU PRODUCTEUR:
ZEICHEN DES LIEFERWERKS:

Acciai Speciali Terni S.p.A.
FIRMA DEL RESPONSABILE INCARICATO
INSPECTOR SIGNATURE
SIGNATURE DU RESPONSABLE CHARGÈ UNTERSCHRIFT
DES WERKSSACHVERSTÄNDINGEN

TERNI IL 29.09.2023 Responsabile del Laboratorio S. Contadini

1) Sampling - Location - Ort
T = Testa - Top - Téte - Kopf
C = Coda - Bottom - Pied - Fuss

2) Sens - Direction - Richtung
T = Trasversale - Transverse - Traverse - Quer
L = Longitudinale - Longitudinal - Long - Längs

Acciai Speciali Terni S.p.A.
Viale B. Brin, 218 - 05100 Terni - Italia
AZIENDA CON SISTEMA DI GESTIONE CERTIFICATO SECONDO ISO 9001

CERTIFICATO DI COLLAUDO INSPECTION CERTIFICATE
CERTIFICATE DE RECEPTION ABNAHMEPRÜFZEUGNIS B*

EN 10204/3.1

1/1

AVV. DI SPEDIZ. N°: 0180637286
SHIPPING NOTICE N°
AVIS D'EXPEDITION N°
VERSANDANZEIGE Nr

ORDINE CLIENTE N°: OOA0108039M
CUSTOMER ORDER N°
COMMANDE DU CLIENT N°

ORDINE INTERNO N°: 8R230148
INTERNAL ORDER N°
COMMANDE INT. N°
WERKS Nr

CERTIFICATO N°: 02248413
CERTIFICATE N°

CARICO N°: 0020031511

CLIENTE: THYSSENKRUPP MATERIALS IBERICA S.A.
CUSTOMER: POL. IND. MARTORELLES C/. SAINT MAR
CLIENT: MARTORELLES (BARCELONA)
BESTELLER: 08107 - 26 - Spagna

PRODOTTO: STAINLESS STEEL COILS
PRODUCT
PRODUIT
PRUFGEGENSTAND

DESTINATARIO: THYSSENKRUPP MATERIALS IBERICA S.A.
SHIP TO PARTY: POLIG. IND. ZONA FRANCA-CALLE 62
CLIENT LIVRÉ: SE
WARENEMPFÄNGER:

N° ROTOLO COIL N° N° BOBINE BAND Nr.	N° COLATA HEAT N° N° COULEE SCHMELZE Nr.	**COMPOSIZIONE CHIMICA** / CHEMICAL COMPOSITION / COMPOSITION CHIMIQUE/ CHEMISCHE ZUSAMMENSETZUNG													
		% C	% Mn	% Si	% P	% S	% Cr	% Ni	% Mo	% N	% Ti	NB %	%	%	%
167911	0470479	0,011	0,310	0,630	0,024	0,001	11,44	0,210	0,035	0,010	0,190	0,008			

SPECIFICA, SPECIFICATION, ANFORDERUNGEN:	**TIPO D'ACCIAIO,** STEEL TYPE, TYPE D'ACIER, MARKENBEZEICHNUNG:
EN 10088-2 AST	1.4512 409

TRATT. TERMICO - RICOTTURA DI SOLUBILIZZ. 820^C ARIA - ACQUANEBULIZZATA - ACQUA
HEAT TRATMENT - ANNEALING: AIR - WATER SPRAY - WATER COOLING
TRAITEMENT - THERMIQUE - HYPERTREMPE: AIR - EAU ATOMISEE - EAU
WARMEBEHANDLUNG - ABSCHRECKEN. °C/LUFT - SPRÜHWASSER - WASSER

PROCESSO DI ELABORAZIONE: E + AOD + CC
STEELMAKING PROCESS
PROCEDE D'ELABORATION
ERSCHMELZUNGSART

IL MATERIALE È RESISTENTE ALLA CORROSIONE INTERGRANULARE SECONDO:
THE MATERIAL IS RESISTANT TO INTERCRYSTALLINE CORROSION IN ACCORDANCE WITH:
LE MATERIEL EST RESISTANT A LA CORROSION INTERGRANULAIR SELON:
DAS MATERIAL IST BESTÄNDIG GEGEN INTERKRISTALLINE KORROSION GEMÄSS:

RISULTATI DELLE PROVE / TEST RESULTS / RESULTATS DES ESSAIS /ERGEBNIS DER PRÜFUNGEN (1 N / m m^2 = 1 M Pa)

N° COLLO PACKAGE N° N° COLIS KISTEN Nr.	**N° ROTOLO** COIL N° N° BOBINE BAND Nr.	**DIMENSIONI** DIMENSIONS ABMESSUNGEN mm	**N° PEZZI** PIECES N° N° PIECES STÜCKZAHL	**FINITURA** FINISH FINITION AUSFÜHRG	**PESO** WEIGHT POIDS GEWICHT Kg.	PRELIEVO (1)	SENSO (2)	**TRAZIONE** / TENSILE / TRACTION / ZUGVERSUCH **ACCORDING TO EN 6892-1**						**DUREZZA** HARDNESS DURETE HARTE		**PIEGA** BEND PLIAGE FALTVERSUCH	**GRANO** GRAIN KORN (size)		
								Rp 0.2%	**Rp 1%**	**Rm**	**A %**								
								N/mm²	**N/mm²**	**N/mm²**	**Lo = 2"**	**Lo = 80**	**Lo = A5**	HRB					
CARATTERISTICHE RICHIESTE - REQUIRED CHARACTERISTICS -CHARACTERISTIQUES REQUISES - ANFORDERUNGEN								≥ 220	≥	380-560	≥	≥ 25	≥	≤	≤				
C0630653 C0630653	167911	1.20X1270.0	1	2B	19.000	T C	T T	274 275		435 422		37,3 39,7		71,0 72,0		GOOD GOOD			

Certificato emesso automaticamente
COMPLIES WITH ED 2000/53/EC

Valore della prova di durezza convertito secondo ASTM E140
MATERIAL IDENTIFICATION CHECK, SURFACE QUALITY AND DIMENSIONS = OK
The material meets the hardness requirements of NACE MR0175/MR0103/ISO 15156-3

Certifichiamo che i prodotti sopra elencati sono conformi alle prescrizioni dell'ordine.
We certify that products listed above comply with order requirements.
Nous certifions que les produits ci-dessus énumerés sont conformes aux prescriptions de la commande.
Wir bestaetigen, dass die Lieferung den Vereinbarungen der Bestallannahme entspricht.

TIMBRO DEL PRODUTTORE: **Acciai Speciali Terni S.p.A.**
PRODUCER TRADE MARK:
MARQUE DU PRODUCTEUR:
ZEICHEN DES LIEFERWERKS:

Acciai Speciali Terni S.p.A.
FIRMA DEL RESPONSABILE INCARICATO
INSPECTOR SIGNATURE
SIGNATURE DU RESPONSABLE CHARGÈ UNTERSCHRIFT
DES WERKSSACHVERSTÄNDINGEN

TERNI IL 13.11.2023 Responsabile del Laboratorio S. Contadini

Contadini

1) Sampling - Location - Ort
T = Testa - Top - Téte - Kopf
C = Coda - Bottom - Pied - Fuss

2) Sens - Direction - Richtung
T = Trasversale - Transverse - Traverse - Quer
L = Longitudinale - Longitudinal - Long - Längs

Acciai Speciali Terni S.p.A.
Viale B. Brin, 218 - 05100 Terni - Italia
AZIENDA CON SISTEMA DI GESTIONE CERTIFICATO SECONDO ISO 9001

CERTIFICATO DI COLLAUDO INSPECTION CERTIFICATE CERTIFICATE DE RECEPTION ABNAHMEPRÜFZEUGNIS B*

EN 10204/3.1

1/1

AVV. DI SPEDIZ. N°: 0180648413
SHIPPING NOTICE N°
AVIS D'EXPEDITION N°
VERSANDANZEIGE Nr

ORDINE CLIENTE N°: OOA0108100F
CUSTOMER ORDER N°
COMMANDE DU CLIENT N°

ORDINE INTERNO N°: SA237996
INTERNAL ORDER N°
COMMANDE INT. N°
WERKS Nr

CERTIFICATO N°: 02252906
CERTIFICATE N°

CARICO N°: 0020031846

CLIENTE: THYSSENKRUPP MATERIALS IBERICA S.A.
CUSTOMER: POL. IND. MARTORELLES C/. SAINT MAR
CLIENT: MARTORELLES (BARCELONA)
BESTELLER: 08107 - 26 - Spagna

DESTINATARIO: THYSSENKRUPP MATERIALS IBERICA
SHIP TO PARTY: S.A.
CLIENT LIVRÉ: POLIG. IND. ZONA FRANCA-CALLE 62
WARENEMPFÄNGER: SE

PRODOTTO: STAINLESS STEEL COILS
PRODUCT
PRODUIT
PRUFGEGENSTAND

N° ROTOLO COIL N° N° BOBINE BAND Nr.	N° COLATA HEAT N° N° COULEE SCHMELZE Nr.	**COMPOSIZIONE CHIMICA** / CHEMICAL COMPOSITION / COMPOSITION CHIMIQUE/ CHEMISCHE ZUSAMMENSETZUNG													
		% C	% Mn	% Si	% P	% S	% Cr	% Ni	% Mo	% N	% Ti	NB %	%	%	%
168901	0470467	0,014	0,320	0,460	0,025	0,001	17,66	0,350	0,065	0,016	0,120	0,360			

SPECIFICA, SPECIFICATION, ANFORDERUNGEN:	**TIPO D'ACCIAIO,** STEEL TYPE, TYPE D'ACIER, MARKENBEZEICHNUNG:
EN 10088-2 AST	1.4509 441AR

TRATT. TERMICO - RICOTTURA DI SOLUBILIZZ. 850^C ARIA - ACQUANEBULIZZATA - ACQUA
HEAT TRATMENT - ANNEALING: AIR - WATER SPRAY - WATER COOLING
TRAITEMENT - THERMIQUE - HYPERTREMPE: AIR - EAU ATOMISEE - EAU
WARMEBEHANDLUNG - ABSCHRECKEN. °C/LUFT - SPRÜHWASSER - WASSER

PROCESSO DI ELABORAZIONE: E + AOD + CC
STEELMAKING PROCESS
PROCEDE D'ELABORATION
ERSCHMELZUNGSART

IL MATERIALE È RESISTENTE ALLA CORROSIONE INTERGRANULARE SECONDO:
THE MATERIAL IS RESISTANT TO INTERCRYSTALLINE CORROSION IN ACCORDANCE WITH:
LE MATERIEL EST RESISTANT A LA CORROSION INTERGRANULAIR SELON:
DAS MATERIAL IST BESTÄNDIG GEGEN INTERKRISTALLINE KORROSION GEMÄSS:

RISULTATI DELLE PROVE / TEST RESULTS / RESULTATS DES ESSAIS /ERGEBNIS DER PRÜFUNGEN (1 N / m m^2 = 1 M Pa)

N° COLLO PACKAGE N° N° COLIS KISTEN Nr.	N° ROTOLO COIL N° N° BOBINE BAND Nr.	DIMENSIONI DIMENSIONS ABMESSUNGEN mm	N° PEZZI PIECES N° N° PIECES STÜCKZAHL	FINITURA FINISH FINITION AUSFÜHRG	PESO WEIGHT POIDS GEWICHT Kg.	PRELIEVO (1)	SENSO (2)	**TRAZIONE** / TENSILE / TRACTION / ZUGVERSUCH ACCORDING TO EN 6892-1						DUREZZA HARDNESS DURETE HARTE		PIEGA BEND PLIAGE FALTVERSUCH	GRANO GRAIN KORN (size)		
								Rp 0.2%	Rp 1%	Rm	A %								
								N/mm^2	N/mm^2	N/mm^2	Lo = 2"	Lo = 80	Lo = A5	HRB					
CARATTERISTICHE RICHIESTE - REQUIRED CHARACTERISTICS -CHARACTERISTIQUES REQUISES - ANFORDERUNGEN								≥ 250	≥	430-630	≥	≥	≥ 18	≤	≤				
C0642328	168901	3.00X665.0	1	2B	4.450	T	T	338		480			37,2	80,0					
C0642328						C	T	326		490			39,7	78,0					
C0642329	168901	3.00X665.0	1	2B	4.224	T	T	338		480			37,2	80,0					
C0642329						C	T	326		490			39,7	78,0					

Certificato emesso automaticamente
COMPLIES WITH ED 2000/53/EC
MATERIAL IDENTIFICATION CHECK, SURFACE QUALITY AND DIMENSIONS = OK

Certifichiamo che i prodotti sopra elencati sono conformi alle prescrizioni dell'ordine.
We certify that products listed above comply with order requirements.
Nous certifions que les produits ci-dessus énumerés sont conformes aux prescriptions de la commande.
Wir bestaetigen, dass die Lieferung den Vereinbarungender Bestallannahme entspricht.

TIMBRO DEL PRODUTTORE: **Acciai Speciali Terni S.p.A.**
PRODUCER TRADE MARK:
MARQUE DU PRODUCTEUR:
ZEICHEN DES LIEFERWERKS:

Acciai Speciali Terni S.p.A.
FIRMA DEL RESPONSABILE INCARICATO
INSPECTOR SIGNATURE
SIGNATURE DU RESPONSABLE CHARGÈ UNTERSCHRIFT
DES WERKSSACHVERSTÄNDINGEN

TERNI IL 04.12.2023 Responsabile del Laboratorio S. Contadini

1) Sampling - Location - Ort
T = Testa - Top - Téte - Kopf
C = Coda - Bottom - Pied - Fuss

2) Sens - Direction - Richtung
T = Trasversale - Transverse - Traverse - Quer
L = Longitudinale - Longitudinal - Long - Làngs